The Dissertation Committee for Jason Chi-Sing Lee certifies that this is the approved version of the following dissertation:

CHARACTERIZATION OF ABLATIVE PROPERTIES OF THERMOPLASTIC POLYURETHANE ELASTOMER NANOCOMPOSITES

Committee:

John R. Howell, Supervisor

Joseph H. Koo, Co-Supervisor

Ofodike A. Ezekoye

Eric M. Taleff

Donald R. Paul

CHARACTERIZATION OF ABLATIVE PROPERTIES OF THERMOPLASTIC POLYURETHANE ELASTOMER NANOCOMPOSITES

By

Jason Chi-Sing Lee, B.S., M.S.

Dissertation

Presented to the Faculty of the Graduate School of
The University of Texas at Austin
in Partial Fulfillment
of the Requirements
for the Degree of

Doctor of Philosophy

The University of Texas at Austin
December 2010

Dedication

To my parents Norman and Anny,
my sisters, Rene’ and Tammy,
my uncle and aunt in Austin, Jack and Susan,
their daughters Samantha and Madeline,
and my beautiful girlfriend, Luana.

Acknowledgements

I would like to first thank my advisors; Dr. Jack Howell, Ofodike Ezekoye, and Joseph H. Koo, for helping me with the technical portions of the research. All three of them have always been encouraging when I have come to them in total frustration. I really admire how calm and humble they have always been. I would also like to thank both Dr. Donald Paul and Eric Taleff for serving on my committee. I am extremely lucky to have had such role models to work with. None of this work would have been possible without funding from AFOSR (Grant No. FA9550-06-1-0356) and the Predictive Engineering and Computational Sciences (PECOS). I would like to thank Dr. Charles Y. Lee from AFOSR as well as Dr. Robert Moser and Chris Simmons from the PECOS project for helping provide funding. Fatima Bridgewater, Rosalie Foster, and Cindy Raman each helped make the waiting for reimbursements and processing purchase orders as fast and painless as that paperwork can be.

Dr. Kenneth Erickson at Sandia National Laboratory helped me a lot when I worked with him in fall 2009. I also used selective equipment in the FNT and would like to thank Dr. William Lackowski the former FNT facility manager and Mr. Jeff Cook who trained me on the SEM. Thank you to Dr. Gerry Wissler who compounded the materials that were tested. A lot of additional help with experiments, experimental analysis, and material supplies came from: the Pittsburg State University (Dr. Chris Ibeh and Dustin Hart), Fredericksburg High School Aeroscience Director Brett Williams, Dr. Patrick Piccone of Arkema, Joseph Ventura of Bayer, Max Lake of Applied Sciences, and Dr. Doug Hunter of Southern Clay Products.

Some of the graduate students helped me with experiments as well as get my mind off of work including: Dickson Lao, Jamil Wakil, Dave Ho, Khiet Nguyen, Nathan Malcolm, Joshua Keena, Budi Hadisujoto and the "lunch bunch" (Sol Keun Jee, Uday Godsee, Sanjiv Shah, Morgan Bruns). I also very much enjoyed working with many undergraduates on this project as well as number of different projects: Chris Lam, Chris Wu, Adam Scott, Hugo Redondo, David Chen and a few Senior K-Group and Polymer nanocomposite students.

My parents and sisters called and visited often and encouraged me to continue when research did not go well. My uncle Jack and his family who also live in Austin not only helped me feel at home but also fed me often and well. My girlfriend, Luana Bessa, is working on her own PhD. That has helped us encourage each other since we both understand the frustrations of grad school. She is soon to complete her PhD as well, and I am very proud of her. Thank you, Luana.

I also want to thank the friends from Hyde Park and Gateway Church who encouraged and prayed for me. And thanks to Jesus Christ, in the past couple of years, I have had to pray a lot as I went through this program. I thank God that I know there is always someone listening on the other side of those prayers.

I have had support from so many different groups of people. I am very grateful to have made these relationships and very happy to have come to Texas for graduate school.

Thank you all.

CHARACTERIZATION OF ABLATIVE PROPERTIES OF THERMOPLASTIC POLYURETHANE ELASTOMER NANOCOMPOSITES

Publication No._____________

Jason Chi-Sing Lee, Ph.D.
The University of Texas at Austin, 2010

Supervisor: Joseph H. Koo and John Howell

The advancement of each component of aerospace vehicles is necessary as the continual demand for more aggressive missions are created. Improvements in propulsion and guidance system electronics are invaluable; however without material development to protect the vehicle from its environment those advances will not have a practical application. Thermal protection systems (TPS) are required in both external applications; for example on reentry vehicles, as well as in internal applications; to protect the casing of rockets and missiles. This dissertation focuses on a specific type of internal solid rocket motor TPS, ablatives.

Ablatives have been used for decades on aerospace vehicles. To protect the motor from the hostile environment, these materials pyrolyze and char. Both of these mechanisms produce a boundary between the combustion gases and the motor as well as release the heat that the decomposed material has absorbed. These sacrificial materials are intended to protect the casing that it is attached to. With the development of polymer nanocomposites (PNCs) in the last couple of decades, it is of interest to see how these two fields can merge.

Three different nanomaterials (carbon nanofibers, multiwall carbon nanotubes, and nanoclays) are examined to observe how each behaves in environments that simulate the motor firing conditions. These nanomaterials are individually added to a thermoplastic polyurethane elastomer (TPU) at different loadings, creating three distinct families of polymer nanocomposites. To describe a materials ablative performance, a number of material properties must be individually studied; such as thermal, density, porosity, char strength, and rheology. Different experiments are conducted to isolate specific ablative processes in order to identify how each nanomaterial affects the ablative performance.

This dissertation first describes each material and the ablative processes which are characterized by each experiment. Then basic material properties of each family of materials are described. Degradation and flammability experiments then describe the degassing processes. Studies of the material char are then performed after full blown rocket experiments are done. These tests have shown that of the three nanomaterials, nanoclay enhances the TPU ablative performance the most while the CNF provides the least enhancement.

Table of Contents

List of Figures

List of Tables

Chapter 1. Introduction

1.1. MOTIVATION

The concept of rocketry began far before adequate steam and propellant technology was available. In the 9th century, the Chinese discovered black powder and the first rocket engines were created, “fire arrows”. Those who had and used black powder had a significant edge in warfare. Effective as they were, they were very inaccurate and inefficient. In the early 1900’s Robert Goddard added a nozzle to these rockets which doubled the thrust. In the late 1930’s German scientists began studying liquid fuel rockets in aircraft and created turbo pumps used in WWII. They had significant problems with cooling the nozzle. Since then the cooling of aerospace vehicles has been a critical issue, creating the field of thermal protection systems (TPS). Rocket cooling continues to be a topic of further research as rockets are expected to fly faster, further, and more accurately than before.

TPS research has been on the front page of public media ever since the Columbia Space Shuttle accident on February 1, 2003 when a piece of foam insulation broke from the external tank during launch. The foam piece struck the leading edge of the shuttle’s left wing. The damaged TPS resulted in the vehicle’s catastrophic failure during reentry, losing all 7 astronauts. A lot of money had been invested to investigate the root of this problem and strict guidelines are now in place as to inspecting and evaluating the quality of TPS after launch. Similarly a failed TPS on a rocket will result in a failed mission, regardless of how sophisticated the guidance and propellant systems are.

TPS can either be active or passive; an example of an active TPS is a regenerative cooling system which is used on liquid rockets. A passive TPS, which is studied in this dissertation, is an ablative. External ablative materials on reentry vehicles are commonly phenolic/epoxy resin and carbon composite tile materials. These ablatives resist the high heat fluxes, complex flows, and gas chemistries that result from the high velocities these vehicles travel while entering the earth's atmosphere. High heat flux and pressures are also present in rocket motors. Internal rocket motor ablatives such as Kevlar®-filled, ethylene-propylene-diene rubber (EPDM) are used to protect the motor casing. Previous research on a thermoplastic polyurethane elastomer (TPU) nanocomposite set was performed on Pellethane™ 2102-90A, from Dow Chemical. Ho (2007) focused on determining the different kinetics of the material during thermal degradation, and Nguyen (2007) focused on the materials performance under a specified heat load. In order to more closely match the stiffness of EPDM, a softer TPU nanocomposite family set is studied in this dissertation. The study of TPU materials as ablatives is enticing since processing is simple and cheap compared to thermosets. In the following sections; the physics of an ablation process and the motivation of using polymer nanocomposites (PNCs) to solve and test the ablative properties are described.

1.2. ABLATION

Before decomposition of an ablative begins, the material is in virgin state. As the material is heated, different reactions within the material cause decomposition and the release of gas molecules. This process is known as pyrolysis. An ablative material is made up of hydrogen, carbon, nitrogen, and oxygen molecules. During pyrolysis, long molecule bonds break down and the hydrogen, oxygen, and nitrogen components are separated from the material. Essentially what is left after all the material decomposition has occurred is carbon. The remaining carbon material is known as char. During ablation all three zones are present, Figure 1.1. Characterization of the ablative material involves studying different aspects of each material zone. Experiments presented in this dissertation seek to capture the different physics of one or more of these zones.

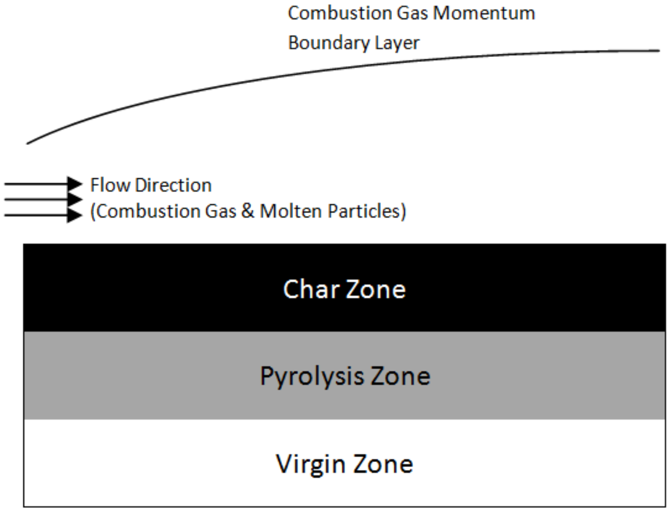

Figure 1.1. Ablation problem global zones.

Ablation is a multiphysics problem, Figure 1.2. All three modes of heat transfer occur simultaneously. The propellant gas interacts with the front face through radiation and convection. Depending on what stage of ablation the system is in, the top surface may be part of any of the three zones. The absorbed energy is then conducted and radiatively transmitted through the three zones. The objective of the ablative is to keep the back face temperature as low as possible. In addition to the specific thermal properties of each zone, different methods of heat release occur during the ablation process.

As the absorbed energy heats the pyrolysis zone, decomposition reactions begin. As the material degases through the front face it provides a convective cooling effect known as the “blowing effect”. Mass transfer also occurs in the char zone through oxidation and external flow shear stresses. Many solid propellant exhausts contain molten alumina particles, typically a couple of microns in diameter. Char surface recession can be significant due to the impingement of these particles. Spallation may also occur if pressures in the gas are high enough causing large normal forces on the char material. Each of these losses in mass are heat releases in the form that a hot mass is removed from the system. However, loss of mass also means that there is a loss of thermal barrier between the propellant gases and back face. This complexity shows that the assessment of a materials ablative performance is strongly a balance between multiple material properties.

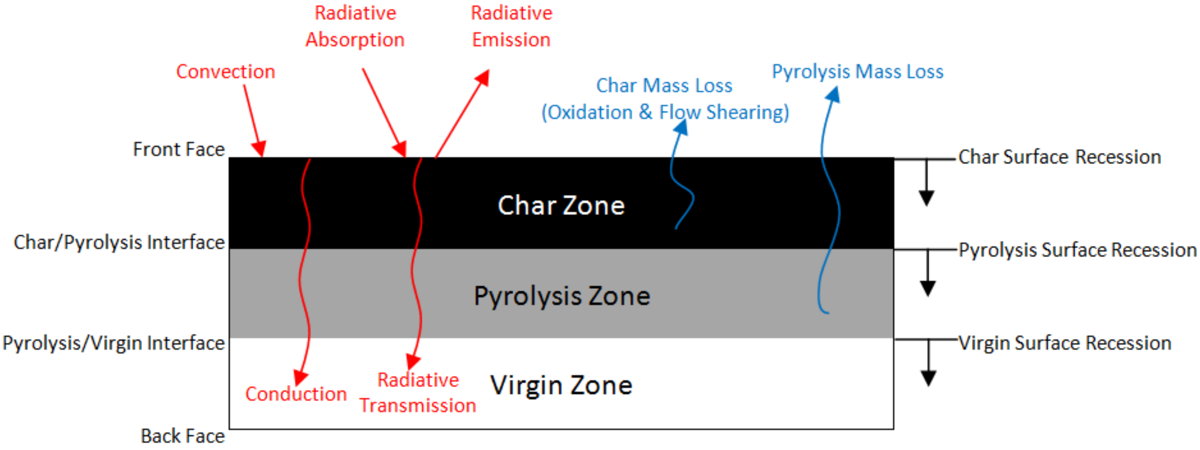

Figure 1.2. Ablation problem physics.

Many computer models for ablation are one-dimensional because the main concern is the in-depth directional thermal profile and surface recession rates. Hurwicz, Kratsch, and Rogan (1972) describe the surface heat transfer by equation 1.1.

$$\dot{q}_s = -\dot{q}_w - \dot{m}_w h_w + \dot{m}_{c_s} h_{c_s} + \dot{m}_{g_s} h_{g_s} - \epsilon_w \sigma T_w^4 + \alpha_w \dot{q}_{rad} - \dot{m}_r h_{c_c} \tag{1.1}$$

where $\dot{q}_s$ is the heat flux from conduction, $\dot{q}_w$ is the wall heat flux, $\dot{m}_w h_w$ is the mass flow rate and enthalpy of wall, $\dot{m}_{c_s} h_{c_s}$ is the mass flow rate and enthalpy of char species, $\dot{m}_{g_s} h_{g_s}$ mass flow rate and enthalpy of the pyrolysis gas species, $\epsilon_w \sigma T_w^4$ is the reradiation term, $\alpha_w \dot{q}_{rad}$ is the incident radiation absorption term and $\dot{m}_r h_{c_c}$ is the mass flow rate and enthalpy due to mechanical erosion. The surface recession rate is often defined using a critical temperature criteria and pure conduction through the different material zones is often used to describe the in-depth thermal gradients. The in-depth heat transfer is modeled by the conduction relationship with the surface heat transfer, $\dot{q}_s = -\left(k\frac{\partial T}{\partial x}\right)_w$. The mass flow rates are constrained with conservation of mass, equation 1.2.

$$\dot{m}_w + \dot{m}_r = \dot{m}_{c_s} + \dot{m}_{g_s} \tag{1.2}$$

1.3. POLYMER NANOCOMPOSITES

EPDM/Kevlar® and phenolic/epoxy resin ablatives are thermoset materials, whereas the TPU material used in this project is a thermoplastic elastomer. Thermosets create crosslinks when cured. This process is irreversible and differentiates with thermoplastics which can be re-melted. Thermoplastic elastomers are copolymers containing a hard anchor and soft elastic segment.

In the last couple of decades, advances in polymer nanocomposites have been shown to be possible in multiple areas including: electrical properties, thermal stability, flammability, mechanical properties, and porosity. This is the motivation behind this study. New applications constantly need new solutions and this is what these materials can provide. A soft TPU is filled with nanomaterials, and the ablative enhancements that can be obtained are studied. To understand these materials' performance, characterizations of individual material properties are performed. TPU at low temperatures are known to melt, thus being a very poor choice as an ablative. However it is expected that even with a small loading of nanomaterials the material will perform drastically better in these conditions. TPU is selected for its ease in processability and recyclability. Three common nanomaterials are used: multiwall carbon nanotubes (MWNTs), nanoclay, and carbon nanofibers (CNFs).

1.4. OVERVIEW OF DISSERTATION

The intent of the experiments chosen is to obtain data from isolated physics during an ablation process from each of the three distinct material zones. In Chapter 2 the processing of the materials used and basic material properties are described. Even at low weight loadings, material enhancements are observed in these fundamental material properties. Multiple degradation experiments are described in Chapter 3. The thermal degradation experiments show enhanced thermal stability and degradation kinetics of the PNCs compared to the neat TPU. Chapter 4 examines flammability experiments which are effective methods to study char formation under low heat fluxes. The char structures studied under microscopy have shown that the different nanomaterials create different char structures. Next in Chapter 5, pyrolysis gases are studied under spectroscopy methods to understand how different additives alter the degradation gas history. The high heat flux of the ablation process is difficult to replicate in the degradation and flammability experiments described in Chapters 3 and 4. Sub-scale experiments in Chapter 6 seek to capture these high heat fluxes to study the ablative performance of these materials. Each of these experiments is effective in comparing the PNC from the neat TPU to show the specific additive enhancements under specific conditions.

Chapter 2. Material Processing and Properties

2.1. INTRODUCTION

This chapter describes the materials that are studied in this dissertation; one resin and three nanomaterials. A description of how the materials are processed is also given. In addition, hardness and density measurements of these PNCs are also described.

2.2. MATERIALS

2.2.1. Thermoplastic Polyurethane Elastomer

The TPU used is Desmopan® DP 6065A. It is a soft aromatic polyether-based thermoplastic polyurethane elastomer (TPU) manufactured by Bayer MaterialScience. It can be processed by extrusion and injection molding, is characterized by good hydrolysis and microbe resistance, short cycle times, and is plasticizer free. Typical applications include rigid/flexible composite systems and sport shoe soles. The diisocyanate in Desmopan® 6065A is methylene diphenyl diisocyanate (MDI) and the polyether is C3 ether based. MDI has 3 forms, 2,2'-MDI, 2,4'-MDI, and 4,4'-MDI. 4,4'-MDI, Figure 2.1, is the most common diisocyanate used and is used in Desmopan® 6065A. The technical and material data sheets list a number of mechanical and thermal properties of this TPU shown in, Table 2.1.

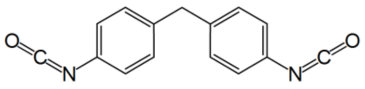

Figure 2.1. Chemical structure of 4,4'-MDI used in Desmopan® 6065A.

Table 2.1. Material properties of Desmopan® DP 6065A.

Typical Properties	Values
General	
Density	1.084 g/cc
Bulk Density	0.5-0.8 g/cc
Hardness (Shore A)	65/66A
Taber Abrasion, H-18 wheel, 1000-g load, 1000 cycles	76 mg loss
Abrasion Resistance	150 mm^3
Bayshore Resilience	49%
Mold Shrinkage @ 100-mil thickness: Flow and Cross-Flow direction	0.008 mm/mm
Mechanical	
Tensile Strength	12.3 MPa
Tensile Stress at 100% elongation	2.6 MPa
Tensile Stress at 300% elongation	4.2 MPa
Ultimate Elongation	890%
Tear Strength, (Die C)	50.9 kN/m
Flexural Modulus @ 23^{o}C, @ -30^{o}C	9.9 MPa, 16.6 MPa
Compression Set. (22 hrs. @70^{o}C, 22hrs @23^{o}C)	34%, 12%
Thermal	
Vicat Softening Temperature (Rate A)	56^{o}C
Glass Transition Temperature (DMA)	-45^{o}C
Specific Heat	1.7 J/g^{o}C
Thermal Conductivity	0.126 W/m^{o}C
Melting Point	220^{o}C
Flash Point	250^{o}C
Auto Ignition Temperature	>210^{o}C
Softening Point	180^{o}C
Initial Decomposition	230^{o}C

2.2.2. Nanoclay Additive

Mechanical and barrier properties of neat resins are improved by nanoclay additives. The in-situ alteration of volcanic ash is a common method of obtaining Montmorillonite (MMT) nanoclay. Stacks of tetrahedral silicate and octahedral alumina layer platelets make up the MMT nanoclay. If well dispersed in a resin, the individual platelets are separated. Each individual platelet is approximately 0.96 nm thick. Southern

Clay Products manufactures Cloisite® additives. This dissertation uses Cloisite® 30B in this TPU. Cloisite® 30B is surface treated so that exfoliation in the TPU resin is possible. The ion exchange between the inorganic alkali cation on the nanoclay and the organic cation is the process of the surface treatment. The modifier used to surface treat Cloisite® 30B is methyl, tallow, bis-2-hydroxyethyl, quaternary ammonium (MT2EtOH), Figure 2.2, at 90 meq/100g. The density and particle size distribution of the premixed nanoclay platelets are described in Table 2.2.

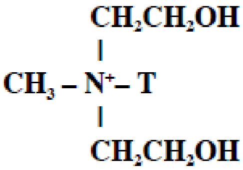

$$\begin{array}{c} \mathrm{CH_2CH_2OH} \\ | \\ \mathrm{CH_3 - N^{+} - T} \\ | \\ \mathrm{CH_2CH_2OH} \end{array}$$

Where T is Tallow (~65% C18; ~30% C16; ~5% C14)

Figure 2.2. Cloisite® 30B modifier, quaternary ammonium salt ion. (Cloisite® Product Bulletin)

Table 2.2. Material properties of Cloisite® 30B.

Density	1.98 g/cc
Bulk Density (Loose, Packed)	0.2283 g/cc, 0.3638 g/cc
Particle Size	10% ≤ 2μm 50% ≤ 6μm 90% ≤ 13μm
Moisture Content	≤ 2%
X-Ray Diffraction d-space (001)	18.5Å

2.2.3. Multiwall Carbon Nanotubes

Arkema produces MWNTs under the trade name Graphistrength®. The manufacturing process is chemical vapor deposition at elevated temperature of ethylene on metal/ceramic catalyst. Plain MWNTs exist in bundles, Figure 2.3, with median diameter approximately 10 to 20 µm. Typical dimensions are 10 to 15 nm in diameter corresponding to approximately 5 to 15 concentric tubes, with lengths approximately 1 to 10 µm. Graphistrength® C100 is used in this study. It contains 3 components: more than 90% graphite, less than 7% Al_2O_3, and less than 5% Fe_2O_3. The MWNT has an apparent density of 0.05-0.15 g/cc, according to the technical data sheet.

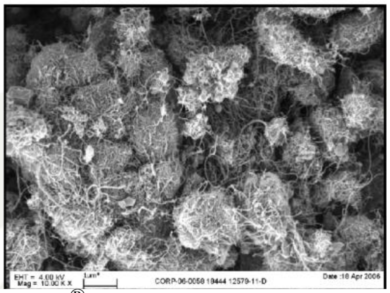

Figure 2.3. Graphistrength® C100 MWNT bundles. (McAndrew, 2008).

2.2.4. Carbon Nanofibers

CNFs are produced through the pyrolysis of hydrocarbons. In gas phase, CNFs are made by chemical vapor deposition. Applied Sciences Inc./Pyrograf® Products manufactures the CNFs used in this dissertation, PR-19-XT-LHT. These CNFs have an average diameter of 150 nm and a length varying from 100 µm to 1 cm. There are 3 grades of PR-19 CNFs: PR-19-XT-PS, PR-19-LHT, and PR-19-HHT which are forms of the CNF heat treated at 900°C, 1500°C, and 3000°C respectively. The low heat treatment removes polyaromatic hydrocarbons and carbon on the CNF surface. The “XT” notation denotes that the CNF is loosened. CNFs are difficult to debulk and during the debulking process often are damaged. These CNFs have a surface area of 20-30 m^2/g, dispersive surface energy of 120-140 mJ/m^2, less than 5% moisture, and an iron content concentration of less than 14,000 ppm. The CNFs used in the study are PR-19-XT LHT CNF and have a bulk density of 0.016-0.048 g/cc.

2.3. PROCESSING

Since the resin material is a TPU, twin screw extrusion is used to process the material. This processing is conducted by 21st Century Polymers, Figure 2.4. The TPU is loaded in the hopper on the right, while the left hopper is filled with a selected nanomaterial. The rate at which the nanomaterials are added is determined by the desired weight loading. The direction of flow is from right to left, such that TPU pellets enter the flow first and are melted. Downstream the nanomaterials are added and the TPU and nanomaterial mixture is mixed as it flows further down the extruder. A specific screw design is selected in parallel with specific thermal conditions controlled by individual heating elements, Figure 2.5.

Figure 2.4. Twin screw extruder.

Figure 2.5. Individual screws and heating elements.

When the material extrudes out of the twin screw extruder it is in a soft spaghetti form. The spaghetti-like material is pulled across a water bath in order to cool and stiffen, Figure 2.6. They are pulled into a chopper that is used to cut the materials about 1 cm in length, forming pellets, Figure 2.7.

Figure 2.6. Extrusion water bath and pellet cutter.

Figure 2.7. TPU Cloisite® 30B pellets.

These pellets can be then used in an injection mold procedure to obtain test specimens of different shapes, Figure 2.8. Similar to the extruder, the injection molding process has locations for heating element specifications. The material is pressed as it is injected and flows into the mold. The molds that used create specimens 3.175 mm (1/8") thick. Injection and processing conditions were set based on those recommended by the settings listed in the Desmopan® product information, Table 2.3. Desired samples that the injection mold is not capable of making are created by compression molding.

Figure 2.8. Injection molder, test specimen mold, and test specimen.

Table 2.3. Injection molding conditions.

Barrel Temperatures	166°C - 177°C	(Rear)
	171°C -179°C	(Middle)
	174°C -185°C	(Front)
	174°C -188°C	(Nozzle)
Melt Temperature	171°C -188°C	
Mold Temperature	16°C -32°C	
Injection Pressure	41.3 – 103.4 MPa (46,000-15,000 psi)	
Hold Pressure	60-80% of Injection Pressure	
Screw Speed	40-80 rpm	
Injection Speed	Slow – Moderate	
Cushion	3.175 mm (1/8") max	

2.4. MATERIAL MATRIX AND DISPERSION QUALITY

Four weight loadings of each of the three nanomaterials are mixed with the TPU, Table 2.4. For both the MWNT and nanoclay specimens, loadings of 10 wt% and lower were studied. Higher weight loadings of CNF are used because previous studies, although with a different TPU and CNF, have shown that in order to reach comparable results with nanoclay, the CNF loading must be significantly higher. For this reason CNF weight loadings up to 20 wt% are used. In each of the PNCs only one nanomaterial is added to the TPU in order to isolate the enhancements of a specific additive. Mixtures of TPU with multiple nanomaterials in a single specimen are not studied in this work; however keeping this in mind for future work may be important. The neat material has an adhesive quality during the processing procedure. At high weight loadings the viscosity of the material increases substantially, especially in the MWNT specimens. Some of the injected 10 wt% MWNT specimens had gaps in the test specimens because the increased viscosity did not allow the material to flow well through the mold.

Table 2.4. Material matrix for TPU nanocomposites.

Formulation	Polymer Matrix (wt%)	Filler (wt%)
1	6065A (100%)	None
2	6065A (97.5%)	(2.5%) Cloisite® 30B nanoclay
3	6065A (95%)	(5%) Cloisite® 30B nanoclay
4	6065A (92.5%)	(7.5%) Cloisite® 30B nanoclay
5	6065A (90%)	(10%) Cloisite® 30B nanoclay
6	6065A (97.5%)	(2.5%) Graphistrength® C100 MWNT
7	6065A (95%)	(5%) Graphistrength® C100 MWNT
8	6065A (92.5%)	(7.5%) Graphistrength® C100 MWNT
9	6065A (90%)	(10%) Graphistrength® C100 MWNT
10	6065A (95%)	(5%) PR-19-XT-LHT CNF
11	6065A (90%)	(10%) PR-19-XT-LHT CNF
12	6065A (85%)	(15%) PR-19-XT-LHT CNF
13	6065A (80%)	(20%) PR-19-XT-LHT CNF

The neat TPU specimens are optically transparent. With the addition of either CNF or MWNT the entire specimen turns black, even at low weight loadings. Visual distinctions between the different weight loadings of these carbon nanomaterial PNCs is not possible. However, the different nanoclay specimens' are visually distinguishable. The PNC's opacity increases with higher nanoclay loading, Figure 2.9.

Figure 2.9. Neat and Cloisite® 30B Desmopan® polymer nanocomposites.

The quality of the additive dispersion within the specimen is dictated by the mixing process. Each of the additives used in this process come in a form where shear must be used to separate individual additive components. In the case of nanoclay, the powder is stack sheets. Southern Clay Products performed the wide angle x-ray diffraction (WAXD) on TPU nanoclay specimens. As mentioned in Table 2.2, the stack platelet Cloisite® 30B has a (001) d-spacing of 18.5Å. From the WAXD graph, Figure 2.10, the platelets in the PNCs are clearly well dispersed in the resin and separated as the d-spacing of the platelet nanoclay are not observed.

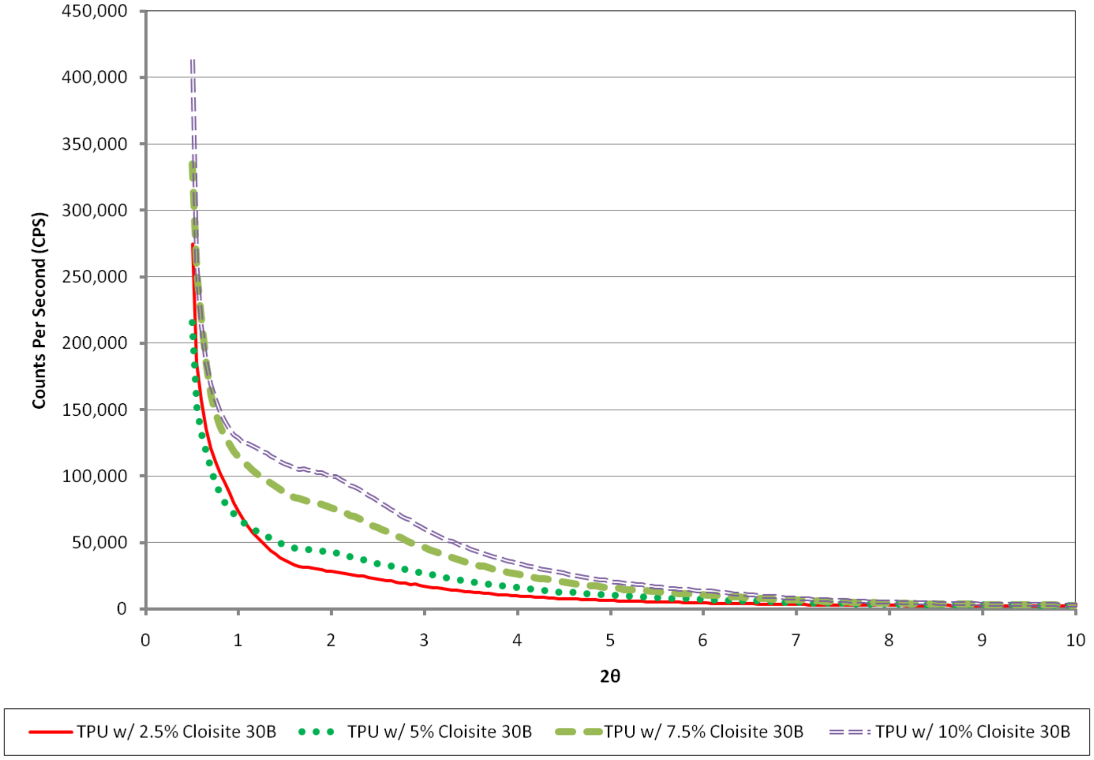

Figure 2.10. Wide angle x-ray diffraction.

In addition, transmission electron microscopy (TEM) images were taken by Dr. Zhiping Luo from Texas A&M, of both the MWNT and nanoclay TPUs are performed in order to determine the quality of dispersion visually, Figure 2.11 and Figure 2.12. In the

2.5 wt% nanoclay sample the individual platelets are easily identifiable and good dispersion is found. The 5 and 10 wt% images show some remaining stacks, however the majority of the image show individual nanoclay platelets. It should also be noted that it does not appear to have any directional orientation from the injection mold process. The MWNT agglomerates are clearly debundled as shown in the two lower weight percentages. In the 10 wt% MWNT TEM image, there is a high density of MWNTs. These are not in bundle form. The bulk material dispersion is assessed by taking TEM images at different locations and observing similar images. Again, it does not appear to be any preferred orientation.

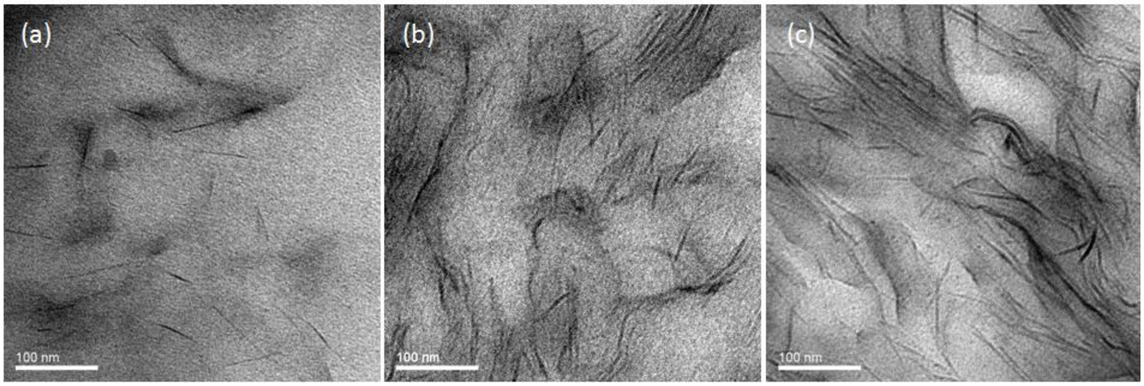

Figure 2.11. TEM images of (a) 2.5% (b) 5% and (c) 10% Cloisite 30B in TPUN.

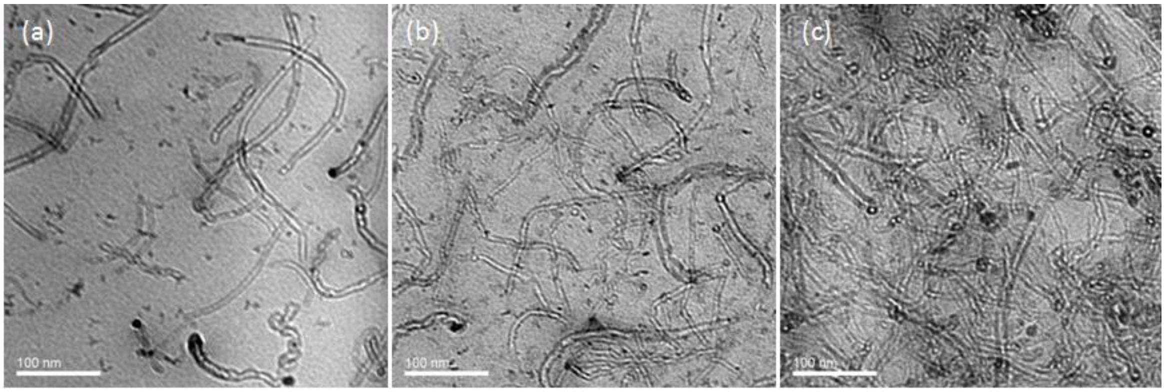

Figure 2.12. TEM images of (a) 2.5% (b) 5% and (c) 10% MWNT in TPUN.

2.5. POLYMER NANOCOMPOSITE MATERIAL PROPERTIES

2.5.1. Density

These materials are mixed based on weight percentages rather than volume percentages because of the large variation between the tightly and loosely packed bulk densities. According to each respective technical data sheets the bulk densities are: 0.5-0.8 g/cc (Desmopan® 6065A), 0.016-0.048 g/cc (CNF), 0.05-0.15 g/cc (MWNT), and 0.23-0.36 g/cc (nanoclay). The actual densities of Desmopan® 6056A and Cloisite® 30B are also listed as 1.084 g/cc and 1.98 g/cc respectively. The pellet densities are measured using an Ultrapycnometer 1000, from Quantachrome, by Patrick Ruth from AFRL. The experiments were tested on 2 separate days. The first day the neat TPU, MWNT PNCs, and nanoclay PNCs were measured. There is a 1% difference between two measurements of the neat TPU. The three additives increase the density of the PNC in a very similar fashion. It can also be noted that at the higher weight loadings of both the nanoclay and CNF samples the densities tangent from the linear density trend. It may be expected based on the nanomaterial bulk densities that the nanoclay PNC would increase in density more than the MWNT. This however is not necessarily true since the bulk density provided is that before the nanoclay is exfoliated and the MWNT is debundled. One factor that is not taken into account is the amount of water these samples may absorb.

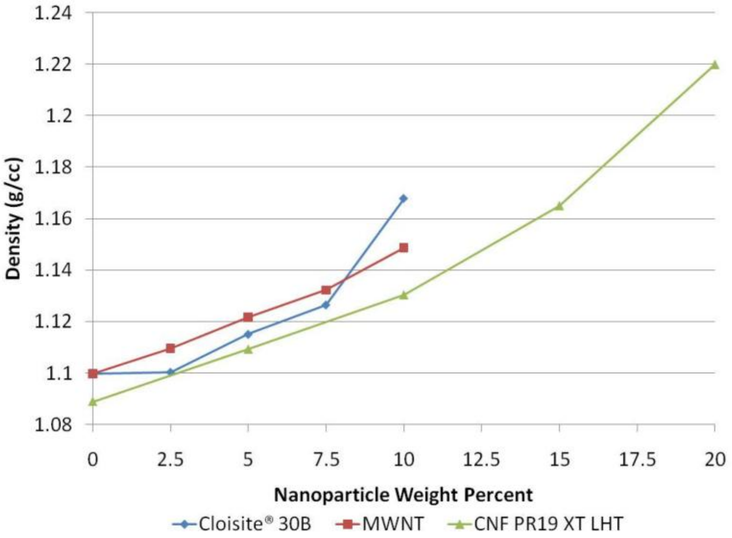

Figure 2.13. Density of PNC with respect to nanoparticle loading.

2.5.2. Hardness

A type A durometer is used to measure the hardness of these TPU specimens, according to ASTM D2240-05. The ASTM standard allows both a stack and single material to be used in the hardness measurement as long as the total thickness is at least 6 mm (0.24”). A durometer is a spring loaded gauge which measures the response of a material when pressed. The dimensions of a plate specimen which is created by injection molding is 10.16 cm x 10.16 cm x 3.175 mm (4” x 4” x 0.125”). Thicker specimens 12.7 mm (½”) thick are created for performance tests which will be described later in the dissertation. Instead of creating a new mold to be used in injection molding these thicker specimens, a few of the thinner samples (3.175 mm thick) are compression pressed at elevated temperatures. Due to the fact that these specimens are thick, they are first placed in a furnace and heated 20°C below the pressing temperature before transported to the hot compression press; these thick samples were pressed by Dr. Wissler. To meet the thickness requirement, the hardness test is performed on two stacked 3.175 mm thick samples and one of the thicker 12.7 mm molded samples. Five points of measurement are taken: one at the center of the specimen and one at each of the four edges 2.54 cm (1") away from the center, Figure 2.14.

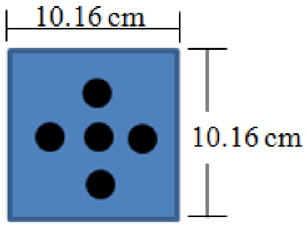

Figure 2.14. Hardness test locations.

The pressed samples are labeled as "single" and the samples which are measured with a stack of 3.175 mm thick samples are labeled as "stack". The "stacked" samples have a higher hardness measurement compared to the "single" specimens, due to the fact that during the compression pressing process small porous pockets may be created. Due to the thickness of the specimen, during the compression process it is difficult to eliminate all the thermal gradients within a specimen. The clay additives substantially increase the hardness of the PNC. At 10% loading, the additives increase the "stacked" sample hardness of the TPU by 29%, 24%, and 20% with the nanoclay, CNF, and MWNT additives respectively.

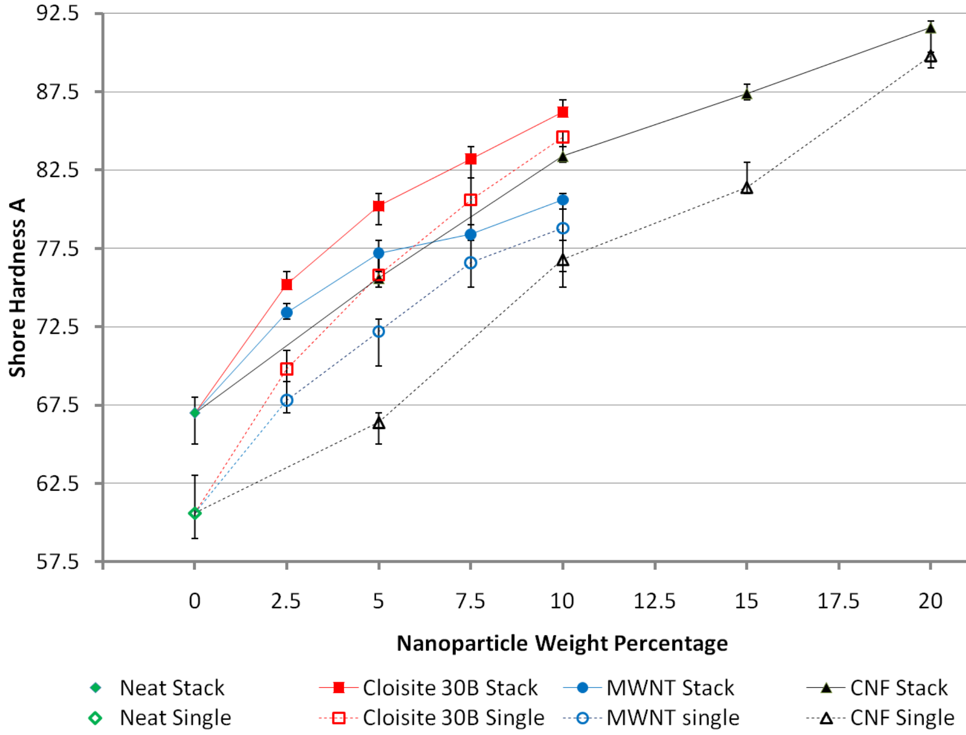

Figure 2.15. Shore hardness of single and stack specimens.

2.5.3. Electrical Conductivity

The specific application for this project is ablation. However nanomaterials are effective at enhancing multiple material properties. For example, the carbon-based additives provide electrical conductivity to the TPU. A four point electrical conductivity test is performed to test the surface conductivity. This work was performed with the assistance of an undergraduate research assistant, David Chen, using the laboratory equipment of Dr. Rodney Ruoff, Figure 2.16. The current setup is limited to be able to measure materials with relatively high electrical conductivity so measurements are only able to be obtained for the TPU w/ 20% CNF, 7.5% MWNT, and 10 wt% MWNT formulations. The specimens tested are thin films, less than 0.254 mm (0.01”) in thickness. These films are made by compression pressing injection molded samples 10°C above the neat TPU's melt temperature. The strip of the film is cut such that a 2.54 cm (1") length material is tested. The sheet resistance is proportional to the voltage to current ratio. Two correction factors are used: CF1 depends on the relationship between the probe spacing, length, and thickness. Because the probe length of the sample is much greater than both the probe spacing and sample thickness the correction factors asymptote to unity and 4.53, equation 2.1, where □ is a non-dimensional unit representing that the measurement is that of surface resistivity.

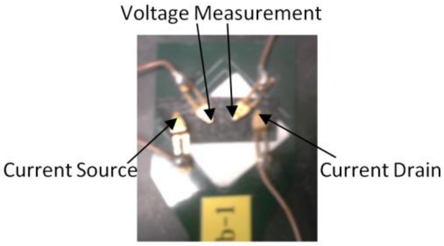

Figure 2.16. Four point probe test setup.

$$\rho_{\square} = \frac{\pi}{\ln(2)}\frac{V}{I} = 4.53\frac{V}{I} \tag{2.1}$$

Multiple samples are tested for each formulation. In each experiment the current source is incremented by 20 nA starting from a setting of -1000 nA up to 1000 nA, so for each experiment 100 data points are collected. At each current setting the voltage across the two center probes is measured. It is important that the four probes are in line with one another such that accurate current and voltage flows are measured. At the start of the experiment the voltage to current correlation is not linear, Figure 2.17. The results for the measurements obtained are shown in Figure 2.18 and are taken when a linear correlation between the voltage and current is observed. The measured electrical resistivity of these three materials is low enough to be used for electrostatic discharge (ESD) applications. There are a few projects related to aerospace vehicles which are interested in finding light weight materials which fulfill the ESD requirement.

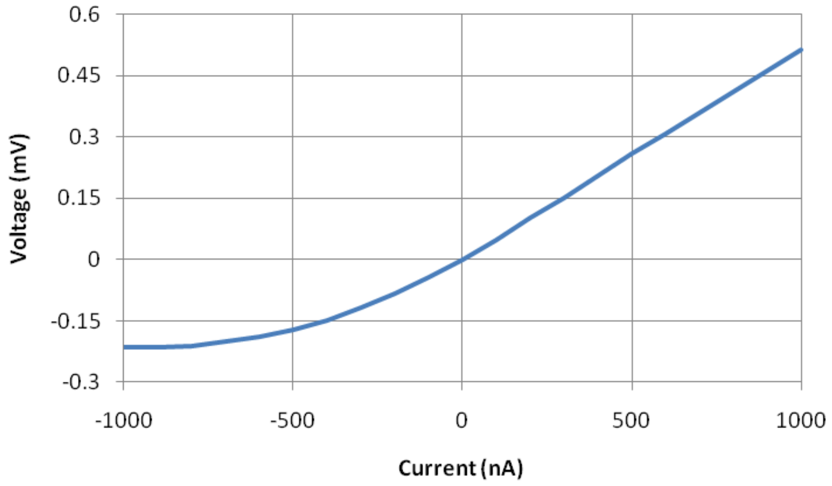

Figure 2.17. Representative four point probe test results.

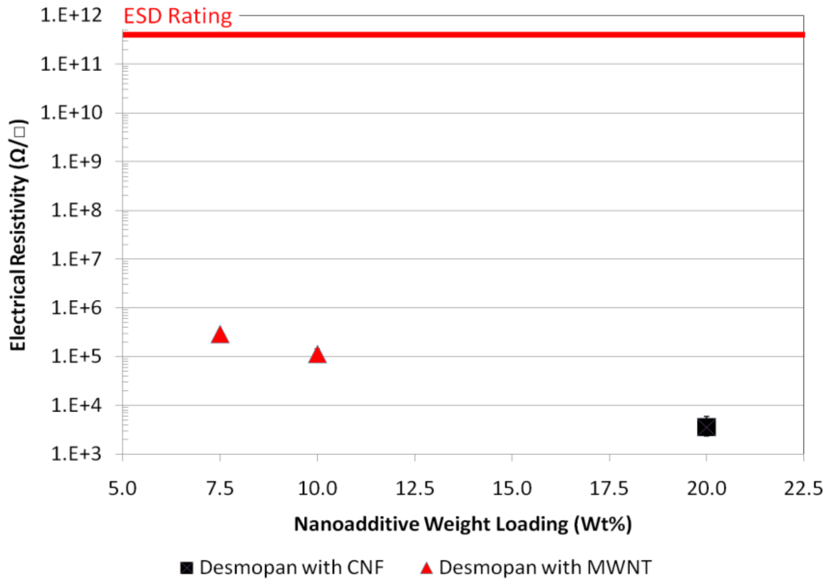

Figure 2.18. Surface electrical resistivity of Desmopan® 6065A CNF and MWNT.

2.6. CONCLUSION

The three nanomaterials and the TPU used in this study are described in this chapter. The materials are processed using twin screw extrusion and are injection molded and compression pressed to specific test specimen sizes. Good dispersion is observed in the materials by using TEM to examine the nanoclay and MWNT samples. In addition the nanoclay sample is studied under WAXD and none of the samples tested were found to have a d-spacing that matched the platelet form of stacked platelet Cloisite® 30B nanoclay.

Each material's density is shown to increase with weight loading at approximately a linear rate. At higher weight loadings, the nanomaterials increase the PNC's density at a more significant rate. Viscosity is also observed to reach a limit of the injection molding process, as specific specimens are not molded well. Hardness measurements are also observed to increase as weight loading is increased. Specimens that are stacked are measured to have a higher stiffness than samples that are compression pressed, due to the fact that increased porosity between the specimens creates a softer response to the durometer. Lastly, the multifunctional properties of these nanomaterials are observed as low electrical resistivity is measured. In the high weight loading CNF and MWNT samples, ESD requirement is achieved. These various enhancement properties are one of the main attractions to considering PNCs for this study. The work done here may apply to ablation processes but also may be relevant to other engineering applications due to the material enhancements in different areas. In the next chapter a series of degradation experiments is used to study the thermal stability of the different PNCs.

Chapter 3. Thermal Degradation Analysis

3.1. INTRODUCTION

A common and useful polymer characterization tool is a thermogravimetric analysis (TGA) instrument. A small mass balance in a furnace measures the changes in mass of a sample under specified thermal conditions. Traditionally the furnace is either raised to an isothermal temperature or heated at a constant temperature rate. These two methods are useful to determine thermal decomposition kinetic parameters. The TGA experiments performed in this dissertation are all dynamic heating processes. The purpose of these experiments is to understand how the different materials degrade and the enhancements in thermal stability that the nanocomposites provide. Thermal stability is measured by the onset temperature. The onset temperature is the temperature at which the maximum weight loss tangential and the zero weight loss line intersect.

Traditional TGA equipment measures heating rates on the order of 20^{o}C/min. However actual ablation heating rates can be on the order of 10,000^{o}C/min. Different heating rates are examined to better understand how the thermal response at low heating rates can be correlated to that of higher heating rates.

Initial tests are performed with a traditional TGA instrument. At the time of these experiments only the MWNT and nanoclay samples were available. The experiments performed here serve to understand how TGA data can effectively be used to understand the different material degradation properties. These experiments and results are presented in section 3.3. To better understand the effects of high heating rates. A TGA instrument with the capabilities of higher heating rates is also used to perform tests on all three PNC families. Some of these materials are heated at upwards of 500^{o}C/min. The results and testing methodology performed with these experiments are presented in section 3.4. Finally a joint TGA/DSC instrument is used to test the materials. The additional DSC component measures the heat flow from the sample. This measurement is useful to measure the specific heat of the sample.

3.2. DEGRADATION OF POLYURETHANE

To understand the degradation of these materials it is also important to understand how the polymer degrades. Dyer investigated the degradation of pure TPUs with Newborn (1958), Wright (1959), and Read (1961) identifying three types of TPU decomposition reactions: 1) depolymerization, 2) secondary dissociation 3) and carbon dioxide elimination.

As mentioned in section 2.2.1. TPU consists of a hard diisocyanate (OCN-R-NCO) and a soft polyether (HO-R’-OH); Lattimer, Polce, and Wesdemiotis (1998). These two segments are joined by chain extenders (HO-R”-OH) to form the polyurethane chain $\left[\text{O–R'–O–CO–NH–R–NH–CO–O–R''–O–CO–NH–R–NH–CO}\right]_n$. The depolymerization process dissociates the TPU (-R’–O–CO–NH–R-) to its original components: alcohol (-R’ OH) and isocyanate (-R–NCO). Secondary dissociation involves the dissociation of the TPU ($\text{-R'–CH}_2\text{–CH}_2\text{–O–CO–NH–R-}$) to primary amine ($\text{-R–NH}_2$), carbon dioxide ($CO_2$), and olefin ($\text{CH}_2\text{=CH–R'–}$). Lastly elimination of carbon dioxide from the TPU (-R’–O CO—NH—R-) produces a secondary amine (-R—NH-R’). The reactions which will be observed in the TGA data will show a two step reaction. The first step is associated to the hard segment and the second step is associated to the soft segment. The ratio of hard to soft segments is a decisive factor in determining how the material degrades.

The nanomaterials are expected to significantly change the degradation of the PNC. Two mechanisms are proposed as the nanomaterials contributing factors. First, the nanomaterials may act as a gaseous barrier. In this case the pyrolysis gases produced are hindered from easily traveling through the bulk material. Second, the nanomaterials may act as a "hard segment" in a similar way that the diisocyanate segment serves as an anchor for the polyether. When the depolymerization process occurs, the alcohol products can use the nanomaterials as an "anchor". Since the nanomaterials do not degrade in the applied conditions they will serve as anchors better than the diisocyanate which does degrade. These two proposed mechanisms are explored in evaluating the properties of the PNCs in each characterization section.

3.3. TRADITIONAL TGA EXPERIMENTS

The traditional TGA setup used is a TGA7 from Perkin Elmer, Figure 3.1. The sample is heated by an electric wound furnace. The space above the furnace contains both the microbalance and is also where the exhaust line is drawn from. Attached to the microbalance is a thin hang down wire. At the lower end of the hang down wire is a hook which the platinum sample pan is hung off of. The loading tray is useful to steadily transport the sample pan to the hand down wire. The chances of bending or breaking the hang down wire are high if careful loading of the sample pan is not performed. In fact this had been an issue since the instrument is a community facility. A bent wire can cause problems with the microbalance measurements, so careful inspection and measuring of the sample mass with an external mass balance is necessary. In addition, the exhaust from these materials gives off a sticky residue that requires maintenance of the upper furnace assembly and the hang down wire. When the hang down wire sticks to the furnace walls inaccurate mass loss results are obtained.

After the sample pan is hung, the lower furnace assembly is raised. A nitrogen purge of 30 minutes is necessary to remove all air that enters the furnace during sample loading. It has been well documented that low percentages of oxygen content can drastically change the decomposition process of a TGA experiment. A 20 ml/min nitrogen purge is maintained though the duration of the test.

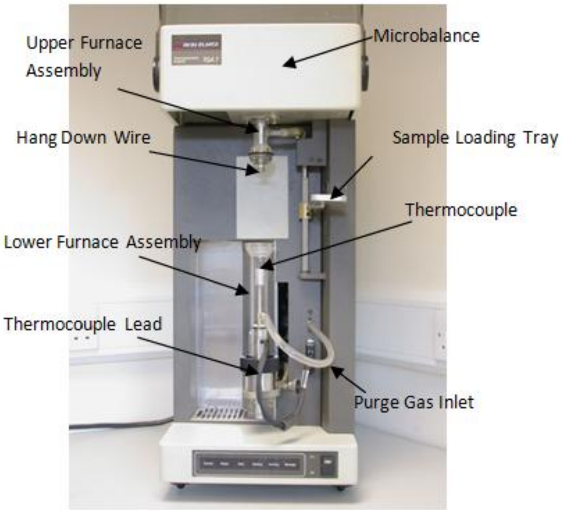

Figure 3.1. Perkin-Elmer TGA7. (http://www.materials.co.uk/tga.htm)

3.3.1. Calibration

Baseline runs are performed by running an empty sample pan at specific heating rates. This is necessary to perform in order to ensure that no drift in the microbalance is occurring. In addition to ensuring that the issues with the hang down wire are resolved to provide accurate mass measurements, the thermal measurements must also be calibrated.

The Chromel/Alumel thermocouple is located in the lower furnace assembly. It is positioned directly below but not in contact with the sample pan. It is important to note that the calibration performed is that of the system rather than that of the thermocouple.

The thermocouple itself has been calibrated by the manufactures. The calibration required is to accurately determine the sample temperature based on the thermocouple temperature. This must be performed at each heating rate for accurate results.

The four calibration materials used are: alumel, nickel, perkalloy, and iron. A reference material is placed in the sample pan and heated at a specific heating rate. During this time a magnet is placed under the sample pan. When the reference material reaches its true Curie point temperature the effects of the magnet will be eliminated. Above the Curie point temperature, the ferromagnetic changes to a paramagnetic, the reference material is no longer magnetic. This is based on the fact that below the Curie point temperature the magnetic moments of the material are aligned in parallel. Above the Curie point temperature however the magnetic moments are disordered. The Curie point temperature is a 2nd order phase transition. A correction is made to the computer if a shift larger than $\pm 2^{o}$C is measured.

3.3.2. Results

The samples used were cut from the pellets produced from the twin screw extrusion process. The samples were maintained between 13-16 mg for consistency between the experiments. The samples were heated at 10^{o}C/min, 20^{o}C/min, 40^{o}C/min, and 100^{o}C/min between 100^{o}C and 900^{o}C.

Figure 3.2 shows the TGA results of the neat TPU. As with typical TGA experiments, the increased heating rate increases the sample's mass loss rate, and shifts the degradation curves to the right of the graph, higher temperatures. This is also observed in the time derivative TGA (DTGA) curves in Figure 3.3, the peak DTGAs and DTGA temperatures increase as heating rate increases. The different heating rate TGA curves cross when the remaining sample mass is less than 20% of its original mass. As the heating rate increases, the remaining weight percent at which the TGA changes slope also increases. For example, in the 10°C/min neat TPU heating rate experiment the curve shifts at 383°C, and this occurs in the 100°C/min heating rate at 457°C. The degradation after the slope changes is slow in comparison to the degradation before it.

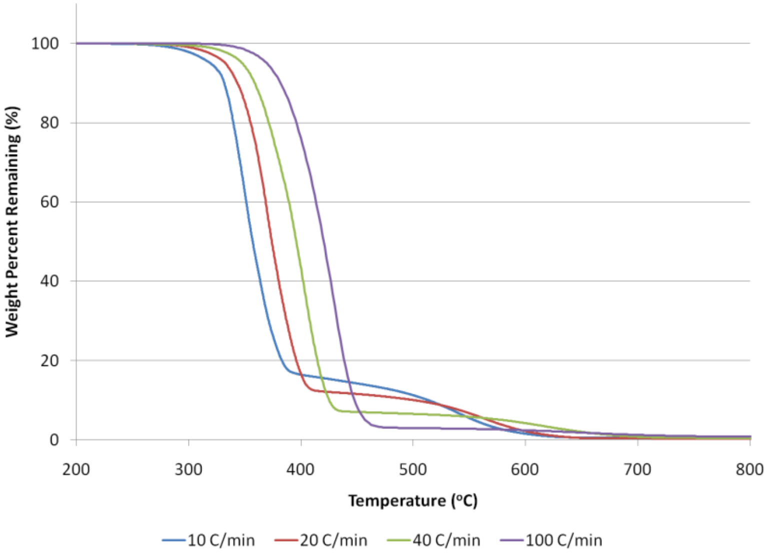

Figure 3.2. Neat Desmopan® 6065A TGA mass loss at different heating rates.

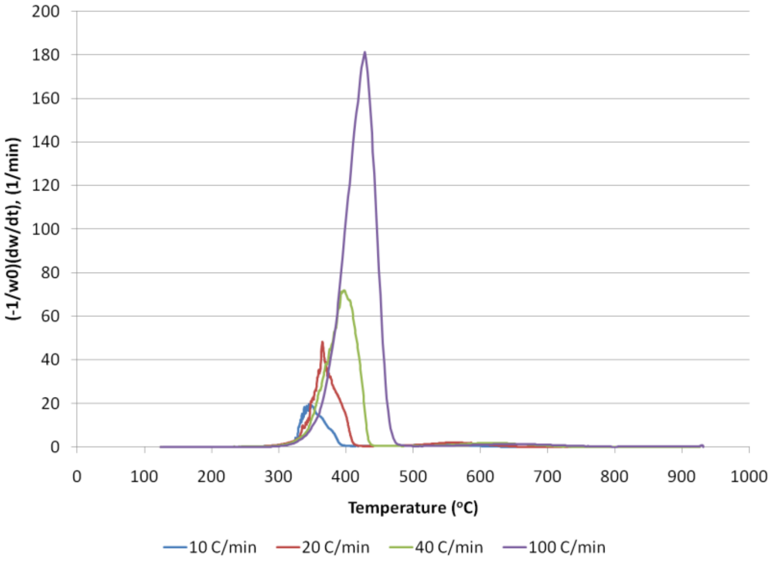

Figure 3.3. Neat Desmopan® 6065A DTGA rate of mass loss at different heating rates.

Each of the nanoclay and MWNT PNC samples are tested with the same heating rates. TGA and DTGA curves of all eight formulations are shown in Figure 3.4 to Figure 3.7. The shift in peak DTGAs and peak DTGA temperatures are also observed in these two materials as well as the fact that at high temperatures the lower heating rate experiments TGA curves cross. Before the discussed curve shift occurs, two distinct slopes, reactions, are observed. These two reactions are more distinctly observable in the PNC curves than in the neat TPU TGA curves.

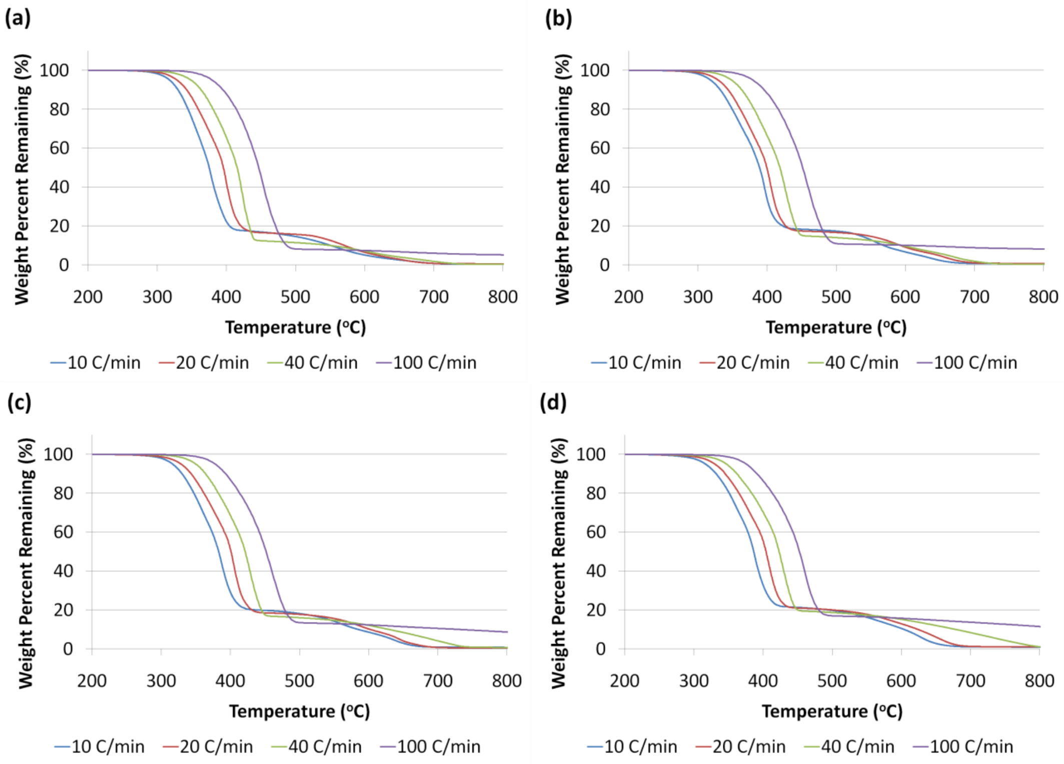

Figure 3.4. MWNT PNC TGA mass loss at different heating rates (a) 2.5% MWNT, (b) 5% MWNT, (c) 7.5% MWNT, and (d) 10% MWNT.

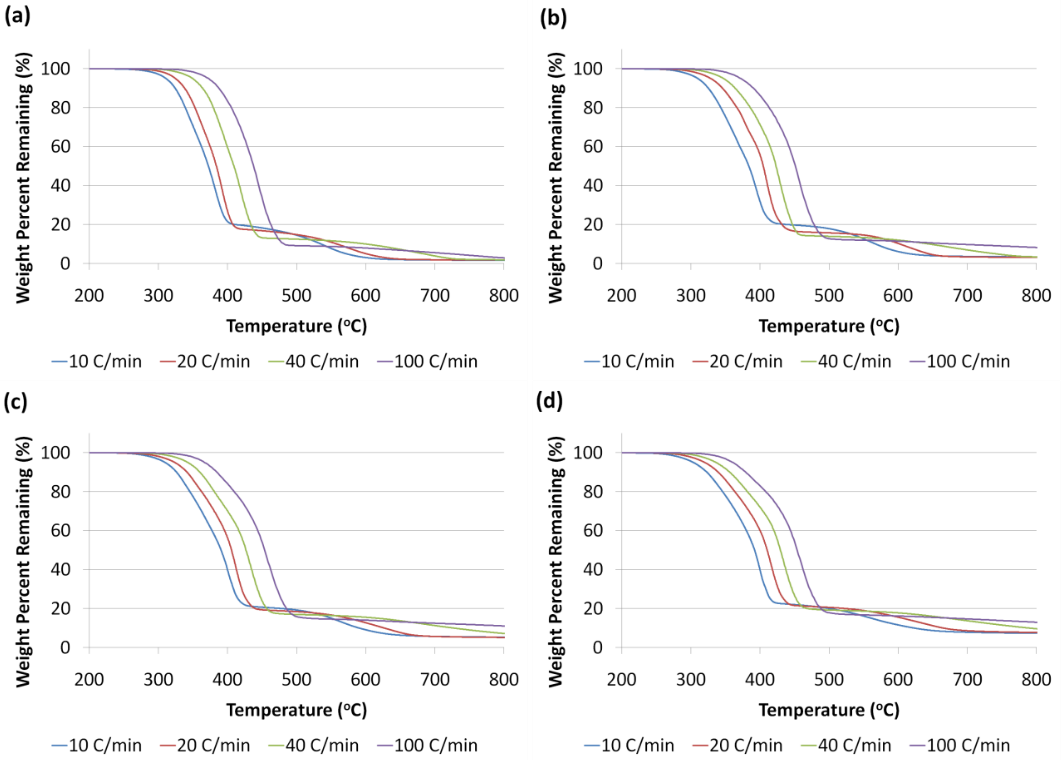

Figure 3.5. Nanoclay PNC TGA mass loss at different heating rates (a) 2.5% Nanoclay, (b) 5% Nanoclay, (c) 7.5% Nanoclay, and (d) 10% Nanoclay.

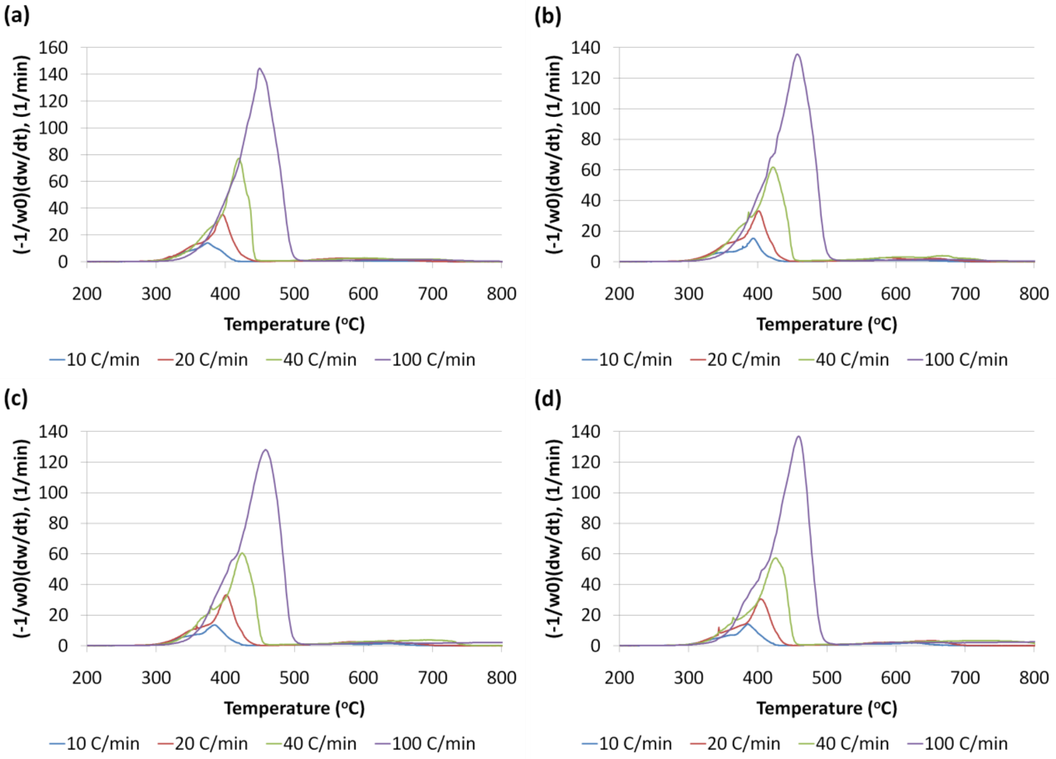

Figure 3.6. MWNT PNC DTGA rate of mass loss at different heating rates (a) 2.5% MWNT, (b) 5% MWNT, (c) 7.5% MWNT, and (d) 10% MWNT.

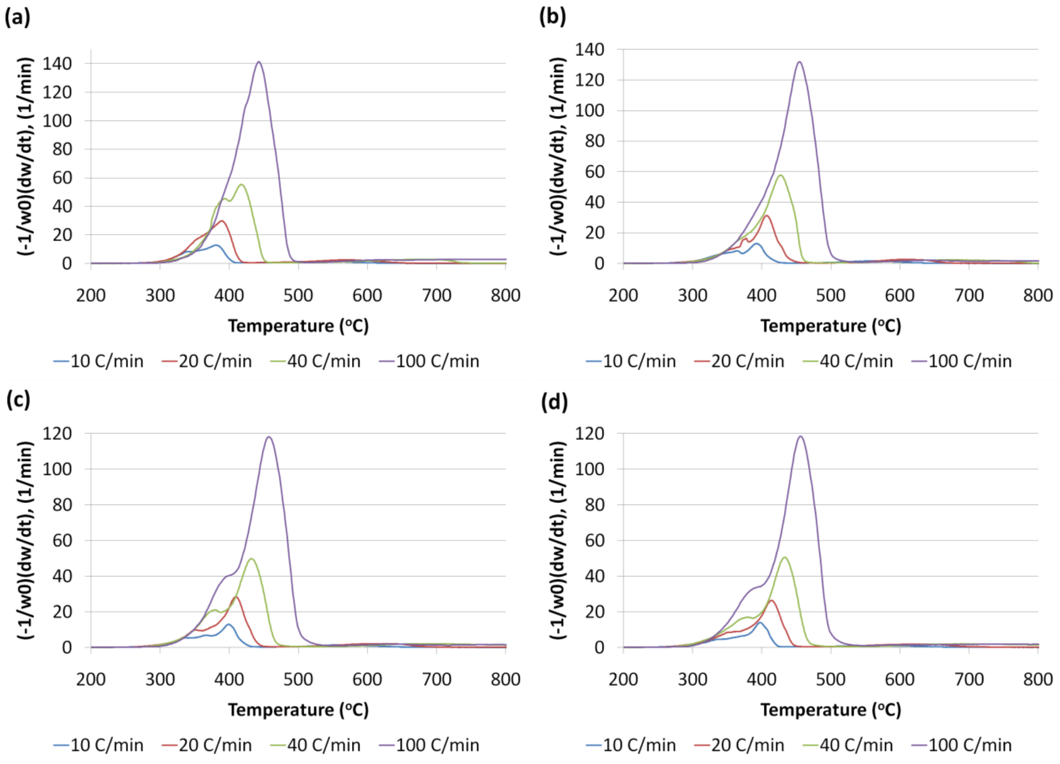

Figure 3.7. Nanoclay PNC DTGA rate of mass loss at different heating rates (a) 2.5% Nanoclay, (b) 5% Nanoclay, (c) 7.5% Nanoclay, and (d) 10% Nanoclay.

A comparison of the neat TPU with the nanoclay PNC at the low heating rate, 10^{o}C/min, is shown in Figure 3.8 and Figure 3.9. The remaining char material residue at 800^{o}C is 0.4%, 1.6%, 3.4%, 5.3%, and 7.3% for neat TPU, 2.5% nanoclay PNC, 5% nanoclay PNC, 7.5% nanoclay PNC, and 10% nanoclay PNC, respectively in the 10^{o}C/min experiments. A comparison of the neat TPU with the nanoclay PNC at the high heating rate, 100^{o}C/min, is shown in Figure 3.10 and Figure 3.11. And 0.78%, 2.8%, 8.2%, 11%, and 13% for neat TPU, 2.5% nanoclay PNC, 5% nanoclay PNC, 7.5% nanoclay PNC, and 10% nanoclay PNC, respectively in the 100^{o}C/min experiments. This means that at the higher heating rates slower reactions are not capable of occurring, resulting in about twice the amount of residue left after low heating rate experiments are conducted.

The DTGA curve of the 10^{o}C/min neat TPU shown in Figure 3.9 has a shoulder at about 360^{o}C. This separates the two distinct reaction regimes. In the neat material, the first DTGA peak is higher than the second. With the addition of nanoclay additives, the first DTGA peak is significantly lower than the first neat TPU DTGA peak. In each of the nanoclay DTGA curves, the first DTGA peak is lower than the second. Nanoclay additives have high aspect ratios which aid in acting as a pyrolysis barrier. This can serve multiple functions which can be associated with the changes in TGA/DTGA curves: 1) the nanoclay may act as an anchor preventing degradation process from occurring, or 2) after the material has degraded and begins to degas the nanoclay may act as a gaseous barrier. With increasing nanoclay loading, the first DTGA peak decreases and the second peak upper temperature range is extended. The two distinct reactions are less observable at higher heating rates as the reactions themselves may be occurring at the same time since the reaction rates remain constant, however higher temperature reactions are initiated more quickly due to the increased environmental thermal heating rate. The nanoclay PNC DTGA curve at 100^{o}C/min heating rate enhances the material to such a degree that the two reactions are still observed.

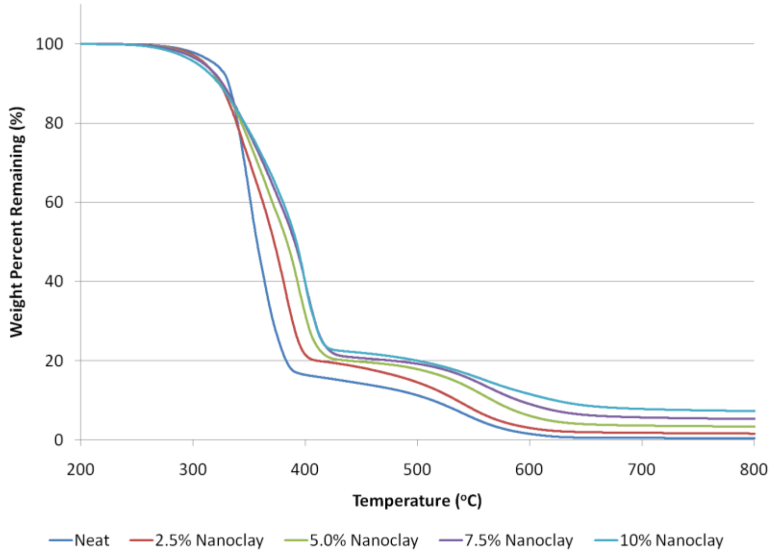

Figure 3.8. Nanoclay PNC TGA mass loss at 10°C/min.

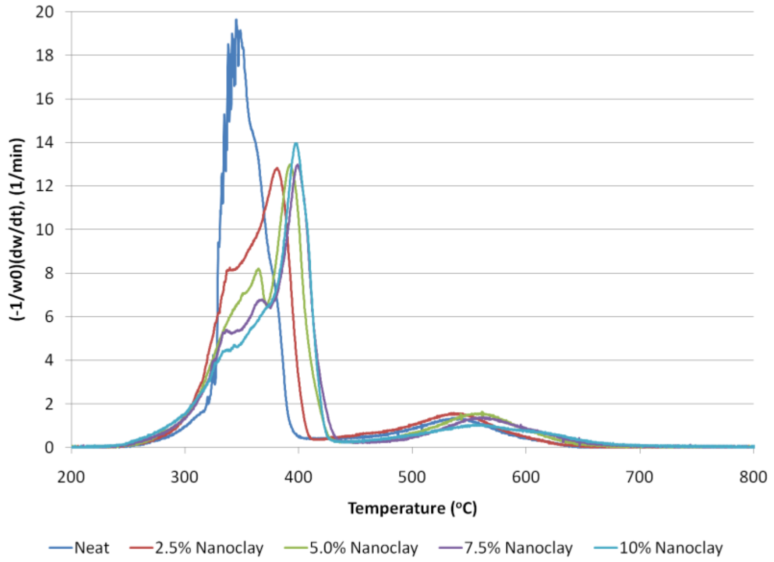

Figure 3.9. Nanoclay PNC DTGA rate of mass loss at 10°C/min.

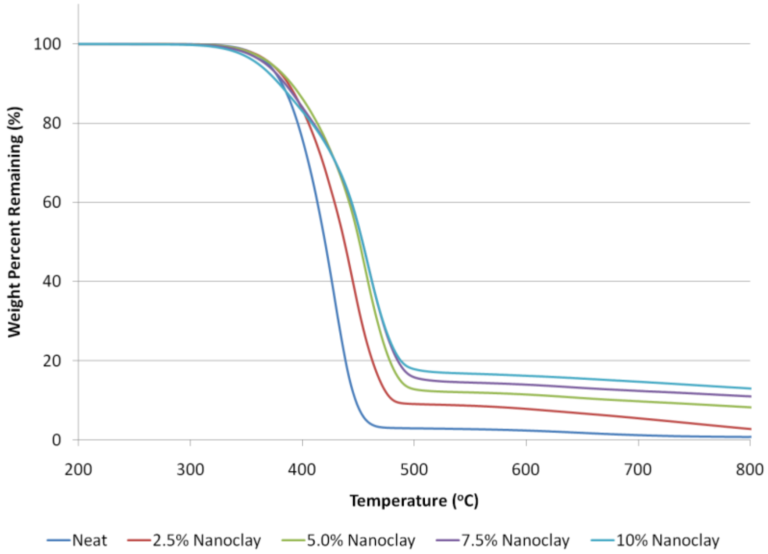

Figure 3.10. Nanoclay PNC TGA mass loss at 100^{o}C/min.

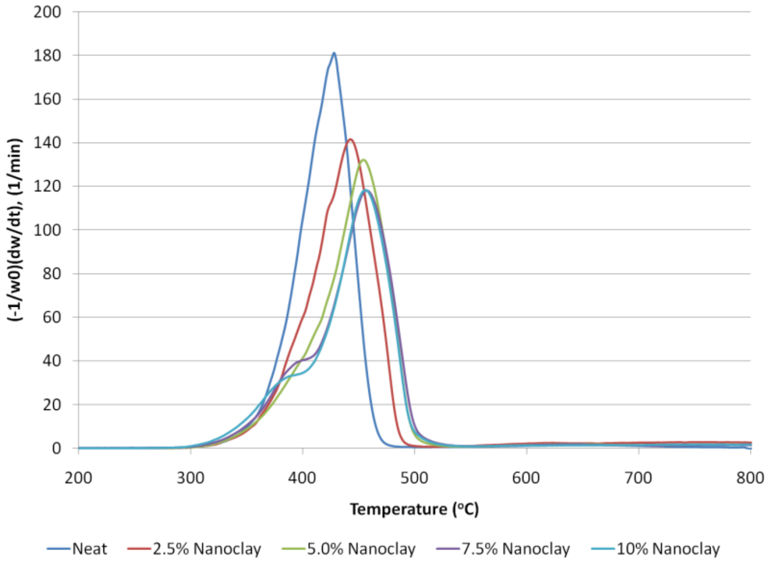

Figure 3.11. Nanoclay PNC DTGA rate of mass loss at 100^{o}C/min.

Figure 3.12 and Figure 3.13 are TGA/DTGA plots of TPU with MWNT at 10^{o}C/min. The remaining char residue at 800^{o}C is 0.4%, 0.43%, 0.6%, 0.78%, and 0.93% for neat TPU, 2.5% MWNT PNC, 5% MWNT PNC, 7.5% MWNT PNC, and 10%

MWNT PNC, respectively. At 100^{o}C/min in figure 3.14 and Figure 3.15 the remaining char residue at 800^{o}C is 0.8%, 5.2%, 8.2%, 8.6%, and 11.2% for neat TPU, 2.5% MWNT PNC, 5% MWNT PNC, 7.5% MWNT PNC, and 10% MWNT PNC, respectively. Similar to the enhancements made from the nanoclay additives, the MWNT PNC curves have a low first DTGA peak and a higher second DTGA peak.

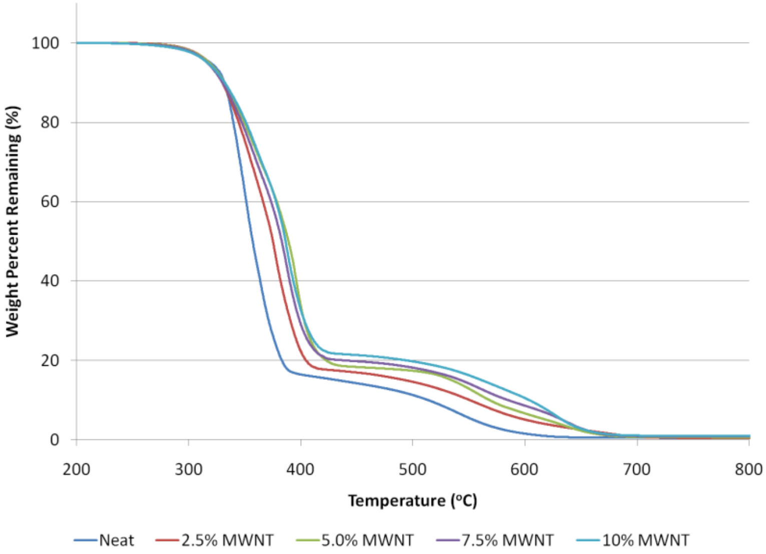

Figure 3.12. MWNT PNC TGA mass loss at 10^{o}C/min.

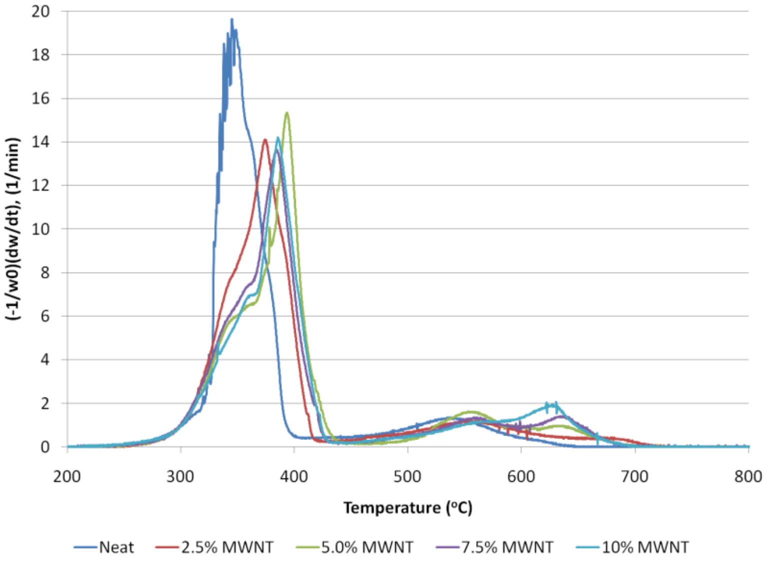

Figure 3.13. MWNT PNC DTGA rate of mass loss at 10^{o}C/min.

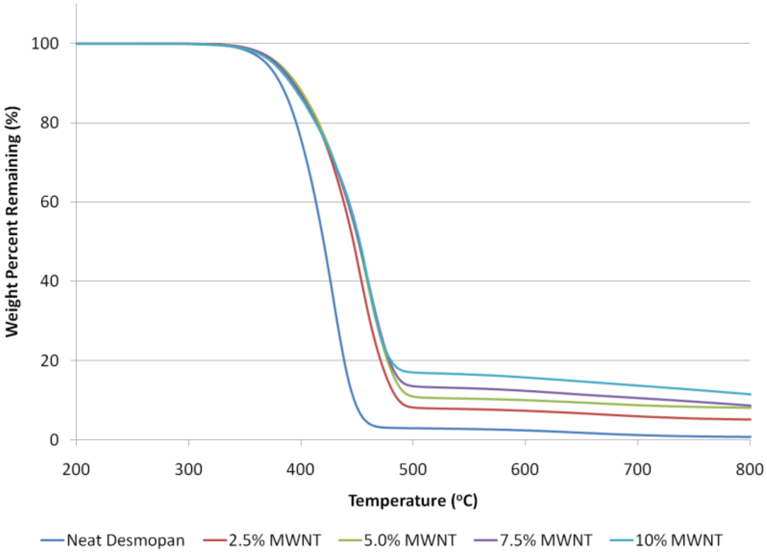

Figure 3.14. MWNT PNC TGA mass loss at 100^{o}C/min.

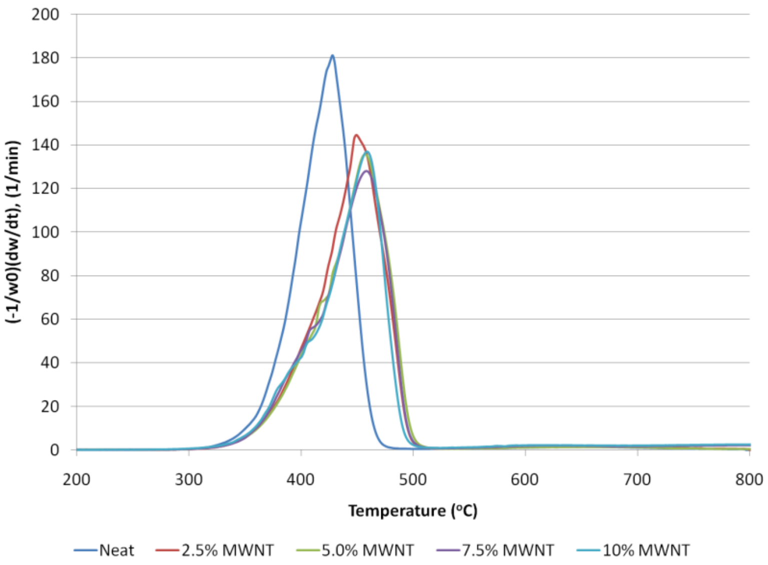

Figure 3.15. MWNT PNC DTGA rate of mass loss at 100°C/min.

The peaks in the DTGA curves above 500°C are not well understood. The reactions are not expected to be discontinuous in this fashion. This may be a system effect of higher heating rates or thermal effects of the mass balance not yet resolved. In the higher heating rate experiments, the material's mass continues to steadily drop at temperatures above 800°C which is also not expected and is likely due to the fact that gaseous material condenses on the hang down wire and is slowly decomposes. The neat TPU at 100°C/min drops an additional 0.5% and the PNCs lose between 1 to 3.5% more material when continued heating to 1000°C.

The onset temperature, Figure 3.16, of the highest weight loadings of MWNT and nanoclay show that the additives improve the PNC's thermal stability by 30°C and 20°C in the 10°C/min and 100°C/min heating rate experiments, respectively. The temperature at which 50% of material remains increases from 357°C in the neat TPU 10°C/min experiment to 392°C and 386°C in the 10% nanoclay and 10% MWNT PNC samples, respectively. At the highest heating rate, 100°C/min, the neat material degrades to 50% at 420°C. The 10% nanoclay and 10% MWNT PNC reach 50% remaining mass at 454°C and 452°C, respectively. The analysis performed on these materials show that the thermal stability of these materials are enhanced. The PNC degradation process is also shown to be different than the neat TPU. Two distinct reactions are observed. The first DTGA peak in the PNC materials is lower than the second DTGA peak. This first peak also decreases as nanomaterial loading increases. With additional nanomaterial loading, the second peak does not drastically increase, however the temperature at which the second reaction ends does increase.

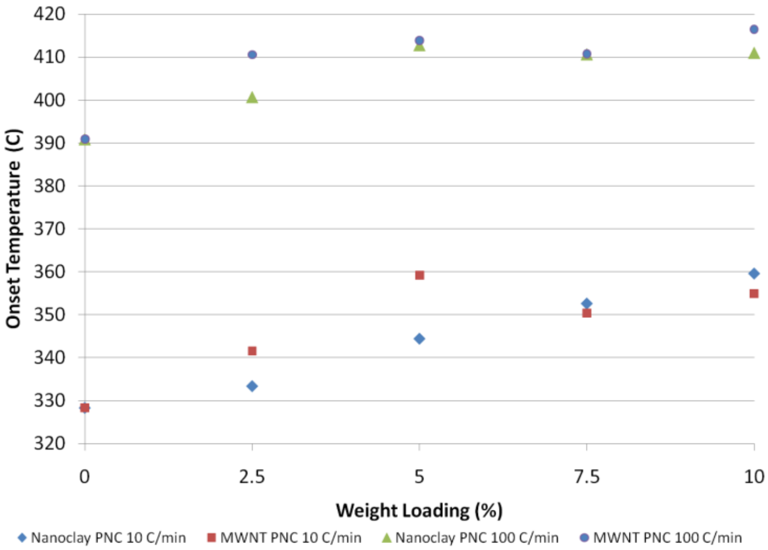

Figure 3.16. Onset temperature of neat TPU, MWNT and Clay PNC @ 10 and 100°C/min.

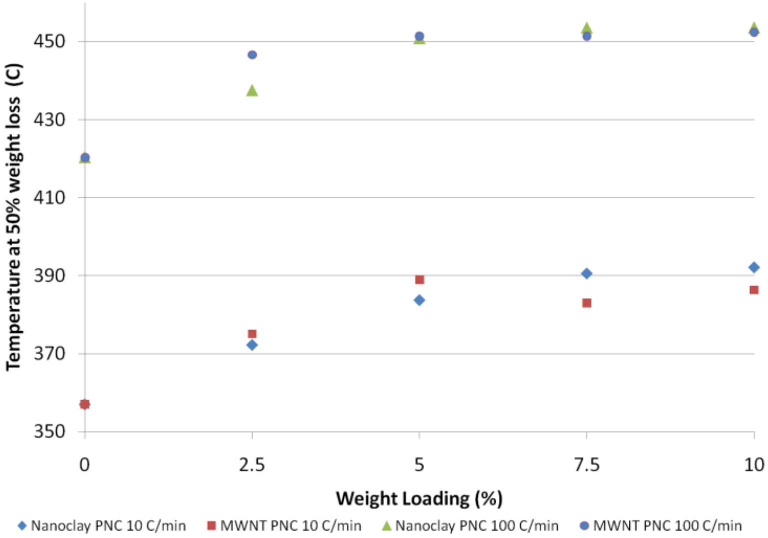

Figure 3.17. Temperature at 50% remaining weight of neat TPU, MWNT and Clay PNC @ 10 and 100 ^{o}C/min.

3.4. HIGH HEATING RATE TGA

In a rocket ablative environment heating rates are in the range of 10,000^{o}C/min. A TGA with higher heating rate capabilities, 500^{o}C/min is used to better understand how the thermal degradation rates will be achieved in ablative environments. In addition, obtaining higher heating rate TGA data can be used to see how well kinetics obtained from lower heating rate TGA can be extrapolated to higher heating rate TGA curves.

The Q5000 IR TGA from TA Instruments is capable of these conditions. The reason that this is possible is that the furnace setup is oriented with four identical IR heat lamps, Figure 3.18. In addition, symmetrically curved surfaces which they call “multi-elliptical reflectors” serve to increase the controlled heating capabilities of this furnace.

The purge gases in this experimental setup flow over the sample pan and exit on the other side of the furnace. The exhaust nitrogen purge gases are maintained at 25 ml/min. The purge exhaust is constantly checked for cleanliness to ensure that the purge flow is continuous and not restricted. Periodically, the exhaust pipe is needed to be cleaned due to condensation of exhaust materials. The outer layer of condensed material tends to be char like substances whereas the center often has a yellowish color material possibly from the TPU or nanoclay PNCs. It is suggested that in future tests the exhaust pipe be heated so that less material can be deposited on its surface. The mass balance setup was opened and checked for cleanliness as well. The hang down wire was found to be clean. One reason that this might be the case is that baffles on both the hang down wire setup as well as below the thermocouple assembly in the lower furnace assembly are present in order to prevent the purge/exhaust gases from entering the sensitive equipment.

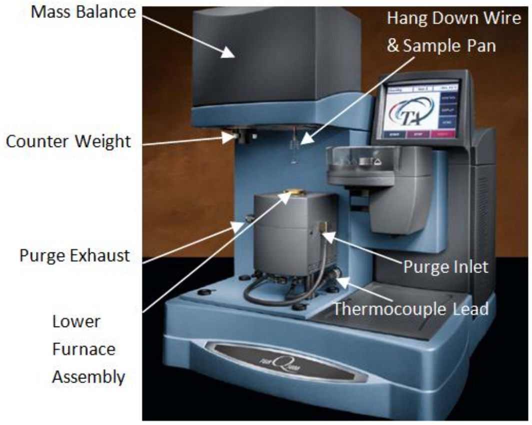

Figure 3.18. Q5000 IR TGA. (TA Instruments Product Brochure)

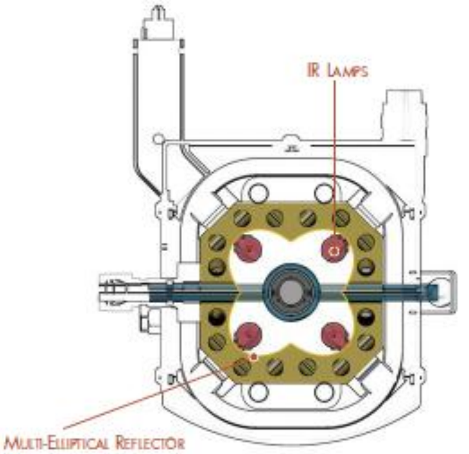

Figure 3.19. TGA Q5000 IR heat lamp arrangement. (TA Instrument Product Brochure)

3.4.1. Calibration

Calibration of the instrument is again performed with the Curie point calibration methodology. In this setup an electromagnet is already in the instrument. Calibrations were initially performed using reference bar materials. However this is not the best method of calibration since in these tests the PNC samples tested are pressed thin films. The calibration using bars is a poor match especially when calibrating the higher heating rate experiments as the thermal response of the material is largely a factor of the sample thickness.

Instead, calibration is performed on Alumel, Nickel, Ni83Co17, and Ni63Co37 thin foils with reference Curie point temperatures of 152.6°C, 358.2°C, 554.4°C, and 746.4°C, respectively. Each heating rate must be calibrated separately as the effect is different for each in each different temperature regime. An electromagnet below the sample pan is turned on at the beginning of the calibration, Figure 3.21. The mass balance measures the magnetic force of the electromagnet as well as the foil's mass when the foil is below the Curie point temperature. A specified heating rate is entered into the control software and the furnace begins heating the sample material. As the sample temperature is heated past its Curie point temperature an apparent drop in mass is measured. The drop in mass is not a sharp step. Depending on the heating rate it can be a slow gradient. The measured Curie point temperature is determined as the intersect of two tangential lines: 1) the steep drop in mass curve as the reference material losses magnetism and 2) the leveled off curve above the Curie point. An example of this calibration methodology is shown in Figure 3.20.

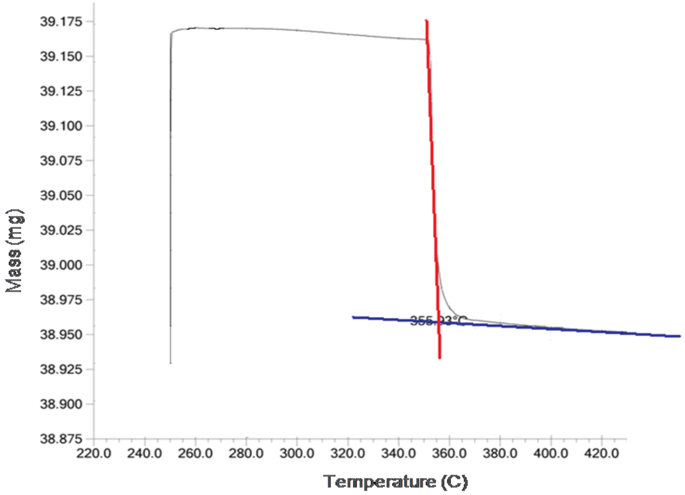

Figure 3.20. Nickel Curie point calibration graph mass vs. temperature.

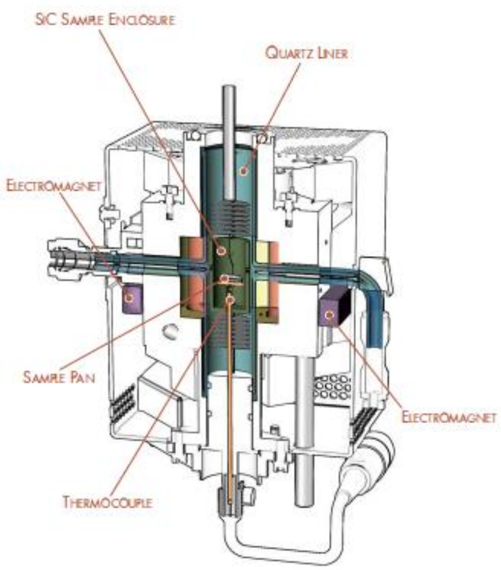

Figure 3.21. TGA Q5000 IR furnace assembly arrangement. (TA Instrument Product Brochure)

Multiple calibrations are performed at each heating rate. The higher heating rate calibrations resulted in a larger range of measured values due to the fact that the ramp rate is so high it takes about 30 seconds to equilibrate to a constant and steady heating rate. The higher heating rate experiments do not equilibrate by the time the Alumel Curie point temperature is reached resulting in far larger uncertainties. The measured Curie point values at each heating rate are shown in Figure 3.22. The results of experiments performed are conducted initially with no calibration. The TGA data is then calibrated with four linear curve fits depending on what temperature range a specific data point is in. Either between: 1) the room temperature and the Alumel Curie point calibration, 2) the Alumel and Nickel Curie point calibration, 3) the Nickel and Ni83Co17 Curie point calibration, and 4) or the Ni83Co17 and Ni63Co37 Curie point calibration.

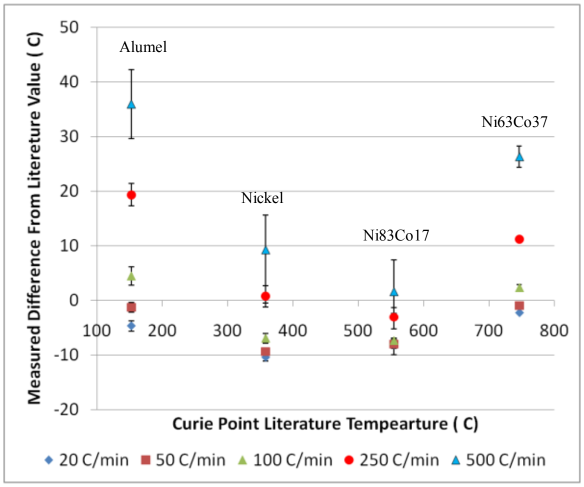

Figure 3.22. Measured Curie point temperatures.

In the furnace assembly, four infrared heat lamps are symmetrically placed around the silicon carbide interior. The thermocouple and sample pan are housed within the silicon carbide, Figure 3.23. The relationship between the reference sample and thermocouple temperatures is dependent on heating rate. At low heating rates the reference sample temperature is higher and at high heating rates the thermocouple temperature is higher. A heat transfer model is created to understand this relationship.

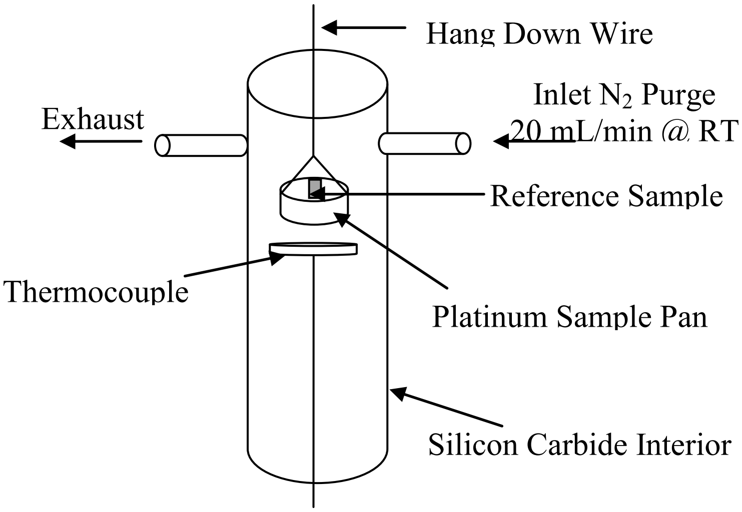

Figure 3.23. Schematic of silicon carbide furnace assembly.

The reference sample and sample pan are modeled as a thin platinum disc, subscript p. The pan has a diameter of 1 cm, mass of 135 mg, and the following thermal properties: thermal conductivity, k_p=71.6 W/mK; specific heat, c_p=0.13 J/gK; and density, ρ_p=21.5 g/cm^3. The thermocouple is also modeled as a 1 cm diameter, 135 mg disc, subscript TC. The thermocouple thermal properties used are of chromel: thermal conductivity, k_{TC}=19W/mK; specific heat, c_{TC}=0.473 J/gK; and density, ρ_{TC}=8.5 g/cm^3. The encasing furnace is a 2 cm diameter 10 cm tall furnace silicon carbide and is referenced to as the wall, subscript w.

The heat equations used in this model for the pan, Eqn. 3.1, and thermocouple, Eqn. 3.2, include radiation from the wall and convection from the gas. The radiative heat transfer between the pan and thermocouple are dominated by these two modes of heat transfer and is neglected from this analysis for simplicity. The nitrogen is assumed to be well mixed. A well mixed approximation, Eqn. 3.3, is used to determine the nitrogen temperature in the system; where, $T_{g_{in}}$ is the temperature of incoming nitrogen (assumed to be at room temperature), A_{cross} is the cross sectional inlet purge area (1 cm diameter), c_N=1.05 J/gK is the specific heat of nitrogen, and $\dot{m}"$=20 mL/min is the mass flow rate of nitrogen purge.

$$m_p c_p \frac{dT_p}{dt} = hA_p\left(T_g - T_p\right) + \epsilon_p \sigma A_{wall}\left(T_w^4 - T_p^4\right) \tag{3.1}$$

$$m_{TC} c_{TC} \frac{dT_{TC}}{dt} = hA_{TC}\left(T_g - T_{TC}\right) + \epsilon_{TC} \sigma A_{wall}(T_w^4 - T_{TC}^4) \tag{3.2}$$

$$A_{cross}\dot{m}" c_N\left(T_g - T_{g_{in}}\right) = hA_p\left(T_p - T_g\right) + hA_w\left(T_w - T_g\right) + hA_{TC}\left(T_{TC} - T_g\right) \tag{3.3}$$

In the model, T_{TC} is set based on the interested heating rate. The unknown values in this system are T_p, pan/sample temperature; T_w, wall temperature; and T_g, gas temperature. Equation 3.3 can be rewritten such that T_g is a function of the two other unknowns. This form of T_g can be substituted into equations 3.1 and 3.2 and simplified to equations 3.4 and 3.5,

$$\frac{dT_p}{dt} = DT_p + ET_w + FT_p^4 + GT_w^4 + H \tag{3.4}$$

$$I(t) = JT_p + KT_w + LT_w^4 \tag{3.5}$$

where, D, E, F, G, J, K, and L are constants and I(t) and H(t) are functions of $T_{TC}(t)$. Equation 3.5 can be rewritten as the time derivative of the pan temperature, Eqn. 3.6, and equated to Eqn. 3.4. The relationship between T_w, T_g, and T_{TC} is determined from the pan temperature, Eqn. 3.5, and the integration of the wall temperature time derivative in Eqn. 3.7.

$$\frac{dT_p}{dt} = \left(\frac{1}{J}\right)\left(\frac{dI(t)}{dt} - K\frac{dT_w}{dt} - 4LT_w^3\frac{dT_w}{dt}\right) \tag{3.6}$$

$$\frac{J\left(DT_p + ET_w + FT_p^4 + GT_w^4 + H(t)\right) - \frac{dI(t)}{dt}}{(-K - 4LT_w^3)} = \frac{dT_w}{dt} \tag{3.7}$$

For the first few seconds, the calculated pan temperature is not realistic, Figure 3.24. After about 4 seconds, the profiles of the three temperatures maintain a parallel relationship. The initial instability is due to the fact that the heating rate of the thermocouple is set at a constant. At the early part of the model, the temperature difference between the wall and thermocouple temperature is not well established. Since the wall is the thermocouples heating source, the pan temperature is raised to an unrealistic value in order to satisfy the heating rate. In the true environment the heating rate is raised to the constant value. This does not affect the analysis sought here since the Curie point temperatures occur much later.

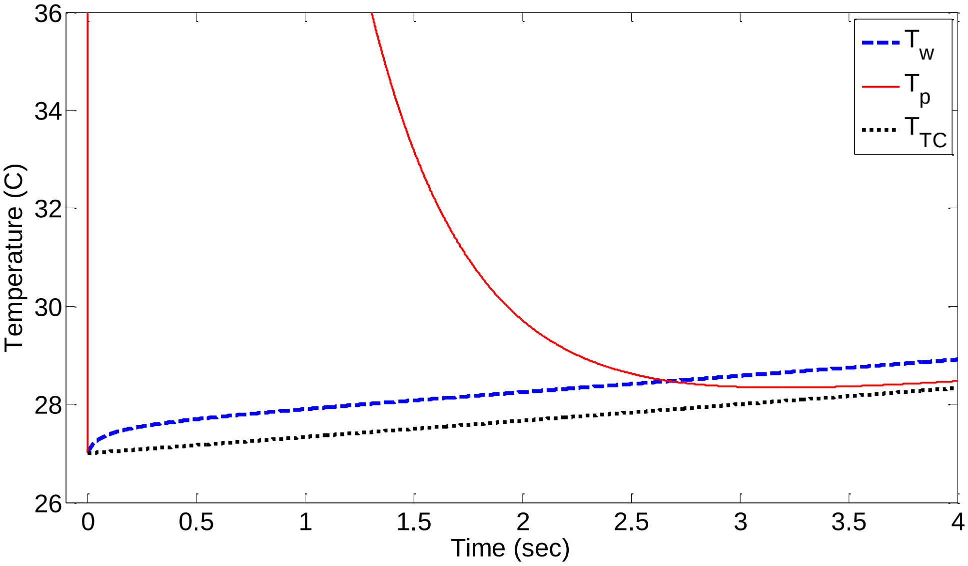

Figure 3.24. Initial instability of T_p.

The results of the thermocouple temperatures which correspond to the pan at the four curie point temperatures are shown in Table 3.1. In this setup the thermocouple temperature is higher than the pan temperature at low heating rates. As heating rate increases the temperature difference is decreased and at high heating rates the thermocouple temperature ends up lower than the pan temperature. These results establish that pan temperature can be higher than the thermocouple temperature at certain heating rates and lower at others. However, the measured thermocouple temperatures increased with heating rate and in this model are shown to decrease. This is due to the assumptions placed on this model. The mass of the thermocouple and pan were assumed to be the same.

Table 3.1. Thermocouple temperatures at sample Curie point temperatures (m_p=m_{tc}).

m_p=m_{tc}=135mg	Curie Point			
	Alumel T_p=152.6°C	Nickel T_p=358.2°C	Ni83Co17 T_p=554.4	Ni63Co37 T_p=746.4
10°C/min	152.692	358.249	554.432	746.423
20°C/min	152.615	358.226	554.422	746.417
50°C/min	152.385	358.154	554.390	746.400
100°C/min	151.998	358.035	554.337	746.372
250°C/min	150.830	357.678	554.179	746.288
500°C/min	148.839	357.078	553.912	746.145

This same model is repeated with a thermocouple 1/10th the mass of the pan, Table 3.2. In this setup the heating rate is proportional to the change of thermocouple temperature. This analysis establishes that the observed heating rates affect the Curie point calibration in a realistic way. The model observed that the thermocouple temperature can be either higher or lower than the pan temperature based on heating rate. The actual difference between the two temperatures is much larger in the true system, however this is due to simplifications made in the model, and the trends observed in the models is of more interest.

Table 3.2. Thermocouple temperatures at sample Curie point temperatures (m_p=10m_{tc}).

m_p=10m_{tc}=135mg	Curie Point			
	Alumel T_p=152.6°C	Nickel T_p=358.2°C	Ni83Co17 T_p=554.4	Ni63Co37 T_p=746.4
10°C/min	152.787	358.279	554.445	746.430
20°C/min	152.806	358.285	554.448	746.431
50°C/min	152.862	358.302	554.456	746.435
100°C/min	152.955	358.331	554.469	746.443
250°C/min	153.2337	358.417	554.507	746.462
500°C/min	153.817	358.642	554.633	746.550

3.4.2. Results

Similar to the previous TGA results, samples are loaded and purged in the nitrogen environment for 30 minutes to remove all oxygen that enters the system when the furnace is opened. Neat TPU, 5% Cloisite 30B, 7.5% MWNT, and 10% CNF samples were tested at 20^{o}C/min, 50^{o}C/min, 100^{o}C/min, 250^{o}C/min, and 500^{o}C/min. Films are pressed with a Carver hydraulic press to thickness 0.254mm (0.01"). Using thin films is a more consistent method than cutting samples of a certain mass from pellets as was used in the previous TGA experiment. Circular discs are punched from these thin films.

The two step reactions observed in the TGA experiments presented in section 3.3.2 are also observed here. The shape of the degradation described earlier as a "shift" is not observed. The two reaction steps are clearly present in the neat TPU tests in this TGA setup, Figure 3.25, whereas in the previous TGA setup the two steps are not distinguishable. The fact that the two peaks are distinguishable in these experiments is due to the fact that thin films are used rather than cut segments of pellets. The thinner sample size produces significantly more detailed data especially at the higher heating rates. At low heating rates the first reaction occurs at a higher rate than the second reaction. But at the highest heating rate, 500^{o}C/min, the peak heating rate is actually in the second reaction regime. Both peaks shift as the heating rate is increased.

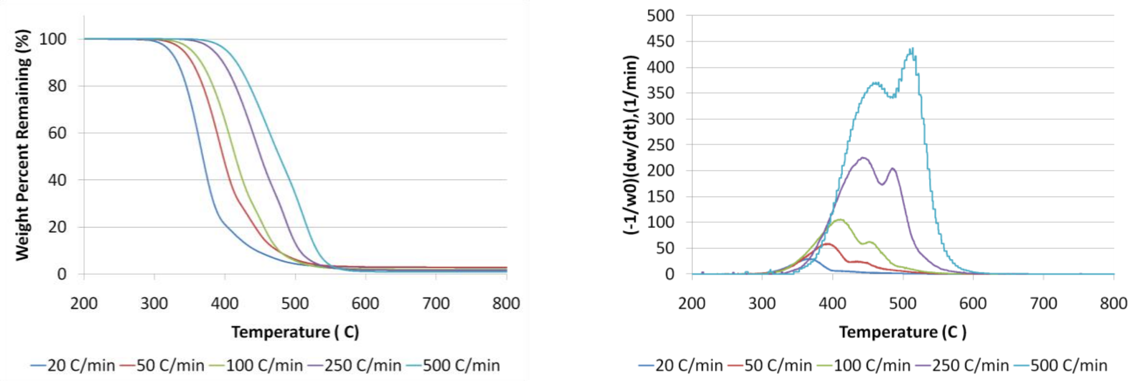

Figure 3.25. Neat TPU high heating rate TGA and DTGA.

The DTGA curves of the PNC samples are shown in Figure 3.26 to Figure 3.28. Note that the overlap in TGA curves with increasing heating rates which is observed in the previous TGA experimental study is not observed in any of the tests performed here. The two step reactions are also observable in each of the PNCs tested.

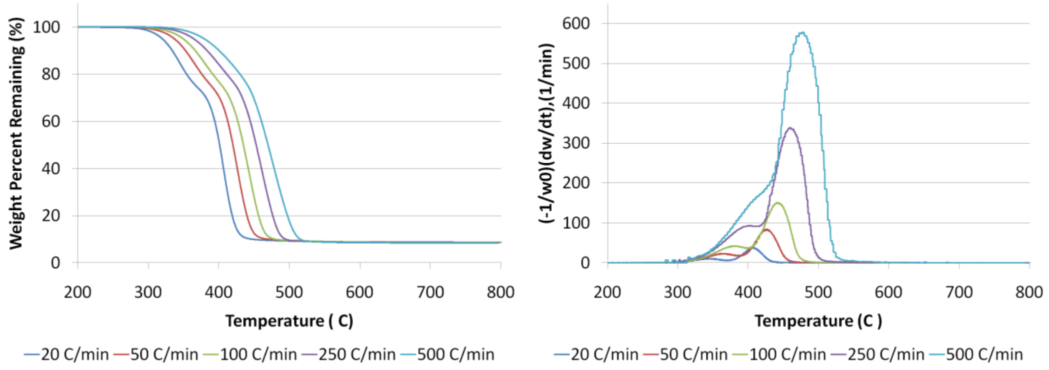

Figure 3.26. 7.5% MWNT PNC high heating rate TGA and DTGA.

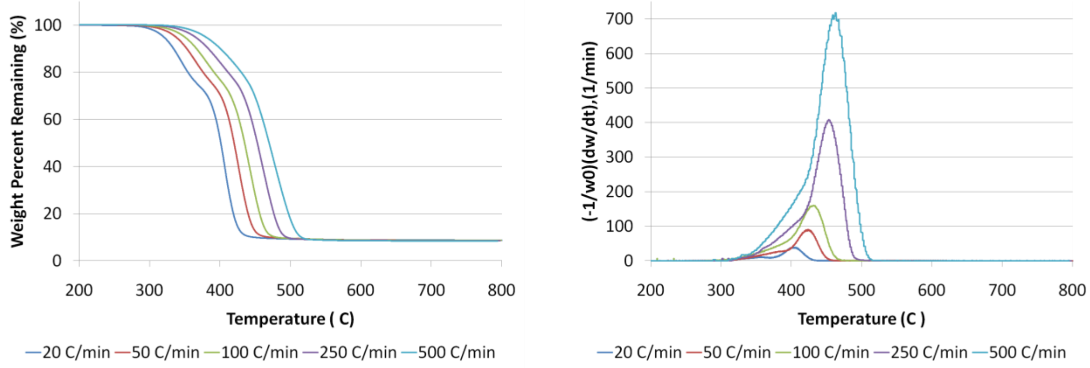

Figure 3.27. 10% CNF PNC high heating rate TGA and DTGA.

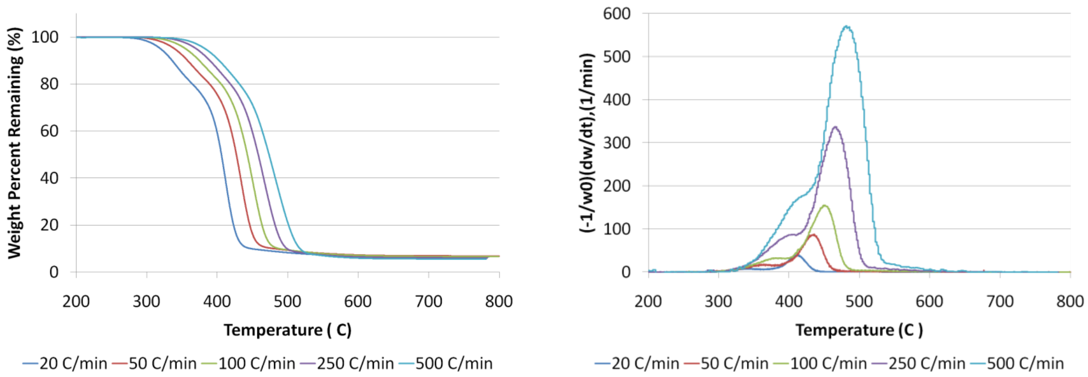

Figure 3.28. 5% Nanoclay high heating rate TGA and DTGA.

A comparison of the highest and lowest heating rates show that at low heating rates the TGA curves of the PNCs follow a very similar shape. In fact, the peaks of degradation rates are very similar. At the higher heating rate however, the MWNT and nanoclay PNC curves are dissimilar to the CNF curve which has a significantly higher DTGA peak. At the 500°C/min heating rate the peak rate of degradation in the CNF PNC also occurs at a lower temperature 458°C compared to the peak compared to the 472°C and 478°C of the MWNT and nanoclay PNC, respectively.

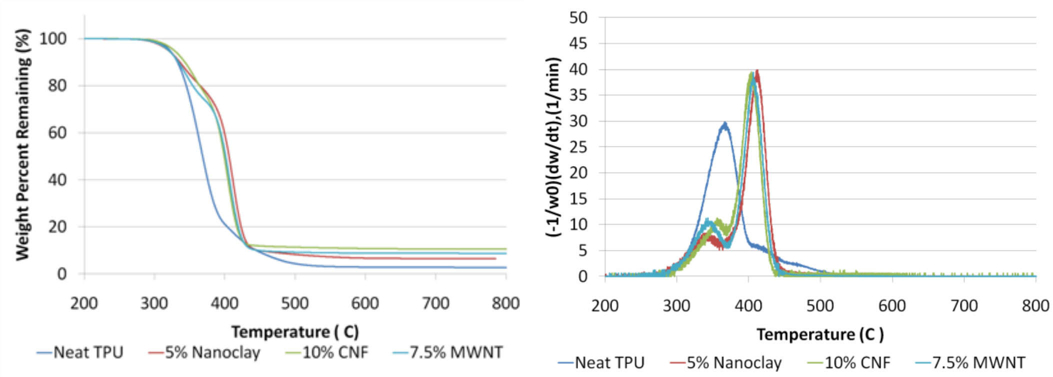

Figure 3.29. PNC TGA and DTGA @ 20°C/min.

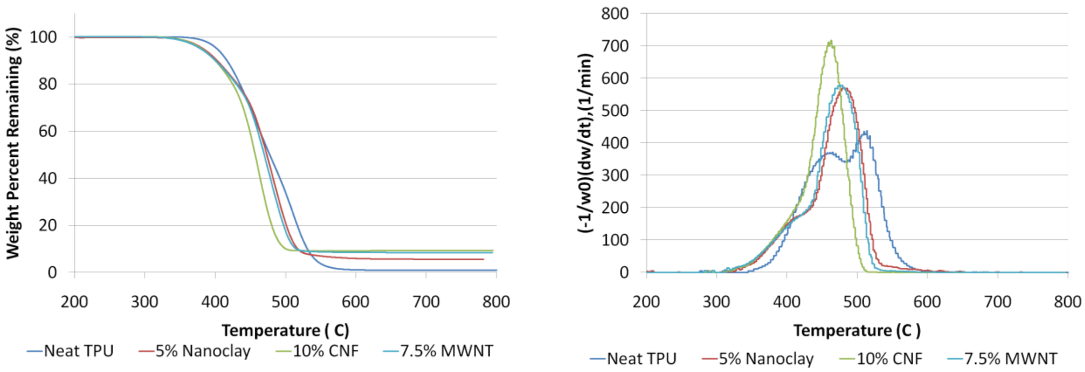

Figure 3.30. PNC TGA and DTGA @ 500°C/min.

The temperature at which 50% of the mass is lost as well as the onset temperature is shown in Table 3.3. The onset temperatures of the 20°C/min heating rates show that thermal stability is enhanced by the three nanomaterials. The nanoclay PNC material shows the greatest thermal stability with a 46°C onset temperature enhancement. Both the MWNT and CNF PNCs also enhance the thermal stability by 41°C and 39°C, respectively. Each PNC also loses 50% of its mass at least 30°C after the neat TPU does. However once the heating rate is increased to 500°C/min the level of enhancement significantly decreases in each of the PNC tests. Each of the PNCs in this case loses 50% of its initial mass before the neat TPU does. Both the MWNT and nanoclay PNCs are within 10°C of the neat TPU. However, 21°C before the neat TPU loses 50% of its original mass the CNF PNC does. Comparison of the onset temperature at this heating rate shows that the nanoclay material only slightly has an enhancement of thermal stability. The MWNT sample is shown to have only a slightly lower thermal stability, whereas the CNF sample's thermal stability is 14°C less than the neat onset temperature.

This set of data shows the importance of high heating rate experimental capabilities. The PNCs are shown to thermally enhance the TPU at low heating rates but poorly performs at higher heating rates, Table 3.3.

Table 3.3. Onset and 50% remaining weight in high heating rate TGA.

	50% Remaining Weight		Onset Temperature	
	20°C/min	500°C/min	20°C/min	500°C/min
Neat TPU	369°C	478°C	335°C	425°C
5% Nanoclay	401°C	470°C	381°C	428°C
7.5% MWNT	406°C	474°C	376°C	422°C
10% CNF	399°C	457°C	374°C	411°C

3.5. SIMULTANEOUS TGA/DSC

An additional TGA test is performed using a TGA/DSC 1 TGA from Mettler Toledo. The reason this setup was chosen is to obtain specific heat measurements based on the DSC portion. Traditional Differential Scanning Calorimeter (DSC) measurements use a two cell approach. In one cell a reference material with a known specific heat is heated in the same furnace as another material. Based on the difference in thermal response of the sample material compared to the reference material the heat flow to or from the sample can be calculated. These experiments are usually performed in a closed environment. In this way degraded material has the chance to condense during cooling which often is also where measurements are taken from.

In these experiments however the sample pan is an open one. A reference material is used to calibrate the instrument separate from the actual run. This setup is different than the previous two in that it is not a hang down TGA. Instead an alumina sample pan is placed on top of a scale which is held like a cantilever beam. The furnace also opens horizontally and exposes a much smaller opening for the robotic arm to load the sample.

Samples in this case are held isothermally at 50°C. The samples tested are cycled from 50°C to 200°C in order to remove any processing thermal histories.

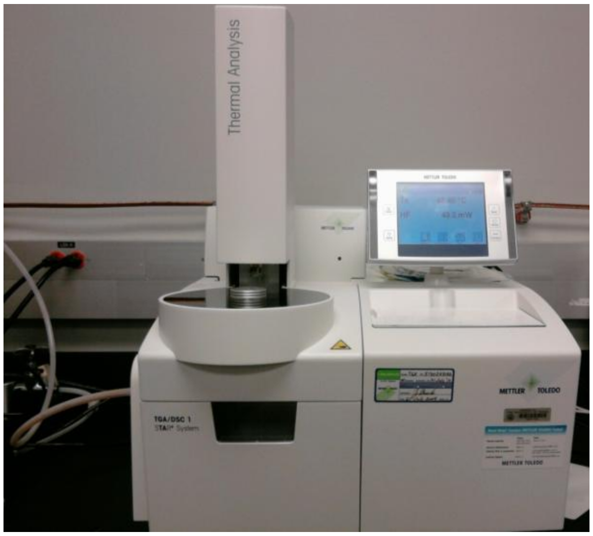

Figure 3.31. TGA/DSC 1 Mettler Toledo.

3.5.1. Calibration

This instrument is calibrated by the melting point of reference materials. In traditional hang down wire TGA instruments, melting points can also be used as reference materials. This is often done by holding a reference material above the sample pan such that when the material does melt it drips onto the sample pan thus signified in an increase in small mass.

However, since this TGA instrument is also a DSC instrument, the heat flow due to melting can also be detected. Since this instrument is part of a public facility calibrations were performed by the instrument’s administrator. A check is done however using simple aluminum foil. Initial results drew concerns because the calculated specific heat from the DSC results for the neat TPU was much larger than expected based on literature values of the virgin material. Upon further investigation this was also found to be the case for results of aluminum foil and nylon 11. This as it turns out was a software problem with the baseline subtraction.

The experiment asks for a baseline run to be made. A blank pan is heated at specified heating conditions and the mass loss changes as well as the heat flow are measured. The computer subtracts these measurements from the measurements made afterwards under the same thermal history method. Although changes to the TGA results are small due to the fact that the baseline sample mass changes are minimal, the DSC heat flow subtraction does not occur correctly when the software is asked to automatically perform this. Instead it is found that collection of the blank and raw sample data is important. Post test analysis is possible to subtract and obtain reasonable DSC results. When performed the specific heat of the TPU, aluminum foil, and nylon 11 samples were within the ±3% of literature values. It is unclear at this point why the software is causing these errors. Figure 3.32 shows an example of the different heat flow measurements that are taken from the aluminum foil specimen. These experiments are performed at a heating rate of 20^{o}C/min and cooled at 10^{o}C/min from 50^{o}C to 800^{o}C. An empty sample is first run to collect the baseline data. This data is labeled "blank run". Next an aluminum foil specimen is placed in the sample pan and heated in the same thermal history; this data is labeled "Al Foil_ComputerSubtracted". In this data set the "blank run" is subtracted from the data by the software. The aluminum foil was then rerun; however this run specifically requested the raw data. This data is labeled "Al Foil_W/outSubtraction". The "blank run" data is subtracted afterwards and this data set is labeled "Al Foil_PostTestSubtraction". There is about a 23 mW difference between the "Al Foil_ComputerSubtracted" and "Al Foil_PostTestSubtraction" data sets. These two data sets should be identical. For this reason tests are subtracted from the blanks manually, not with the software.

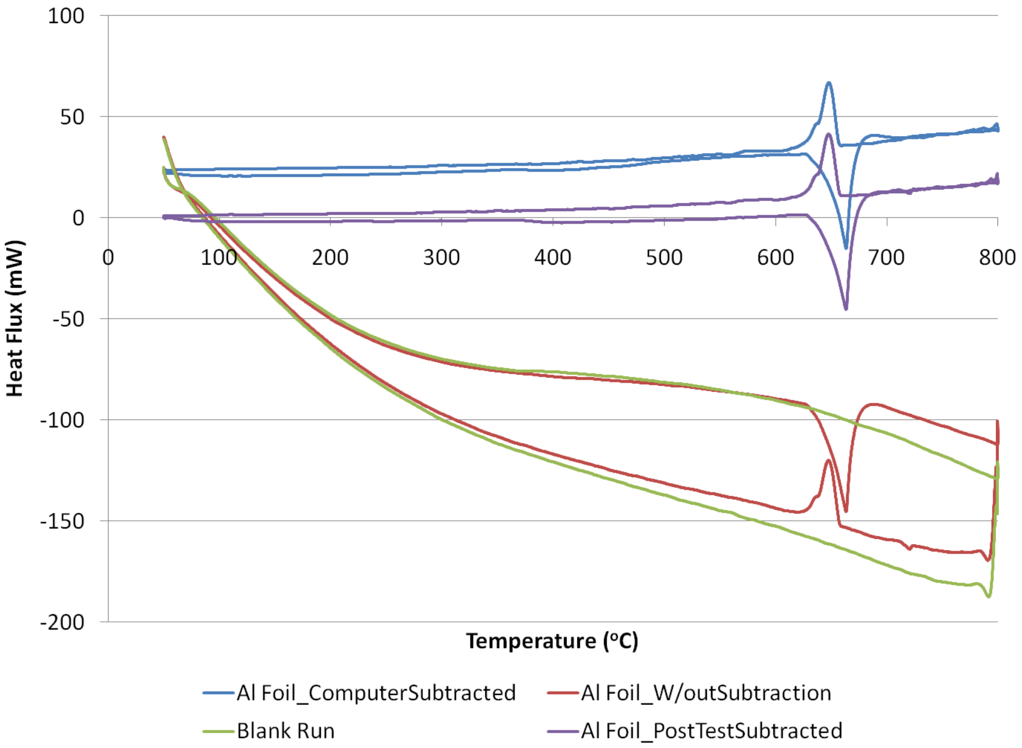

Figure 3.32. Aluminum foil blank subtraction comparison.

The calibration discussion describes the reason that the DSC data appeared to be incorrect is based on the specific heat calculation compared to literature data, equation 3.8. This equation is valid to determine the specific heat before the material begins to degrade. In the case of thermal degradation an additional energy term must be taken in account. More work is necessary to analyze the accuracy of the specific heat values obtained from this experiment.

$$\dot{Q} = mc_p \frac{dT}{dt} \tag{3.8}$$

3.6. KINETICS

To evaluate kinetic chemical decomposition parameters an isoconversion method is used (Ceamano, Mastral, Millera, and Aldea, 2002). Kinetic parameters describe the degradation behavior of different materials. Many different kinetic models are used to curve fit TGA data (Bruns, Koo, and Ezekoye, 2009). A materials solid conversion, X_s, described in eqn. 3.9 is used to describe the degradation process with eqn. 3.10. The kinetic constant, k, in this equation is represented by the Arrhenius equation, eqn. 3.11. Using the Ozawa Flynn Wall method, eqn. 3.12 (Day and Budgell, 1992), the activation energy, E, and pre-exponential, A, can be determined.

$$X_s = \left(\frac{w_o - w}{w_o - w_f}\right) \tag{3.9}$$

$$\frac{dX_s}{dt} = k(1 - X_s)^n \tag{3.10}$$

$$k = Aexp\left(-\frac{E}{RT}\right)^n \tag{3.11}$$

$$\ln\beta = \ln\left(\frac{AE}{R}\right) - 5.33 - \ln(1 - X_s) - 1.05\frac{E}{RT} \tag{3.12}$$

By fitting the $\ln\beta$ and $\frac{1}{T}$ terms at a specific solid conversion at different β, heating rates, the activation energy and pre-exponential can be determined using linear curve fits. Therefore, for each solid conversion factor a distinct activation energy and pre-exponential can be obtained. Kinetic parameter analysis performed by Lee et. al (2009) show that the kinetic parameters calculated by this method for low heating rate vs. high heating rate TGA conditions produce different kinetic parameters. However, considering how that the higher heating rate TGA experiments produced more uncertainty in the thermal data these high heating rate experiments were adequately predicted by the lower heating rate experiments. More work is necessary in order to fully understand how the data can be extrapolated to even higher heating rates.

3.7. CONCLUSION

Three sets of TGA experiments are presented in this chapter. At low heating rates, the PNCs significantly enhance the TPU's thermal stability. The calibration and cleaning necessary for each of the three equipments is shown to drastically influence the type of data that is obtained. At high heating rates, the calibration method itself is difficult to obtain consistent results so the data from these experiments have higher uncertainties.

The enhancements observed at the lower heating rates are not observed at the higher heating rates. The enhancement characteristics are quantified by the temperature at which 50% of the original mass is degraded and the onset temperature. In fact, at the highest heating rate tested, 500°C/min, the degradation data of the CNF PNC behaved significantly worse than the neat TPU. Both the nanoclay and MWNT performed very similarly in all the tests. However, at this highest heating rate the neat TPU shows better thermal stability.

At the low heating rates, each of the nanomaterials similarly enhances thermal stability. The proposed mechanism that these nanomaterials act as hard segments can be observed since the first reaction is slowed down. Even in the higher heating rates the thermal stability of the first reaction is enhanced significantly compared to the neat TPU.

The loss in overall thermal stability enhancement has more to do with the fact that the thermal properties of the PNCs change with nanomaterial loading. Although the nanomaterials act as hard segments at these high heating rates a thermal gradient may be present. The increase in thermal conductivity especially in the CNF PNC results in an overall higher sample temperature leading to a larger loss in mass. This is still an accurate comparison of the samples since the materials are exposed to identical heat environments.

It is important to remember that these tests are solely degradation tests. In an ablation environment, the strength of a material during degradation is just as important as the materials ability to resist degradation, thermal stability. These TGA experiments can help explain the surface degradation processes. As the heating rate increases the degradation TGA curve will increase in temperature. In the next chapter, experiments in an oxidized environment are tested. One of these experiments also gives insight to the composition strength of the material during degradation.

Chapter 4. Flammability Analysis

4.1. INTRODUCTION

Flammability experiments are an important addition to the ablation process. Ablation processes experience oxidation in addition to the pyrolysis process studied in the previous chapter. Two flammability tests are presented. In one test, a sample is burned vertically in which the strength of the material is tested if the sample can hold its own weight during degradation. The second flammability test is conducted horizontally. The samples' mass loss as well as oxygen consumption is useful to understand how an ablative material will burn and continue to burn as it consumes available oxygen.

4.2. UL94 VERTICAL

A standard flammability test performed on polymers is the UL 94 test. Of the three types of UL 94 test setups: surface burn, vertical burn, and horizontal burn tests; the vertical burn test was performed on the Desmopan® nanocomposite formulations. A 2.54 cm (1") flame is placed at 45° to the bottom of a clamped 12.7 cm x 12.7 mm x 3.175 mm (5" x 0.5" x 0.125") test specimen, Figure 4.1. After 10 seconds the flame is removed and the time the specimen remains on fire is recorded. A second 10 second flame is introduced and the time of burn after removal is again recorded. The specimen is held 30.48 cm (12") above a piece of cotton. The cotton is used to determine the flammability of any drip from the material. Based on these observations the specimen can either pass or fail V0, V1 or V2.

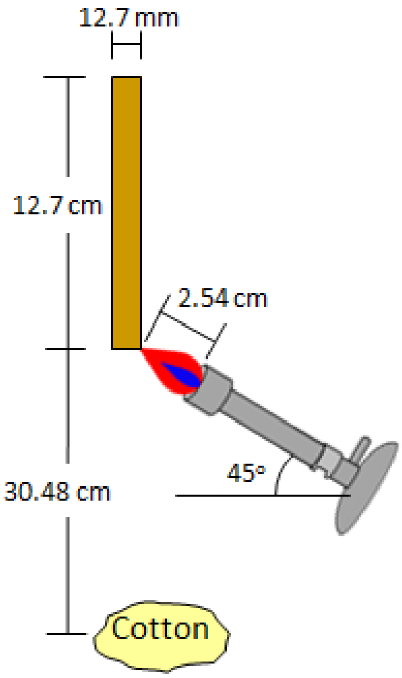

Figure 4.1. Vertical UL 94 burn test setup.

V0 is the most stringent of the three. The specimen must not burn for more than 10 seconds and is not allowed to drip and ignite the cotton. V1 allows up to a 30 second burn but still restricts drip that ignites the cotton. V2 also allows less than 30 second burn time however allows drip that ignites the cotton.

A set of five specimens is tested above the cotton piece. After conducting the experiments, it is found that many of the materials do drip or fall apart. As the material falls onto the cotton below each one ignites the cotton. The material continues to burn with the cotton and the remnants are difficult to characterize. To better understand and predict the drip, an additional seven tests of each material formulation are performed. In these tests the cotton piece below is removed. Note that all descriptions of events at a certain time are in reference to when the flame is first introduced.

The neat TPU does drip, so it passes V2. The material before and after the UL 94 tests are shown in Figure 4.2. After a flame is introduced to the specimen for 10 seconds, none of the bulk material burned. However, 4 of the 7 specimens did drip. The drip is very liquid like, this can be observed in the fourth burnt test sample shown in Figure 4.2b. When the flame is introduced for an additional 10 seconds, all 7 test specimens dripped. The bulk material of each of the 7 samples burned for less than 1 second.

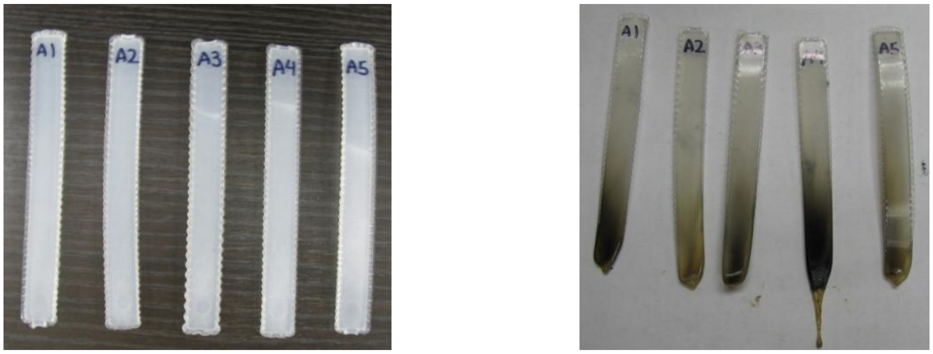

(a) (b)

Figure 4.2. Neat Desmopan® (a) before and (b) after vertical UL 94 test.

To understand how the material self extinguishes, a neat TPU specimen is clamped in the same setup as the vertical burn UL 94 setup. Instead of removing the flame after 10 seconds, the flame is held for an extended period of time. A stream of melted material dripped. This drip was on fire, shown in Figure 4.3. The bulk material however burned in the same way that the pervious tests had shown. The presence of the flame is sufficient to melt the TPU and the conditions of the melt are sufficient for it to burn. Since the presence of a flame for an extended period of time does not cause the bulk material to burn for any longer, this means a significant amount of the heat is transferred into melting the material. As the burning material drips additional heat is removed from the bulk material.

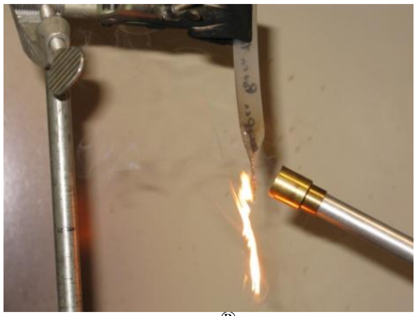

Figure 4.3. Neat Desmopan® extended burn time.

The viscosity of the material plays a large role. A much stiffer TPU elastomer, Pellethane™, was also tested. The most significant difference between the two TPU's is that Pellethane™ is a much stiffer material, with a shore hardness of 94A as compared to the shore hardness of Desmopan®, 65A. The neat Pellethane™ burns for a short time and begins dripping. A much larger portion of the Pellethane™ dripped due to the longer burn time; the Pellethane™ specimens after the test are shown in Figure 4.4. The increased hardness of this TPU is reflected in a more viscous melt which result in the bulk material to burn. Most of the burn times are less than 10 seconds, Table 4.1, however two of the specimens (3 and 4) burned for over 30 seconds when the second flame was removed. The viscosity and sensitivity of this experiment are crucial. The Desmopan® melt flows fast enough that this sensitivity is not observed and the bulk material simply does not burn as the extended burn test had shown. In relation to an actual ablation application, if the neat Desmopan TPU is placed as an ablator the material will melt and be sheared free into the flow stream down the rocket combustion chamber.

Table 4.1. Neat Pellethane™ burn times after 1st and 2nd flame.

	Burn Time (sec) After 1st Flame Removed	Burn Time (sec) After 2nd Flame Removed
Specimen 1	3	6
Specimen 2	2	1
Specimen 3	4	44
Specimen 4	6	57
Specimen 5	3	3

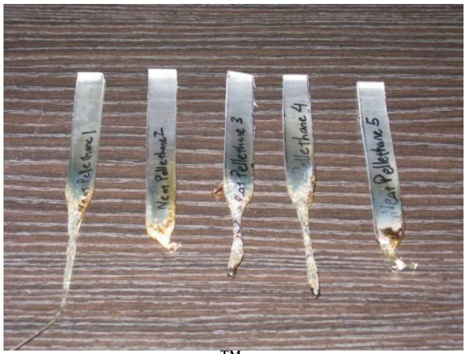

Figure 4.4. Neat Pellethane™ specimens after UL94 test.

The next test involves TPU with 2.5 wt% nanoclay formulation. This formulation behaves significantly differently than the neat TPU under UL 94 testing. The bulk specimen begins to burn after the flame is removed. None of the surfaces begin to melt as they do in the neat TPU sample. As the specimen burned, it became structurally weak and began to fall apart. Each of the 7 specimens tested, had between 4 and 8 distinct pieces fall during the test. The first piece that falls occurs at an average of 39 seconds after the flame is introduced, and the last drop occurs at an average of 85 seconds after the flame is introduced. The first piece that falls ranges between 12.7 cm and 38.1 cm (0.5" and 1.5") long. Subsequent samples that fall are smaller in size. After the first segment drops the material loses its structure resulting in the small segments. After the last piece drops, about a 0.635 cm (1/4") of material remains held in the clamp. This specimen continues to burn for an average of 185 seconds. After that time a second 10 second flame is introduced, but the specimen does not burn or drip. This signifies that all combustible material was burned during the first 10 second of flame exposure.

The nanoclay prevents the specimen from dripping like the neat material. It provides a thermal boundary, increases the melt viscosity, and creates a surface char. The surface char is held together as the center of the material melts. This is clear because during the experiment charred segments begin to elongate from the bulk material. These segments have a char surface and a melt like center. The charred surface breaks away from the bulk material and is held only by the viscous melt center. After the first drop, subsequent drops do not have a consistent shape or size because of the melt elongation.

A higher loading of nanoclay, 5 wt%, decreases the number of drops to just one. This drop occurs on average at 76 seconds, about twice as long as in the 2.5 wt% nanoclay specimens. The specimens that drop are also much longer, between 10.2 cm and 11.7 cm (4" and 4.625"). The specimens have a total burn time of 177 seconds, slightly shorter than the burn time of the 2.5 wt% nanoclay samples. In both the 2.5 wt% and 5 wt% nanoclay PNC formulations, cracks appear in the specimen while it burns. These cracks are associated with thermal stress and out-gassing of the polymer. The locations that these cracks appear are not predictable, however depending on the specimen formulation, a crack occurring at a specific location may or may not lead to a piece falling. Pieces of the 2.5 wt% specimen fall almost immediately with each crack. In the 5 wt% nanoclay specimen, the first segment that dropped was as large as 10.5 cm (4.125"). This signifies that there is an increase in mechanical strength of the charred specimen with increased nanoclay loading.

This trend of increasing mechanical strength of the char is also observed in the higher nanoclay loadings since none of the 7.5 or 10 wt% nanoclay specimens fall.

During the burning of 7.5 wt% and 10 wt% nanoclay, cracks are not observed. The 10 wt% samples after UL94 testing are shown in Figure 4.5. The burn time of these specimens are longer than the nanoclay formulations that did drop. The 7.5 wt% and 10 wt% nanoclay specimens burned for an average of 228 and 237 seconds, respectively. After the specimen burned it was weighed, the original mass of the 7.5 wt% and 10 wt% nanoclay specimens was 6.1 to 6.2g and after completely burned was 0.9 to 1.1g, about 5/6 of the sample in weight had burned off.

Figure 4.5. Desmopan-10 wt% Cloisite® 30B after vertical UL 94 test.

The range of drop times as well as the burn times of each formulation of the nanoclay family is shown in Table 4.2. As more nanoclay is added, the number of drops decreases. In addition, since the strength of the charred material is increased a longer specimen is required to induce a drop leading to a longer time before the first drop occurs. Since each of the nanoclay formulations did not burn on the second introduction of the 10 second flame, all combustible material is assumed to have been consumed. Specimens which had sections that dropped have shorter burn times than that of specimens that did not drop. This is due to the fact that dropped segments have not completely burned while attached to the bulk material.

Table 4.2. Nanoclay drop and burn times.

	# of Drops	1st Drop Time (sec)	1st Drop Length (cm)	Last Drop Time (sec)	Burn Time (sec)
2.5 wt% Nanoclay	4 to 8	39	1.3 – 3.8	85	185
5 wt% Nanoclay	1	76	10.2 – 11.7	---	177
7.5 wt% Nanoclay	0	---	---	---	228
10 wt% Nanoclay	0	---	---	---	237

Scanning electron microscopy (SEM) images of the surface of Desmopan-10% Cloisite 30B at different stages of a UL94 experiment are shown in Figure 4.6. The heated surface, Figure 4.6a, is a surface that has not burned however is near a flame so has been thermally heated. The heat from the flame causes the material to begin to crack. A surface that begins to burn for 30 seconds and is externally extinguished is shown in Figure 4.6b. Large degassing bubbles are observed. As the material continues to burn until no combustible material remains, more bubbles appear, Figure 4.6c.

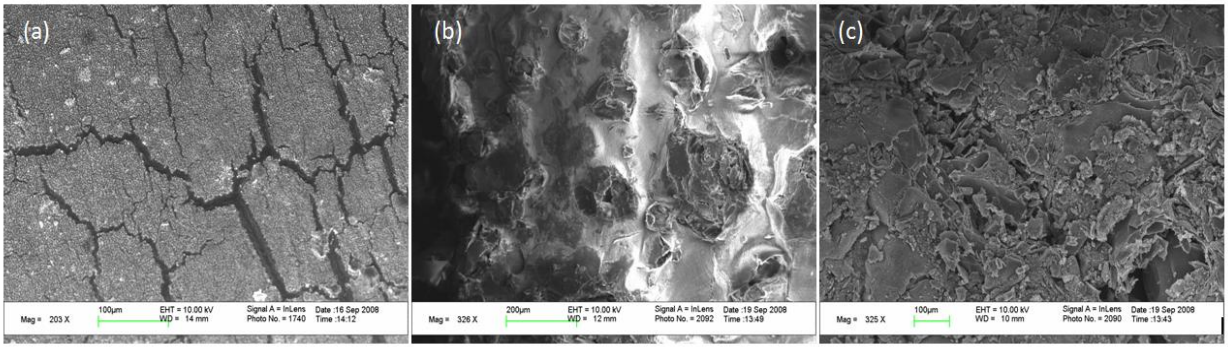

Figure 4.6. SEM images of Desmopan-10% Cloisite 30B at three burn stages: (a) heated surface (b) 30 second burn surface and (c) complete burn surface.

The 2.5 wt% MWNT samples took on average 33 seconds before the first piece dropped, about the same time the 2.5 wt% nanoclay samples dropped, 39 seconds. This drop however is of much smaller samples, approximately 0.1 g. The difference may be due to the type of char formation each PNC creates. The MWNT specimen cracks everywhere and continuously drops small pieces until about 119 seconds after the flame is first introduced. A small section remains clamped and continues to burn. The burn time for the 2.5 wt% formulation is 175 seconds.

The 5 wt% MWNT specimens holds together better. Initially the specimen elongates without visible cracking. After about 30 seconds, cracks appear and cause the specimen to fall at 63 seconds. This is twice the time it takes for the 2.5 wt% MWNT specimens to begin falling. The first specimen that falls is between 5 cm and 6.7 cm (2" and 2.625") long. The burnt specimens are extremely brittle. Increasing the loading to 7.5 wt% and 10 wt% MWNT decreased the number of drops to no more than 1. In fact 2 of the 7.5 wt% MWNT specimens and 5 of the 10 wt% MWNT specimens did not have pieces drop. Of the specimens that did drop, the drop occurred at 106 and 109 seconds for the 7.5 wt% and 10 wt% MWNT formulations, respectively. As shown in Table 4.3, the length of the first drop specimen increases with MWNT loading up to 7.5 wt%. The length of the dropped specimen at 10 wt% MWNT does not follow this trend. This is due to the unpredictable location of the cracks. In each of the MWNT formulations, cracks occur everywhere, the amount of cracking is significantly more than that observed in even the 2.5 wt% nanoclay samples. In the 10 wt% MWNT samples which dropped, cracks occurred at both sides of the specimen and met at the center. If the cracks were offset vertically, a drop would not have occurred.

Figure 4.7. Low weight loading of MWNT showing cracks along edges.

Table 4.3. MWNT drop and burn times.

	# of Drops	1st Drop Time (sec)	Length 1st Drop (cm)	Last Drop Time (sec)	Burn Time (sec)
2.5 wt% MWNT	Continuous	33	~0.1 grams	119	175
5 wt% MWNT	2 to 4	63	5.1-6.7	85	171
7.5 wt% MWNT	0 to 1	106	8.9-11.1	---	200
10 wt% MWNT	0 to 1	109	7.3 – 9.8	---	230

SEM images, Figure 4.8, show that the burnt samples cracks are observable after testing as well. The cracked regions show a very different structure than that of the bubble formations observed in the post test nanoclay samples. In addition, higher resolution SEM images were taken with the aid of Dr. Jin Gyu Park and Dr. Richard Liang from Florida State University. SEM images of the virgin material show the embedded MWNTs in the TPU, and the burnt samples show that the remaining char material is only the MWNTs, Figure 4.9.

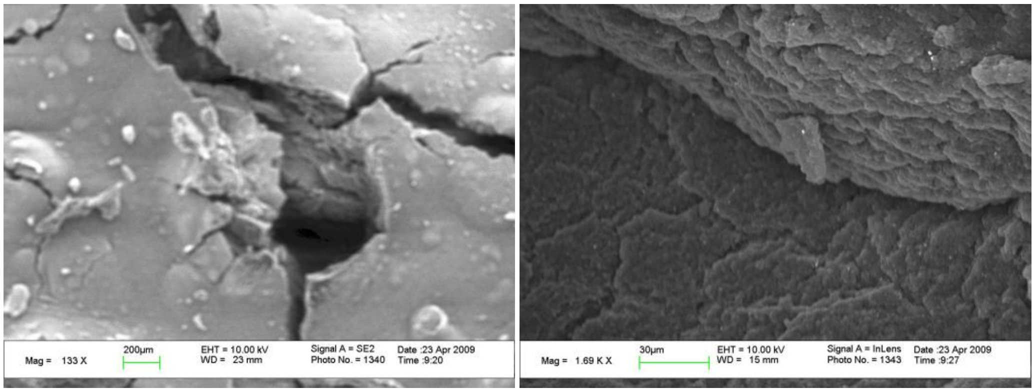

Figure 4.8. SEM images of burnt MWNT samples.

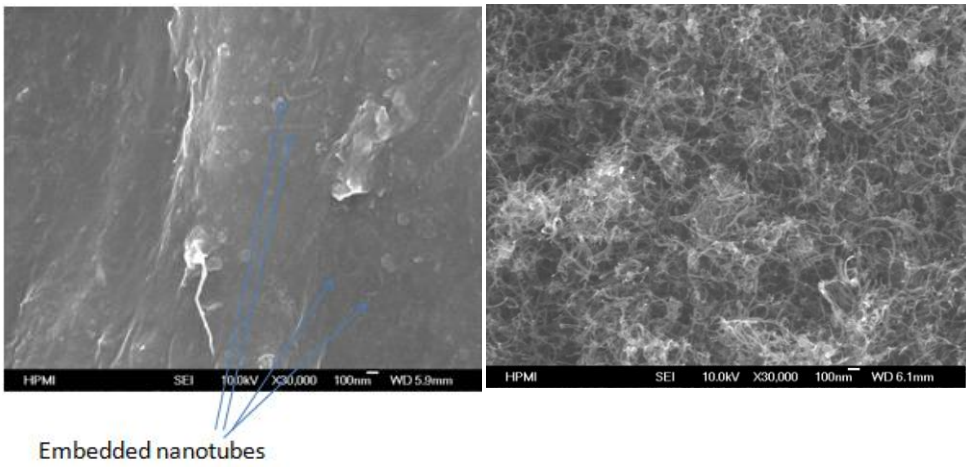

Figure 4.9. High resolution SEM images of virgin and burnt 10% MWNT samples.

The virgin CNF samples look identical to virgin MWNT samples, however burn very differently. Bubbling on the surface is observed, whereas the change in topography of the MWNT and nanoclay formulation surfaces is less dramatic. The 5 wt% CNF sample elongates quite a bit even at the surface which is not observed in both the nanoclay and MWNT PNCs. The elongating portion drips like a viscous liquid. Small solid pieces not fully melted, flow through the elongating portion and speed up the drip process.

The bulk material is only on fire in the area which is elongated, 12.7 cm (½”). As the flame propagates up into the section that has not deformed, that section then begins to elongate. Once the material begins to drip, flame propagation is slowed. The first drip occurs at 20 seconds, faster than any of the other nanomodified formulations. The sample continues to drip until it has all dripped at 152 seconds.

Increasing the loading to 10 wt% makes the drop have more surface structure. However once these specimens fall and hit the table, the shape deforms. These drop sections are not brittle, but very soft and deformable. After these specimens which have fallen and cooled, they become brittle as do the char of the other TPUNs. The flame propagates faster in this formulation because the added CNFs slow dripping. However the propagation of the flame is still much less than that observed in the MWNT and nanoclay tests. The 10 wt% CNF samples drip from 34 to 117 seconds, when all material has dripped.

The pieces of 15 wt% and 20 wt% CNF specimens that drop can be distinguished however each does deform due to its liquid like properties. As Table 4.4 shows, increasing the loading lengthens the time before the 1st drop occurs as well as shortens the time in which the last drop occurs. This however does not mean that the speed of drip increases with increased loading. As loading increases, the number of drops decreases, as does the time between drops. The flame propagation is a factor of the amount of flammable portion held with the specimen. The longer 1st drop time, allows the flame to propagate through a larger volume of the bulk material. SEM images show that after firing the CNF samples have many porous regions. And similar to the MWNT SEM images all that is left are CNFs, Figure 4.10.

Table 4.4. CNF drop and burn times.

	# of Drops	1st Drop Time (sec)	Last Drop Time (sec)	Burn Time (sec)
5 wt% CNF	Continuous	20	152	152
10 wt% CNF	Continuous	34	117	117
15 wt% CNF	8	39	109	109
20 wt% CNF	1-2	63	82	161

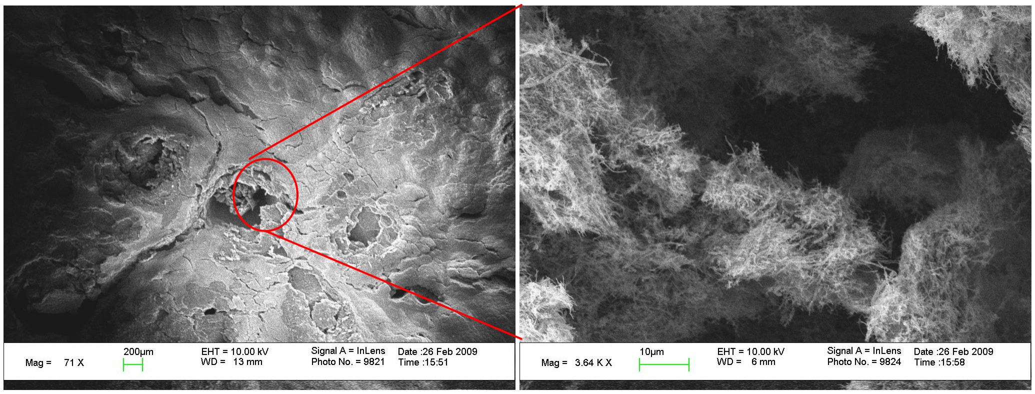

Figure 4.10. SEM image of 20% CNF after UL 94 firing.

4.3. CONE CALORIMETER

Cone calorimeter experiments for the neat and the 5% formulations of MWNT, clay, and CNF are performed at Pittsburg State University by Dustin Hart. Samples that were tested were 10.16 cm x 10.16 cm x 3.175 mm (4” x 4” x 0.125”) at 50 kW/m^2. Tests are performed on the neat TPU, 5% MWNT, 5% nanoclay, and 5% CNF PNC formulations.

4.3.1. Results

The tests were performed on two samples of the neat TPU. Unfortunately in each case the material melted and dripped off of the sample holder, Figure 4.11.

Figure 4.11. Dripped melted neat TPU cone calorimetry tests.

The aluminum foil melted during the test, Figure 4.12. Since the neat material is held in the aluminum foil, the neat material begins to drip through the melted foil. New test procedures can be implemented which involve an additional sample tray to catch material that is melted and fallen off which is recommended for future testing of neat TPU materials. The way that the material drips off of the foil is not repeatable resulting in two different heat release rate (HRR) measurements, Figure 4.13. At the end of the first test more aluminum foil had melted than TPU mass remained which resulted in a negative sample mass measurement, Figure 4.14. Sample 2 loses mass at a higher rate than sample 1 from the beginning. After 120 seconds from the start of the test, sample 2 has lost 30% more mass than sample 1. The post test sample, Figure 4.12, shows that in both segments large portions of foil have melted.

Figure 4.12. Post neat Desmopan® 6065A cone calorimeter samples.

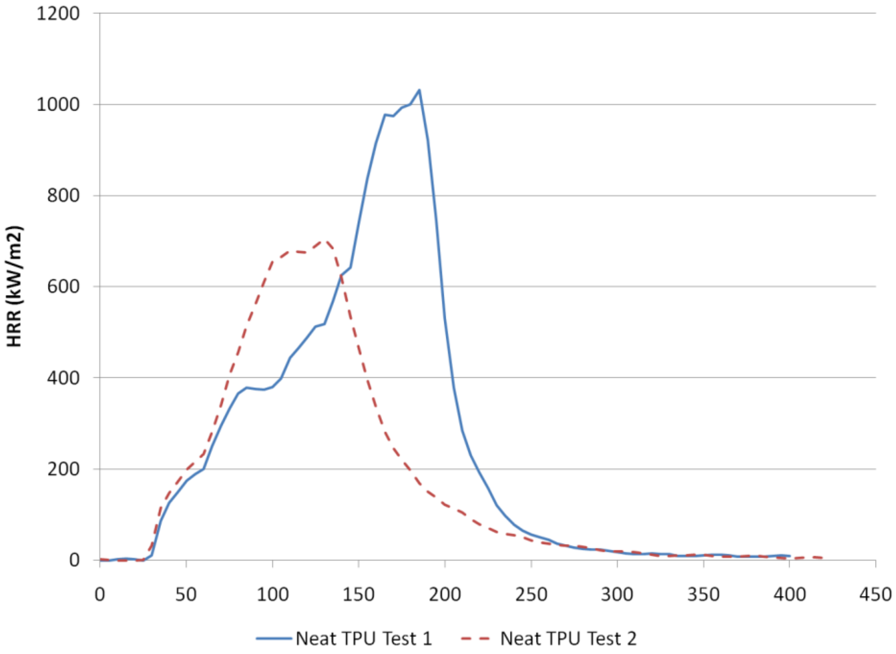

Figure 4.13. HRR of neat TPU - cone calorimeter, 50 kW/m^2.

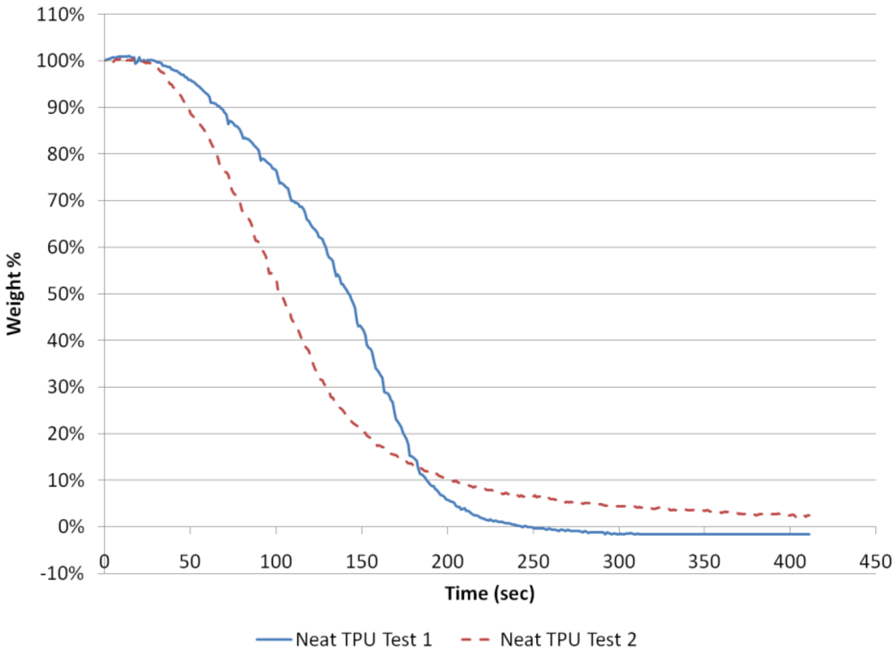

Figure 4.14. Mass loss of neat TPU - cone calorimeter, 50 kW/m^2.

The HRR and mass loss data of the PNC samples are much more repeatable as the foil does not melt. Three PNC samples are tested for each nanomaterial. The average mass loss values of the PNCs are compared to both of the neat TPU samples in Figure 4.15. Considering that the aluminum foil melted and released some of the melt during testing it is difficult to compare the mass loss rates of the neat TPU with the PNCs. However since each material is exposed to the same heat flux the heat released by each is the same. This is determined by the area under the HRR curve. The energy absorbed by each material is 101 MJ/m^2, 74 MJ/m^2, 102 MJ/m^2, 104 MJ/m^2, and 100 MJ/m^2 for the 1st neat TPU, 2nd neat TPU, 5 wt% nanoclay, 5 wt% CNF, and 5 wt% MWNT PNCs respectively. This shows that the second neat TPU test absorbed and released energy consistent to what is observed in the repeatable PNC cases. Comparisons for the rest of the chapter use the first TPU as the baseline. In the initial 125 seconds the neat TPU has more remaining mass than the PNCs. The time which 50 wt% of the TPU portion of the PNCs has degraded is 175 sec., 150 sec., and 116 sec., for the 5 wt% nanoclay, 5 wt%

MWNT, and 5 wt% CNF PNCs, respectively, compared to 142 sec when the neat TPU loses 50%. At this level of degradation the CNF sample continues to degrade faster than the neat TPU.

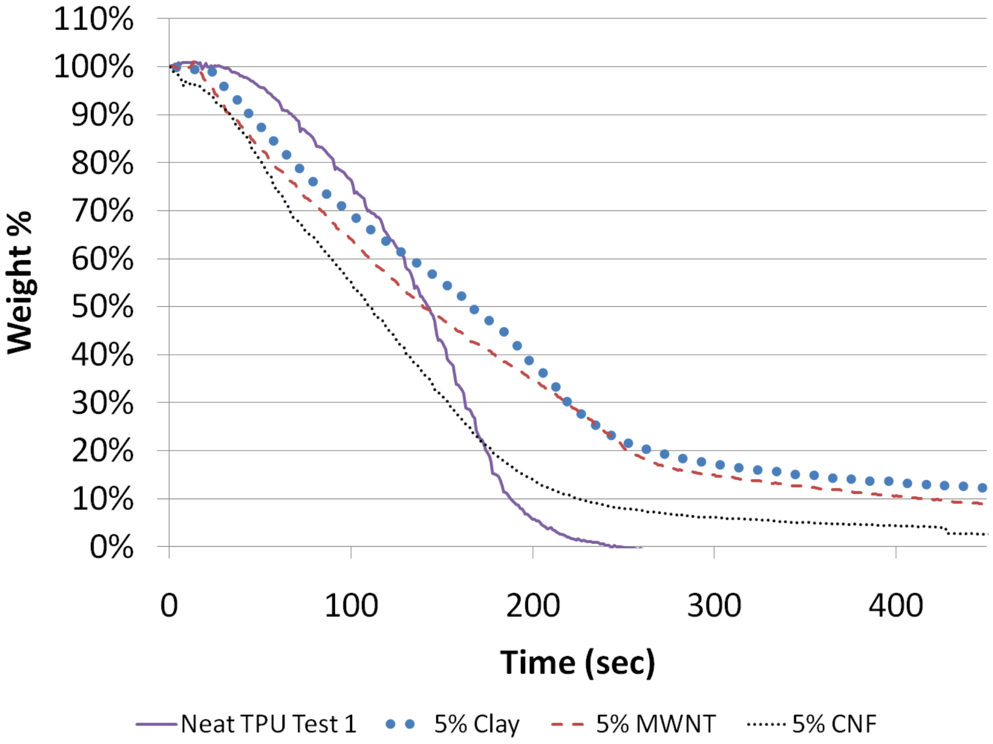

Figure 4.15. Mass loss of neat and 5% PNC – cone calorimeter, 50 kW/m^2.

Figure 4.16 shows that the neat TPU PHRR is higher than each of the PNCs. Similarly to the data obtained in the TGA experiments, the HRR curves show two local PHRRs in the PNC tests. The neat TPU appears to have only one peak HRR, which occurs after the first PNC PHRR and before the second PNC PHRR.

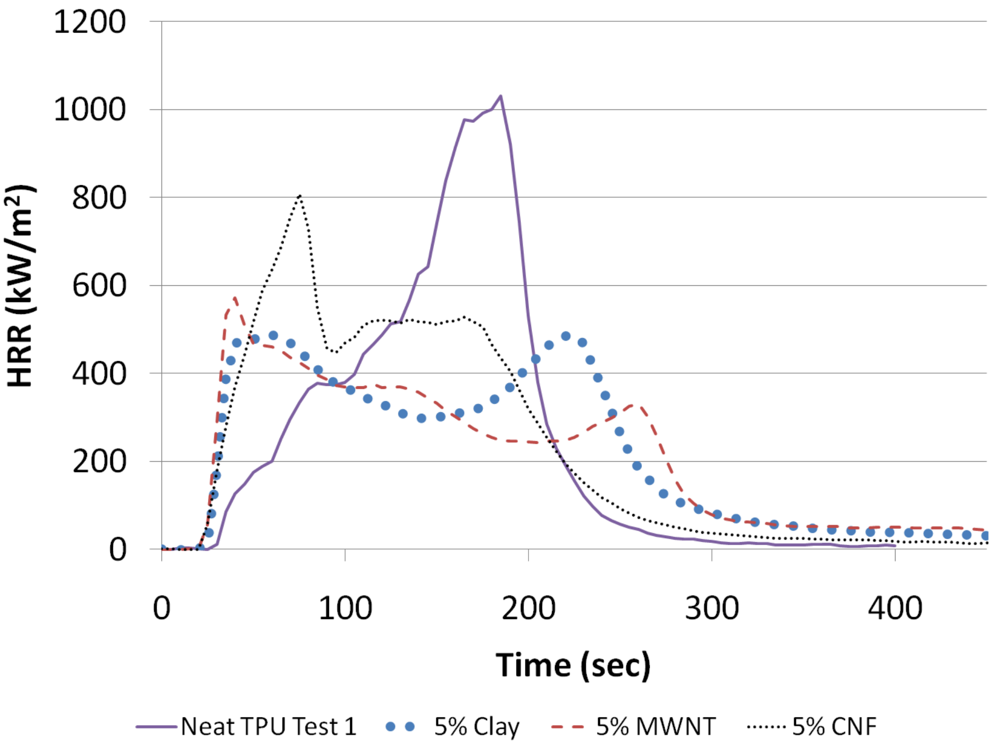

Figure 4.16. HRR of neat and 5% PNC – cone calorimeter, 50 kW/m^2.

The flammability properties are shown in Table 4.5. The material's time to sustained ignition is not affected by the addition of nanoclay. However the carbon-based PNCs both decrease the time to ignition by 25%, likely due to the higher thermal conductivity. The suppression of PHRR in the PNC is significant, 50%, 45%, and 22% from the nanoclay, MWNT, and CNF PNCs respectively. The effective heat of combustion is the same for each material since the mass of each material are not drastically different. The average specific extinction area (SEA) is also decreased by each of the PNCs (4%) but most significantly decreased by the nanoclay PNCs (18%). The higher values in the carbon-based PNCs (SEA) are due to the high soot contents of the carbon-based PNCs and the fact that the nanoclay PNC serves as a good gaseous barrier.

Table 4.5. Summary of cone calorimetry data at irradiance heat flux of 50 kW/m^2.

Material	t_{ig} (s)	PHRR (kW/m^2)	Avg. HRR, 60s (kW/m^2)	Avg. HRR, 180s (kW/m^2)	Avg. Eff. H_c (MJ/kg)	Avg. SEA (m^2/kg)
Neat TPU (1)	28	1031	228	515	27	311
5% Clay	27	518	442	376	28	256
5% MWNT	21	571	436	492	28	297
5% CNF	21	808	508	361	27	298

t_{ig} = Time to sustained ignition; PHHR = Peak heat release rate; Avg. HRR = Average heat release rate after ignition; Avg. Eff, H_c = Effective heat of combustion; Avg. SEA = Average specific extinction area

The materials after firing are shown in Figure 4.17 to Figure 4.19. The nanoclay material is shown to expand. This can be associated with the material's gaseous barrier properties. The side image in Figure 4.17 shows the height growth of the material. In comparison the CNF PNC material stays relatively flat. The center of the post test CNF sample shows cracking which is not observed in the nanoclay materials. Lastly, the MWNT post firing samples have a red pigment due to the iron catalyst used to produce the MWNTs. This material is also flat and does not have the char structure that is observed in the nanoclay sample.

Figure 4.17. Post Desmopan® 6065A 5% Cloisite® 30B calorimeter samples.

Figure 4.18. Post Desmopan® 6065A 5% CNF calorimeter samples.

Figure 4.19. Post Desmopan® 6065A 5% MWNT calorimeter samples.

4.4. CONCLUSION

Both a vertical UL 94 and a horizontal cone calorimeter experiment were performed. The vertical UL 94 burn test showed the low viscosity of the melt TPU and how significantly each nanomaterial modified the melt and burning conditions of the PNC. The mechanical stability of the PNC char after the flame test is increased as the nanomaterial loading is increased. This is measured by the time a charred segment takes to fall and the size of the charred segments that do fall. The failure mechanism of each TPUN is different. Cracks appear in the nanoclay and MWNT specimens. Nanoclay loadings above 7.5 wt% show no cracking and as a result no charred segments dropped. The surface of the CNF specimens did not create char-like structure until a much higher loading was added. At low loadings, the specimen burned like a very viscous melt. At higher loadings the CNF specimens behaved similar to that of the MWNT. These flammability tests show that adding nanomaterials to TPU drastically change the viscosity, mechanical properties, and flammability properties. With additional nanomaterials, the material keeps its structure for a longer period of time. The nanoclay additives show superior enhancement and the CNF additives show weak enhancements even at the high 20% loading.

The cone calorimetry experiments show that the neat TPU has significantly higher PHRRs in comparison to the PNCs tested. The enhancements of the MWNT and nanoclay PNCs to lowering the PHRR are both equally significant. The time of ignition however is actually lowered by the addition of CNF and MWNT nanomaterials. The nanocarbon PNCs also have a significantly higher SEA compared to the nanoclay PNC. The final char structure in this test is also found to be best in the nanoclay PNC, it expands during testing and keeps a continuous surface. In comparison the final sample of

CNF is a thin char with cracks and the final MWNT structure is a dispersed red pigmented residue.

SEM images of carbon-based PNC burned residue show that the remaining material is a network of the MWNT or CNFs. During the burning process, as the material degasses, the MWNT and CNFs collapse upon itself. Islands of MWNT and CNFs are then formed. These island-network residues are observed in the flammability experiments of the MWNT as cracks in UL 94 specimens and as the dispersed powder and iron oxide residue in the cone calorimeter tests. In the CNF PNC UL 94 experiments a weak char is formed resulting in a viscous melt. Although still a weak char, the higher weight loadings mean a more continuous char layer can be formed. In cone calorimeter experiments, where viscosity is not a factor, the CNF char is found to be very soft. The nanoclay specimens also collapse as the residue degasses. However since nanoclay specimens are platelet sheets, the residue is a more continuous char layer. This is observed in the strong UL 94 char and the dome like cone calorimeter char formed due to the materials gaseous barrier.

These flammability experiments show that the nanoclay specimens perform the best under these conditions by creating the strongest char. In addition to not having segments drop in the higher weight loading UL 94 burn tests, the nanoclay PNCs are found to outperform the carbon-based PNCs in each of the measured values in the cone calorimeter experiment. Compared to the carbon-based PNCs the nanoclay segments tested in cone calorimeter experiment: lost the least mass, suppressed PHRR the most, maintained the time of ignition (the carbon-based PNCs decreased the time of ignition), and decreased the SEA the most.

Chapter 5. Exhaust Gas Studies

5.1. INTRODUCTION

Spectra data of exhaust gas specimens that are produced from a TGA experiment heated at 20^{o}C/min are studied with Fourier Transform Infrared Spectroscopy (FTIR) on the neat TPU as well as the 7.5% MWNT, 5% Clay, and 10% CNF PNC specimens in a nitrogen environment. A steel transfer line is connected to the exhaust of the Q5000 IR TGA, described in section 3.4, and a Nicolet 6500 FTIR. The 9.144m (3 ft) long transfer line is wrapped in insulation and is heated and maintained at 300^{o}C for the duration of the experiment. A concern for the long transfer line is that certain gas components may take longer to travel down the transfer line because it is heated only up to 300^{o}C. The data is obtained for a low heating rate of 20^{o}C/min because too high of a heat heating rate would be difficult to distinguish different species corresponding to different decomposition phases.

Figure 5.1. Q5000 TGA and Nicolet 6700 FTIR with transfer line. (TA Instruments)

Before the experiment is run a background, Figure 5.2 is taken and subtracted from the experimental spectra. As the temperature increases there appears to be a small drift in the background, this however is small in comparison with the absorbance spectra. To analyze the different spectra the exhaust components contain, a library of identified spectra compositions in the OMNIC 8.0.0.313 software from Thermo Scientific is used.

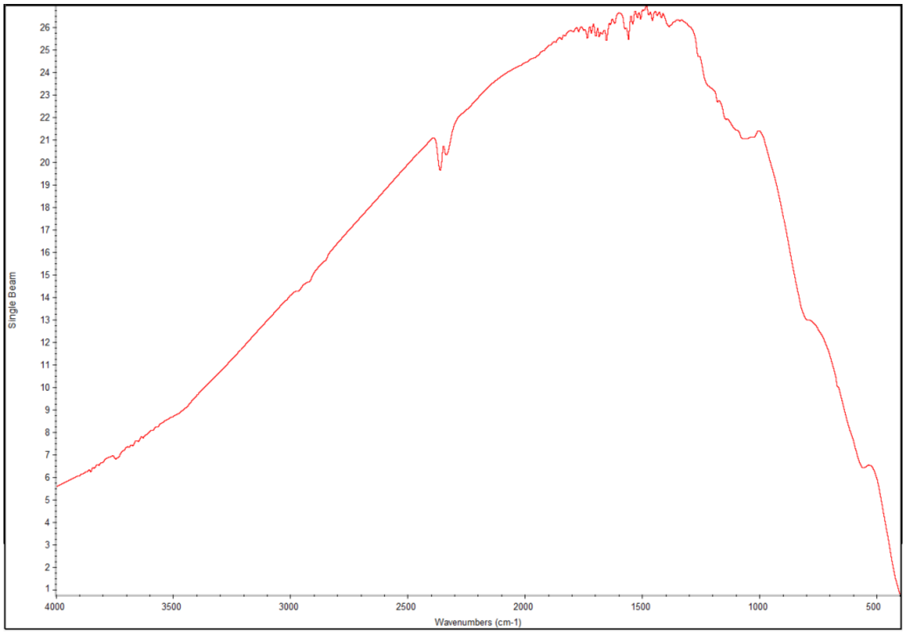

Figure 5.2. Background spectra.

5.2. FTIR RESULTS

The rate of decomposition in the TGA is observed to closely match the shape of the FTIR total absorbance band, Gram-Schmidt. Figure 3.29 show the TGA and DTGA curve of the environment these FTIR spectra are obtained from. Data sets are taken and averaged over every 30 second time interval so the Gram-Schmidt, Figure 5.3, is a blurred representation of the DTGA curves.

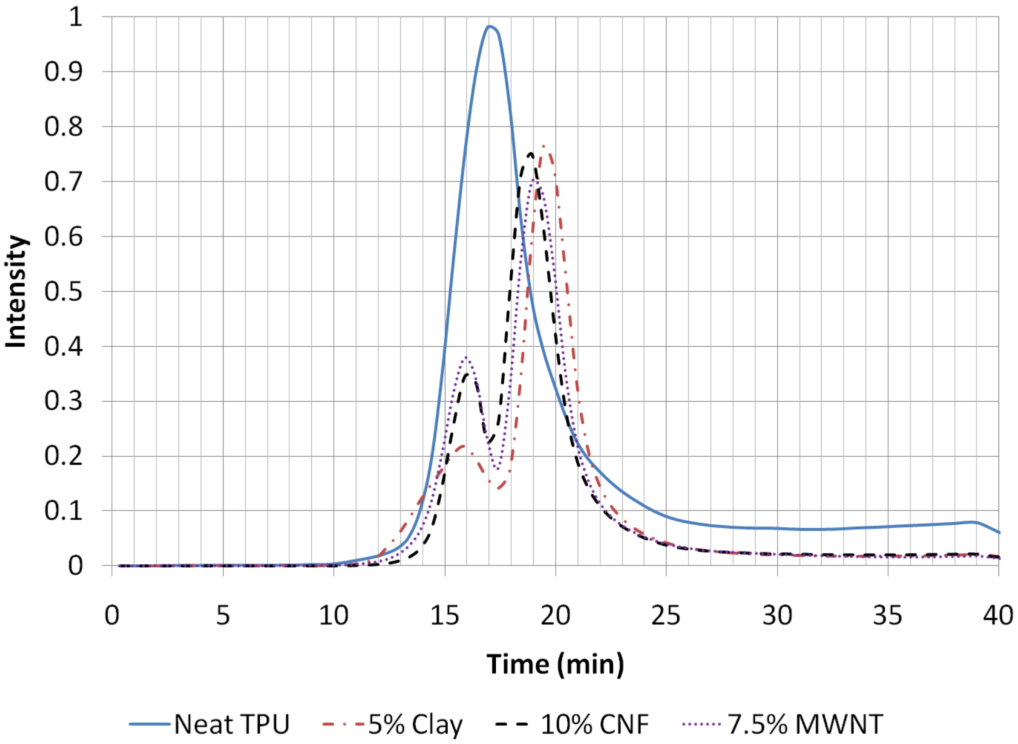

Figure 5.3. Total absorbance of PNCs exhaust of TGA at heating of 20°C/min.

From the observed Gram-Schmidt curves, the most significant areas of degradation occur between 15 and 20 minutes. The two reactions shown in the peaks of the PNC Gram-Schmidt curves are not as clearly observed in the neat TPU. The peaks observed in each of the PNCs occur at roughly the same time. The neat TPU has a peak at 17 minutes, whereas the PNCs 1st peak reaction occurs at 16 minutes and the 2nd peak reaction occurs between 19 and 20 minutes. The spectra over this time range are analyzed. The CO2 and isocyanate spectra lie very close to each other and are difficult to distinguish in some spectra.

The spectra taken at 16 minutes are shown in Figure 5.4. A strong CO_2 band is observed in the TPU and PNCs. The isocyanate peak is very strong in the MWNT and CNF PNCs. The isocyanate peak is less visible in both the nanoclay PNC and neat TPU samples as the CO_2 band in these two materials dominates at this time. During this first reaction peak, the PNC samples show only a small signal related to the ether group. The neat TPU in comparison shows an equally strong signal related to the ether group.

At the 18 minute mark, Figure 5.5, the neat TPU ether signal is about twice as strong as it was at 16 minutes. The ether group now dominates the decomposition products of the MWNT and CNF PNCs. The nanoclay PNC in fact has a very low signal at this point and its spectrum is balanced between CO_2 and ether. At the 20 minute mark, Figure 5.6, the decomposition of the neat TPU has significantly decreased. Even at this point CO_2 and ether are detected in the decomposition gases. Each of the PNC formulations' CO_2 and isocyanate bands do not show. Only the ether group is actually shown in these spectra.

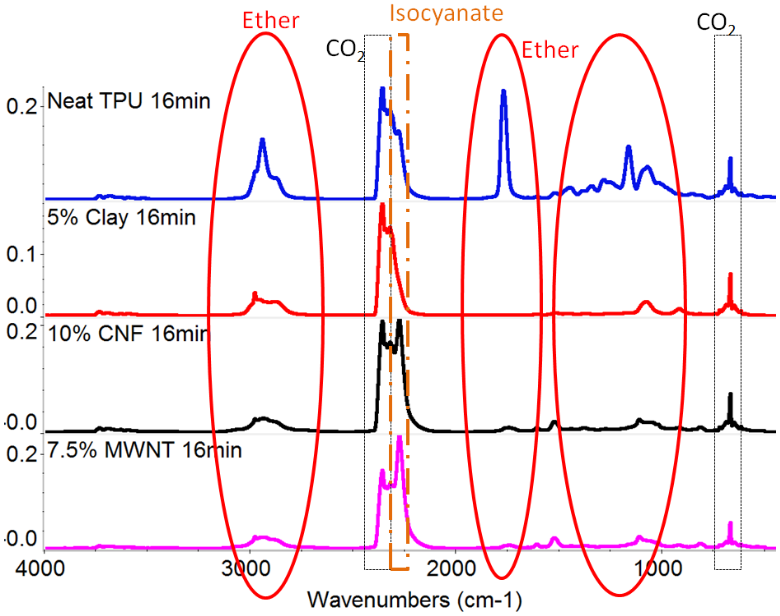

Figure 5.4. FTIR spectra at 16 min.

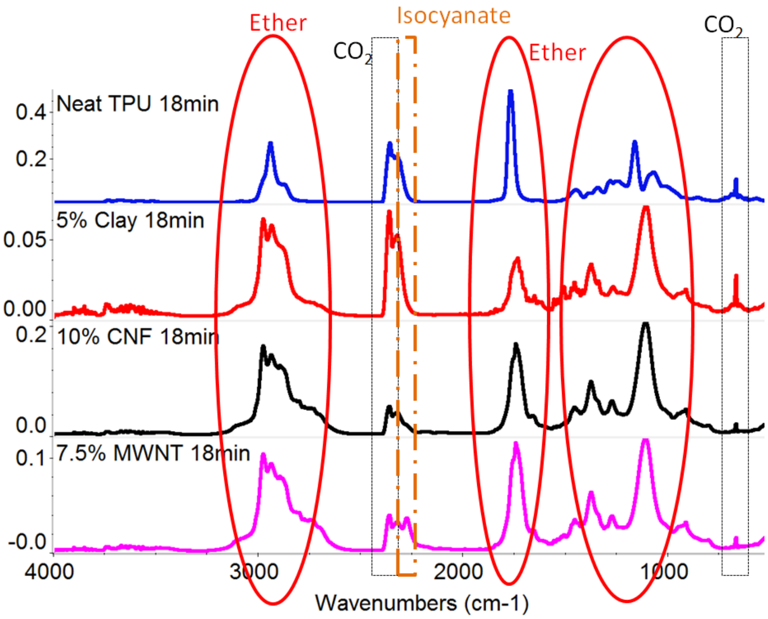

Figure 5.5. FTIR spectra at 18 min.

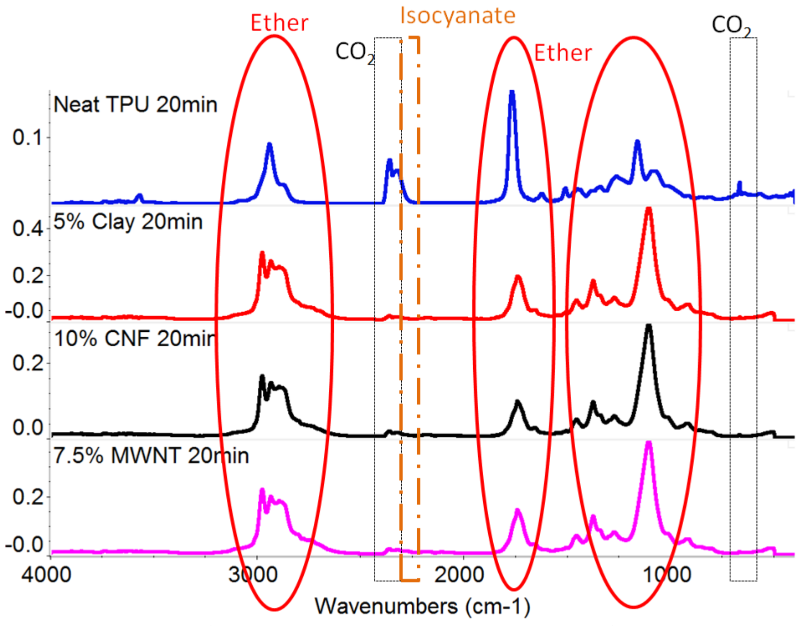

Figure 5.6. FTIR spectra at 20 min.

In all of the spectra taken, there are essentially 5 regions of peaks associated with decomposition of gases of CO_2, isocyanate, and ether. To compare the gas compositions observed more closely specific wavenumber time history curves are compared: The neat TPU spectra peak include: 2940 cm^{-1} (CH_2), 2360 cm^{-1} (CO_2), 2274 cm^{-1} , 1770 cm^{-1} (C=O), 1166 cm^{-1} (C-O-C), and 668 cm^{-1} (CO_2). The spectra at 2360 cm^{-1} and 668 cm^{-1} represent the CO_2 wavenumbers. The spectra at 2274 cm^{-1} represents the isocyanate. And the spectra at 2940 cm^{-1}, 1770 cm^{-1}, and 1166 cm^{-1} represent the ether chain loss. The PNC spectra of CO_2 as well as isocyanate are also observed. However, the ether spectra observed in the PNC appears to be different. Instead of a strong peak at 2940 cm^{-1} a broad spectra is observed between 2865 cm^{-1} and 2975 cm^{-1}. In addition, a shift from peaks occurring at 1770 cm^{-1} and 1166 cm^{-1} in the Neat TPU are instead observed at 1740 cm^{-1} and 1110 cm^{-1}. Although these spectra are close the observed shift is clear and consistent.

From the spectra observed in the neat spectra history, Figure 5.7, it is clear that the decomposition of the isocyanate is occurring before the ether and CO_2 time peaks. It is also observed that the peak at 1774 cm^{-1} is about two times of the other signal peaks. The peak at 2276 cm^{-1} occurs at 15.5 minutes and the other peaks occur at 17 and 17.5 minutes. Each of the PNC formulations show a combination of two times when spectra time peaks occurs. The PNC peaks of the 2361 cm^{-1} and 2273 cm^{-1} wavenumbers occur at 16 minutes and the 2941 cm^{-1}, 1740 cm^{-1}, and 1110 cm^{-1} peaks occur at 19.5 minutes.

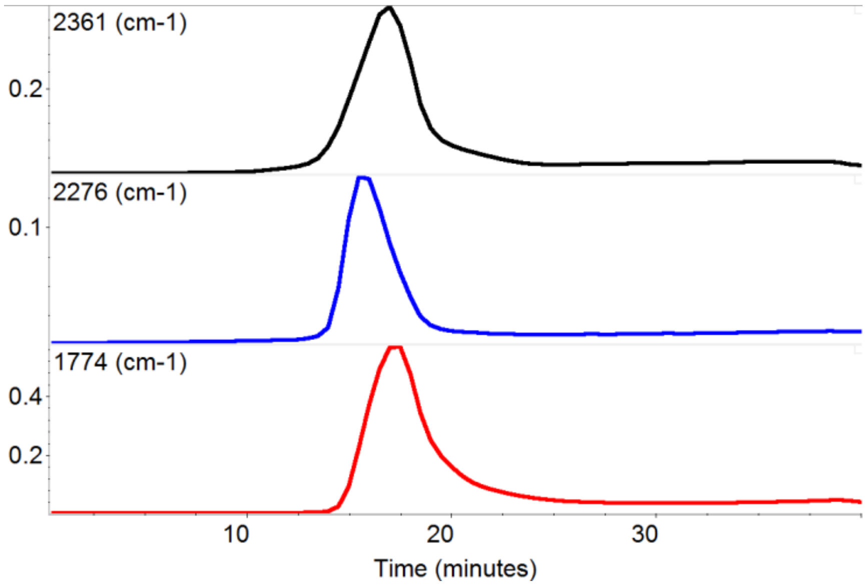

Figure 5.7. Peak neat TPU spectra time history.

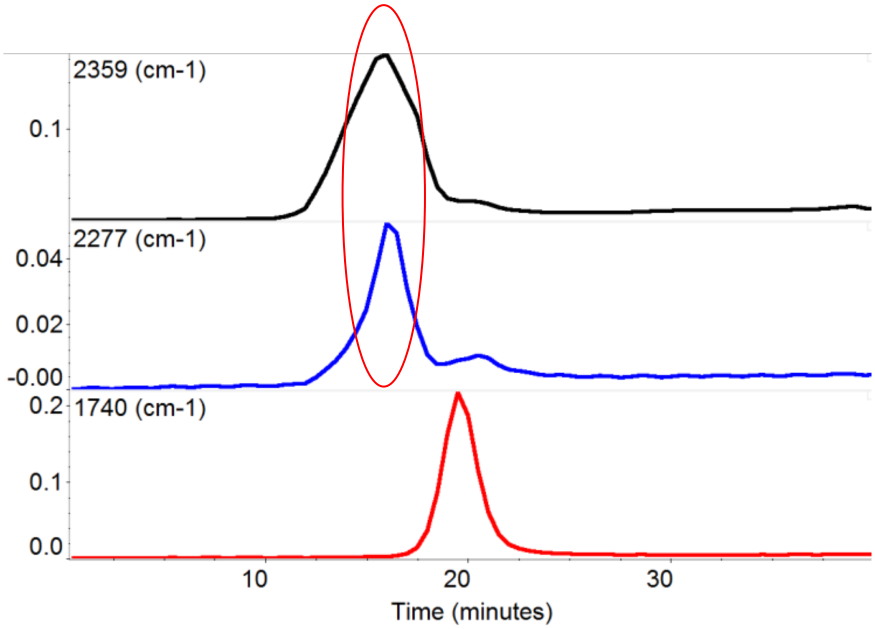

Figure 5.8. Peak 5% clay spectra time history.

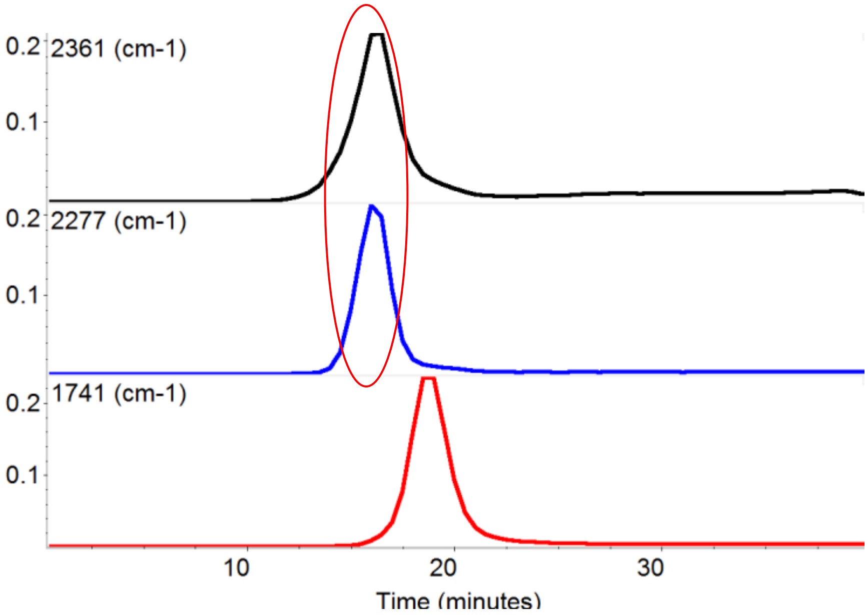

Figure 5.9. Peak 10% CNF spectra time history.

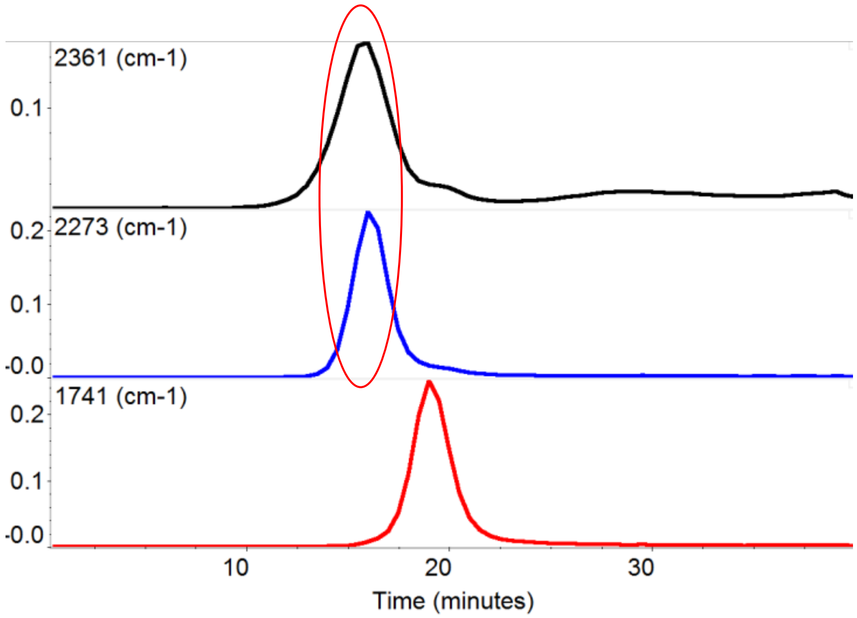

Figure 5.10. Peak 7.5% MWNT spectra time history.

5.3. CONCLUSION

The FTIR data shows a distinct difference in reactions occurring during the decomposition of neat versus nanomodified PNCs. At the beginning of the experiment small traces of CO_2 are observed, water content even at this stage is low (<10% of CO_2 trace). The neat TPU is observed to evolve CO_2, isocyanate, and ether peaks throughout the two step degradation time of interest (16-20 min.). The spectra time history shows that the peak CO_2 and ether spectra occur during the second reaction of the neat TPU degradation. However, the CO_2 peak occurs during the first reaction of the PNC degradation. In fact both the isocyanate and CO_2 traces are no longer observed after 20 minutes, in the PNC spectra.

Since this shift is observed in all three PNCs and not solely in the nanoclay PNC, the mechanism which affects the change in spectra is not that a gaseous barrier is formed, but that the nanomaterials effectively are serving as hard segments. Since no CO_2 or isocyanate is observed during the second reaction, the nanomaterials are acting as hard segments undergoing the depolymerization process. However in this case the polyether group is the only product. During this reaction the ether is not breaking down into further components as CO_2 traces would then be observed. During the first reaction of decomposition, any of the three dissociation processes are occurring, since the CO_2 and isocyanate peaks are observed. However the bonds do not break in the ether chain such that they are not detected until the second reaction. The ether chains are held by the nanomaterials.

Since CO_2 traces are observed throughout the neat TPU: secondary dissociation and CO_2 removal processes are occurring. Thermal stability of the PNC is enhanced by the decomposition process of the PNCs because the nanomaterials delay decomposition of the ether group. This is observed in the first DTGA peak. The first DTGA peak of the neat TPU is higher than that of the PNCs’ because the decomposition of ether in the neat TPU is occurring. The second DTGA peak of the neat TPU is lower than that of the

PNCs' because the delayed ether products are then released. In this stage the neat TPU ether products are broken down into smaller products, this is not the case in the PNCs. This is the reason that the neat TPU continues to degrade after the PNCs stop degrading.

Chapter 6. Solid Rocket Motor Testing

6.1. HYBRID ROCKET TESTS

Char strength of material tested in rocket environments is an area that has very little consistency in literature. Often it is described subjectively and measured in terms of char thickness. The first thing that this project needed was to expose the PNC materials to rocket environments. The flammability experiments performed in Chapter 4 are all charred materials however the heat fluxes, surface shears, and pressures are nowhere close to rocket environments. Work had been planned to test the materials at a simulated solid rocket motor (SSRM) at Texas State University. Unfortunately the test setup has been down for an extended period of time. The materials for this set of testing will be continual work that will be done beyond the work presented here.

Fortunately a local high school in Fredericksburg, Texas is involved with rocket testing. Brett Williams is the director of IGNITE as well as the high school teacher leading this effort. IGNITE is a NASA funded nonprofit organization meant to help educate high school students on rocket testing. The work that these students have been able to perform is very impressive and very much appreciated.

The setup is a static hybrid rocket test. A 4130 steel frame is used to secure the rocket which is tested horizontally, Figure 6.1. Three gas tanks are used, N_2 at 2.1 MPa (300 psi), N_2O at 5.2 MPa (750 psi), and O_2 at 552 kPa (80 psi). Initially the oxygen tank is opened, 2.5 seconds later the igniter is lit. At 0.5 second after that, N_2 is flowed. The flow of N_2 opens a Moog valve and allows the N_2O to flow through the test cell. After the specified burning duration, N_2 continues to flow through the rocket in order to purge the environment. About 1 lb of N_2O is contained downstream of the manifold and is also purged at the end of the test. To help with the initial burning process steel wool is drawn along the center of the propellant.

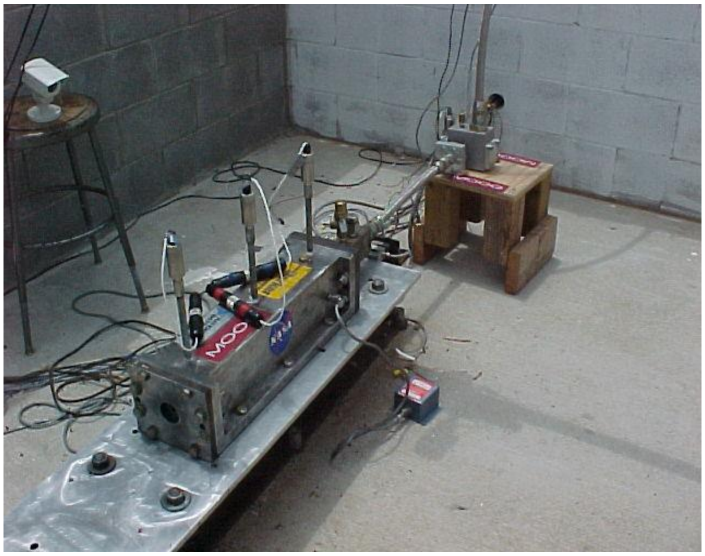

Figure 6.1. FHS Hybrid Rocket Test Setup

The entire rocket test bed is 53cm (20.875”) long with a 10.2cm (4”) diameter. A cardboard phenolic tube is used to hold the propellant. The group cures the propellant in the phenolic tube. The 33cm (13”) propellant is placed in the middle of the tube such that 10cm (3.9375”) remains on both ends which contain the pre mixing and aft mixing areas, Figure 6.2a. After the tube is secured an additional 1.27cm (0.5”) thick graphite disc is used as the nozzle.

Ablative materials are tested in the aft mixing area. In every firing EPDM/Kevlar is used as a baseline material. Two PNCs are also added, Figure 6.2b. Materials were adhered to the phenolic tube with 3M Scotch-Weld Epoxy Adhesive 2216 B/A. The materials are 10.2 cm x 10.2 cm x 3.175 mm (4” x 4” x 1/8”) panels. These materials were fitted as tightly as possible to prevent gaps between the materials which would degrade the phenolic tube from the backside. Additional RTV and thin pieces of Kevlar/EPDM are also used to protect the material interfaces.

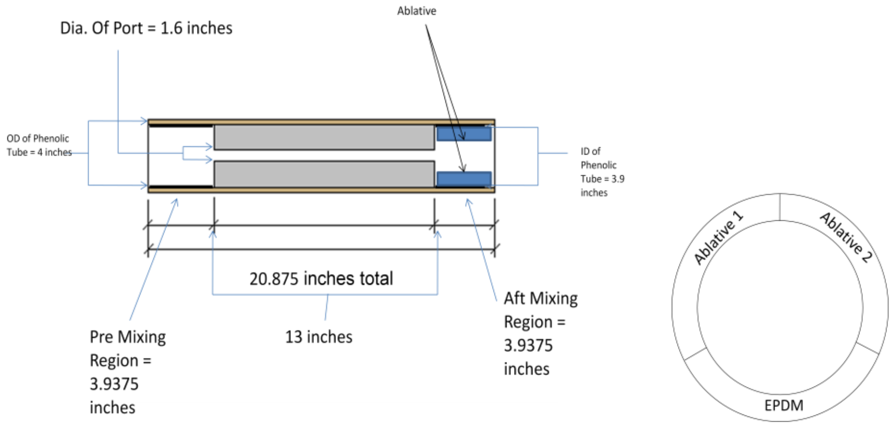

(a) (b)

Figure 6.2. (a) IGNITE small scale hybrid rocket diagram and (b) sample layout.

The two rocket fuels that these materials were tested in are polybutadiene acrylonitrile (PBAN) and hydroxyl-terminated polybutadiene (HTPB). These materials were selected for the close thermal properties described in the provided NASA combustion program. Three firings of each propellant are performed on the different materials as shown in Table 6.1.

Table 6.1. Materials tested in each propellant firing.

Firing #1	**Firing #2**	**Firing #3**
EPDM	EPDM	EPDM
Desmopan 10% Clay	Desmopan 10% MWNT	Desmopan 20% CNF
Desmopan 7.5% Clay	Desmopan 7.5% MWNT	Desmopan 15% CNF

6.1.1. Results

In all tests conducted the EPDM material survived with minimal ablation. The first test conducted is a 20 second burn test using HTPB fuel. The 15% and 20% CNF samples failed completely. The PNC as well as the phenolic tube are completely burned away. Because of this result, the next test is performed with a shorter duration in order to obtain more of PNCs for post testing. A 15 second HTPB burn test is performed on the EPDM and MWNT samples. Figure 6.3 shows that the entire EPDM surface is maintained. Based on the MWNT PNCs it appears that there are 3 sections within the aft section. In the 7.5% MWNT samples only the bottom section, the section closest to the propellant, survived. In the 10% MWNT sample the top and bottom section both survive. The center section experiences the highest degree of ablation.

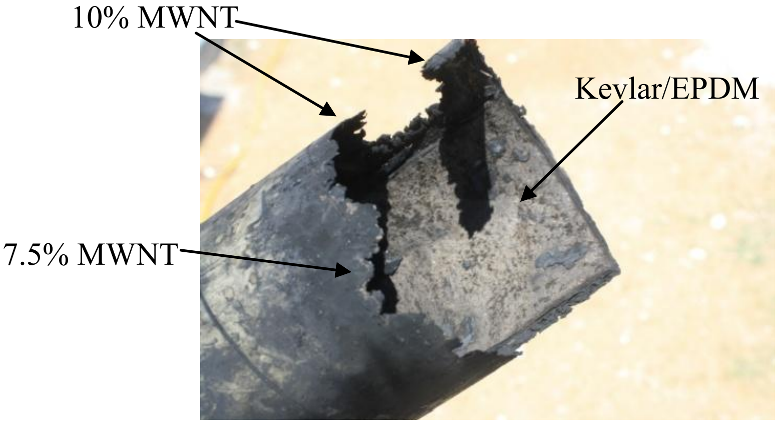

Figure 6.3. MWNT and EPDM after 15 sec. HTPB burn.

The areas of the phenolic tube behind the ablatives that have survived maintain their original color indicating that in fact these sections are protected by the ablative. In Figure 6.4 the interface between the 10% MWNT and EPDM materials is also shown to survive. This small section within the center of the aft section does not survive on the

7.5% and 10% MWNT material interface. This implies that the center region in fact is ablated due to the fact that the 7.5% MWNT adjacent to it had ablated away. Since the EPDM edge adjacent to the 7.5% MWNT had also survived, this indicates that the adhesive is not the reason for the 10% MWNT failure in the center section. At the end of the tests flakes of materials, Figure 6.5, were found on the floor of the rocket. These flakes are about 2.54 cm (1") in diameter and indicate that a layer of char is formed and sheared off the surface.

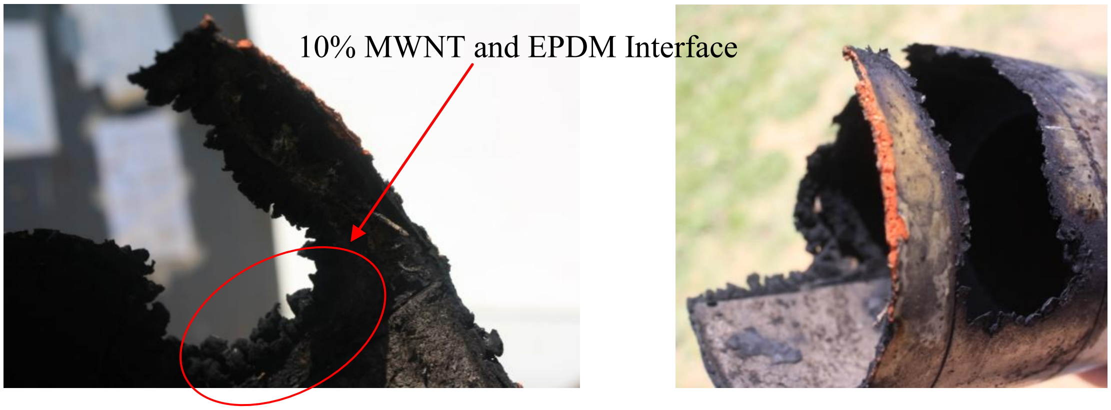

Figure 6.4. 10% MWNT after 15 sec. HTPB burn.

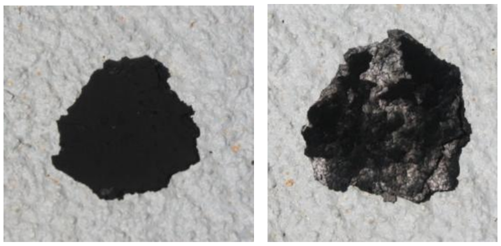

Figure 6.5. Charred flake (front and back) from MWNT and EPDM 15 sec. HTPB burn.

The third test is run with an even shorter duration to obtain more material for post test analysis. A 10 second HTPB burn is performed on the nanoclay and EPDM materials. In this test both the 10% and 7.5% nanoclay samples survived completely. Similar to the post test materials of the cone calorimetry tests the surface of the nanoclay samples expands upwards. The bottom and middle sections of the nanoclay sample have a yellow pigment. This indicates that not all of the material has charred. The charred surfaces in this area must have blown off during the purge since if it blew off during the burn the next layer of material would have also charred.

Figure 6.6. Clay and EPDM after 10 sec. HTPB burn.

From the results of the HTPB burn tests a 10 second burn appeared to be the best choice for post material testing. Ten second PBAN burn tests are performed on the three different firings. Even at this low time scale the CNF samples did not survive. The MWNT samples performed slightly better compared to the 15 second HTPB burn results. The top and center region of the 7.5% MWNT sample has burned off as well as the center region of the 10% MWNT sample, Figure 6.7. The yellow pigment on the nanoclay materials is also observed, Figure 6.8. In this case however a 2.54 cm (1”) long section of the 7.5% nanoclay specimen had burned through, Figure 6.9.

Figure 6.7. MWNT and EPDM after 10 sec. PBAN burn.

Figure 6.8. Clay and EPDM after 10 sec. PBAN burn.

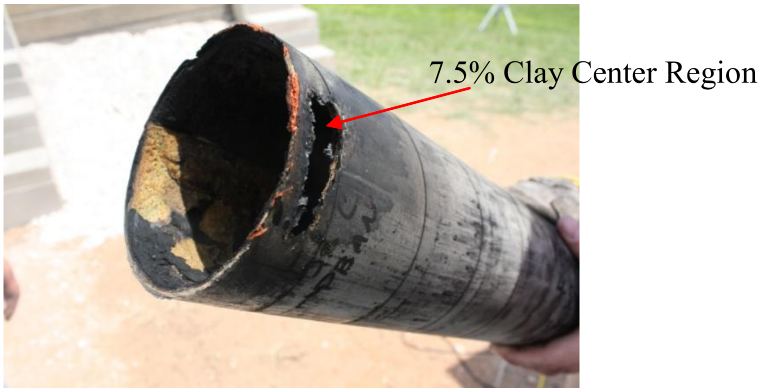

Figure 6.9. 7.5% Clay after 10 sec. PBAN burn.

Pressure measurements are taken in the pre mixing and propellant sections. The initial fuel grain diameter center hole is 4.2 cm (1.66”). After the test is performed the center hole diameter is measured to assess the regression rate of the fuel grain. The 10 second PBAN tests have an average post fuel grain hole diameter of 6.4 cm (2.52”) which is correlated to a 0.22 cm/sec (0.086 in/sec) regression rate. The graphite nozzle regression rate is also measured. With an initial diameter of 1.95 cm (0.769”) and an average post test diameter of 2.0 cm (0.787”) is a 0.005 cm/sec (0.0018 in/sec) regression rate is measured in the PBAN experiments. The details of each individual PBAN and HTPB test result are shown in Table 6.2 and Table 6.3.

Table 6.2. PBAN fuel grain and graphite nozzle regression.

Ablative	(10 sec) MWNT	(10 sec) Clay	(10 sec) CNF
Post Test Nozzle Diameter (cm)	2.00	2.01	1.99
Nozzle Regression Rate (cm/sec)	0.005	0.006	0.004
Post Test Fuel Grain Diameter (cm)	6.35	6.40	6.45
Nozzle Fuel Grain Rate (cm/sec)	0.21	0.22	0.23

Table 6.3. HTPB fuel grain and graphite nozzle regression.

Ablative	(15 sec) MWNT	(10 sec) Clay	(20sec) CNF
Post Test Nozzle Diameter (cm)	2.00	1.96	2.10
Nozzle Regression Rate (cm/sec)	0.003	0.00025	0.007
Post Test Fuel Grain Diameter (cm)	6.27	6.83	7.32
Nozzle Fuel Grain Rate (cm/sec)	0.138	0.263	0.156

Pressures during the testing of these materials were also obtained. Pressure transducers are placed at the center of the premix and fuel grain regions. The pressures measured along the regions are very similar. The pressures in the HTPB, Figure 6.12, show that when the ignition begins a peak pressure of 2.4 MPa is experienced. There is a pressure drop of in both the 15 and 10 second burns at 3 seconds and 10 second respectively. More consistent results are obtained in the PBAN tests, Figure 6.10, which shows a max initial pressure between 2.9 MPa and 3.4 MPa and a stabilized pressure of 1.8 MPa. The thrust measurements are consistent with the pressure changes, Figure 6.11 and Figure 6.13.

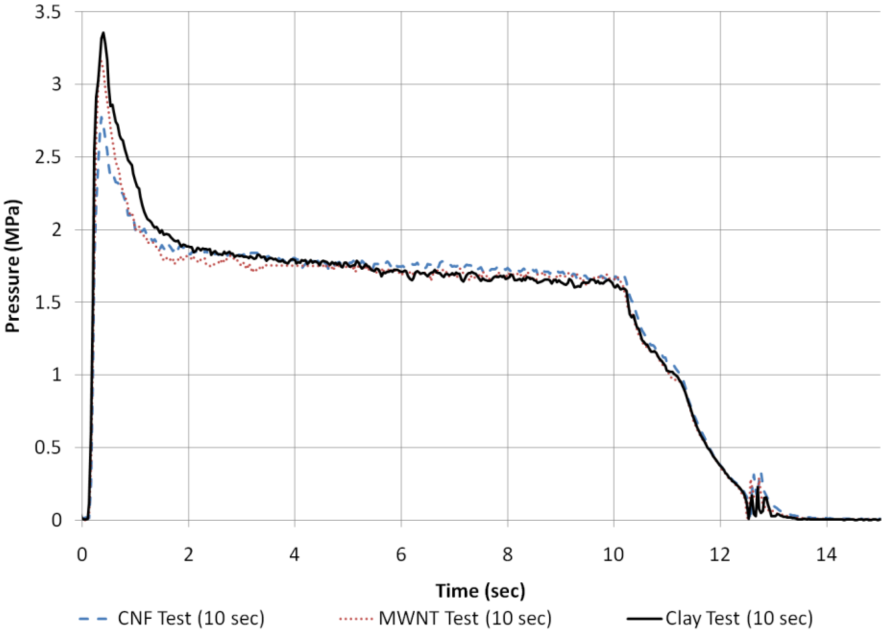

Figure 6.10. PBAN pressure measurements.

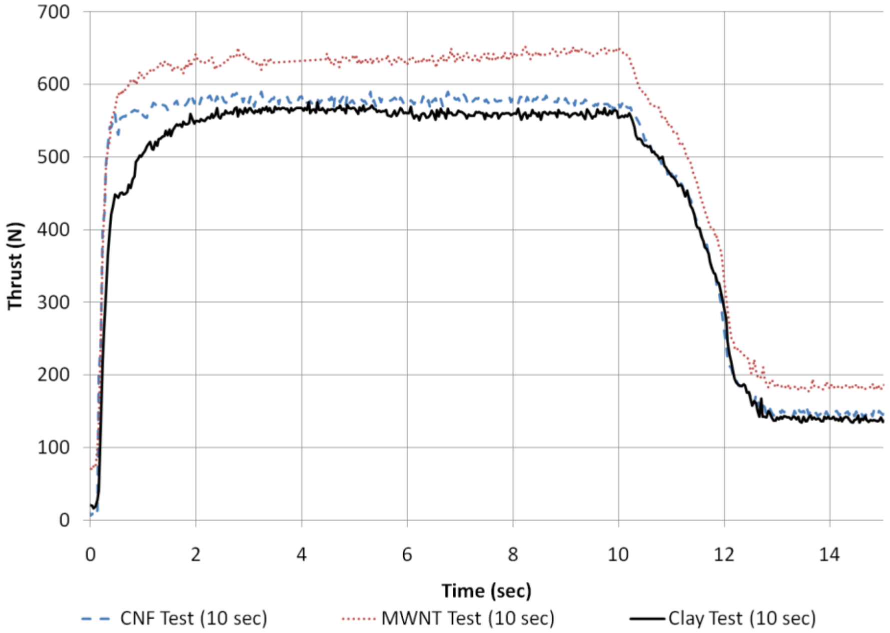

Figure 6.11. PBAN thrust measurements.

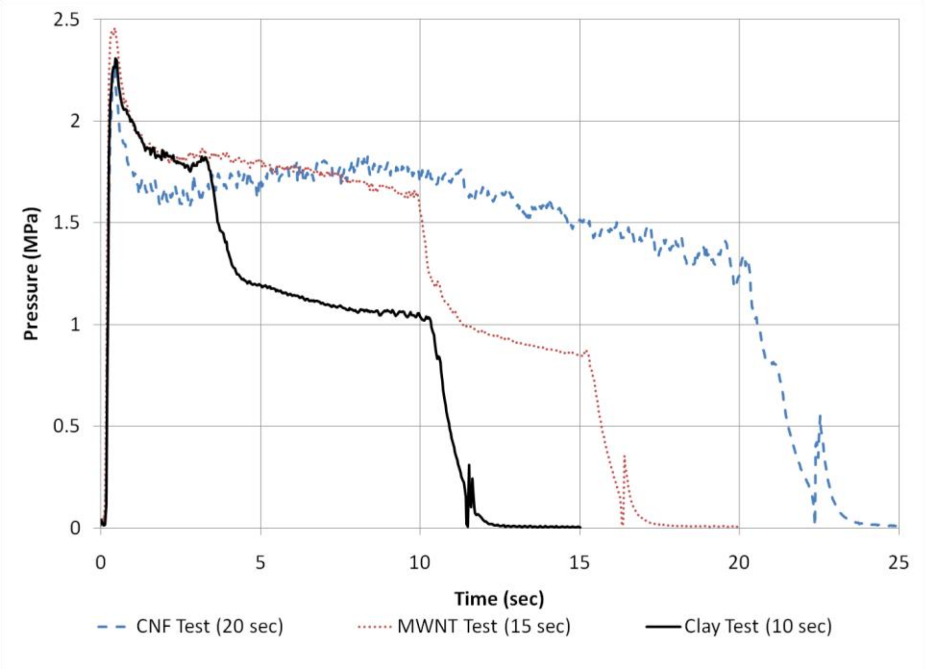

Figure 6.12. HTPB pressure measurements.

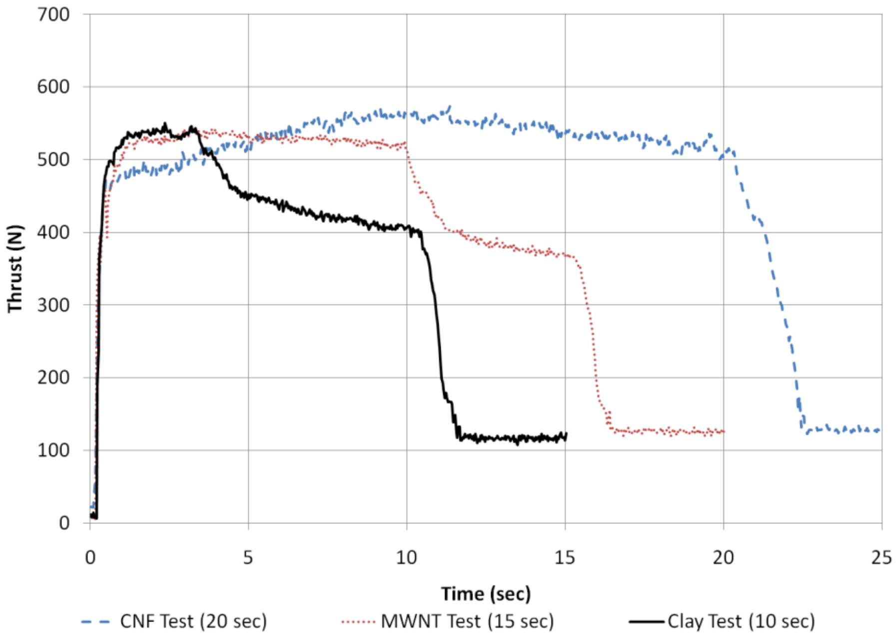

Figure 6.13. HTPB thrust measurements.

6.2. CHAR STRENGTH TEST

Char strength measurements in post tests analysis is an important way of measuring the different ablative performance. Many will look at a material and examine the thickness of char, brush off the char region and then measure the pyrolysis zone. A more consistent quantitative method is desired. Two undergraduate senior design teams have been tasked with the development of a new approach to measure char strength. There is limited research being conducted in this area. Jaramillo, Edd, Wells, and Koo (2010) have built on the work of Reshetnikov, Garashenko, and Strakhov (2000). Jaramillo has been closely working with me on this portion of the project to ensure that good results are obtained.

A compression test method is used, Figure 6.14. A Tekscan piezoresistive load cell measures the force required to break a char sample as a potentiometer measures the distance traveled by a linear actuator. The main concern in this experimental setup is the sensitivity of the force measurements. The char being tested is weak relative to most compression test setups. The linear actuator travels at 1.27 cm/sec (0.5 in/sec) towards the sample and 0.254 mm/sec (0.01 in/sec) while in contact with the sample.

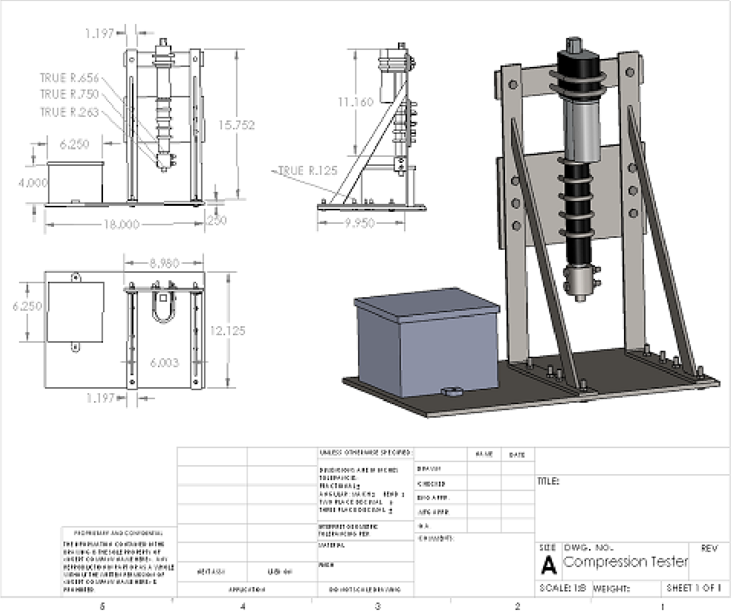

Figure 6.14. Char sensor assembly. (Jaramillo 2011)

Calibration of linear distance is performed by measuring the potentiometer voltage at different distances, and calibration of the force response is performed using a spring with a known spring constant. Four springs with a k-constant of 8.23 kN/m (47 lbf/in) are used in series, Figure 6.15. Preliminary strength tests measurements have been performed on a char 10% MWNT sample and it was realized that the motor's duty cycle may need to be adjusted depending on the strength of the char. A different calibration may be required for each individual duty cycle. This test setup will be used on the hybrid rocket motor samples at different locations to determine and compare char strengths of the different materials.

Figure 6.15. Char strength measurement devise.

6.3. OXYACETYLENE TORCH TESTS

High heat flux experiments are conducted by Dr. Maurizio Natali at the University of Perugia, Italy, who is currently working with another senior design group in setting up an oxyacetylene torch for ablation testing at UT Austin. Ablation tests are performed on samples at Natali's laboratory facility (Natali, 2009). The material is exposed to the hottest portion of the flame, with a 7mm flame diameter, for 25 seconds. Samples of 12.7mm x 12.7 mm x 5 cm are cut out of a 12.7 mm x 10.16 cm x 10.16 cm (½" x 4" x 4") compression pressed sheets, Figure 6.16 and Figure 6.17. The torch is directed towards the square face (12.7 mm x 12.7 mm). In this orientation the sample may be tested twice.

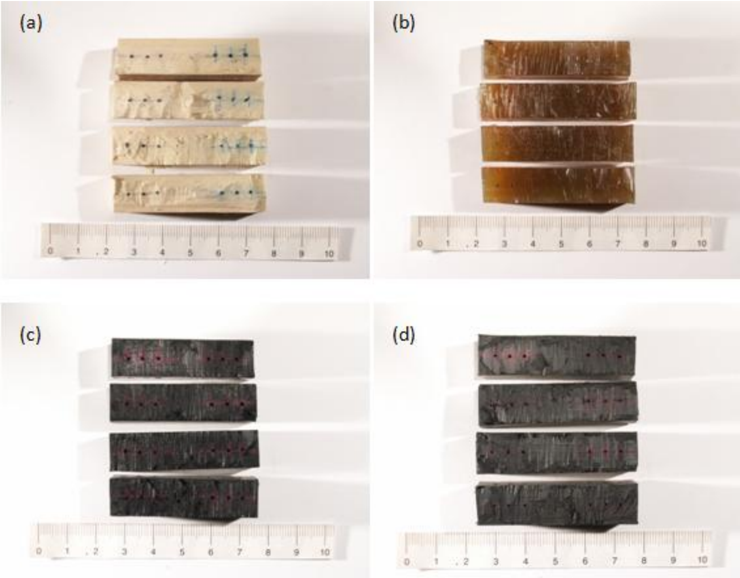

Figure 6.16. Oxyacetylene Torch Samples Top View (a) Kevlar EPDM, (b) Nanoclay 10 wt%, (c) MWNT 10 wt%, and (d) CNF 20 wt%.

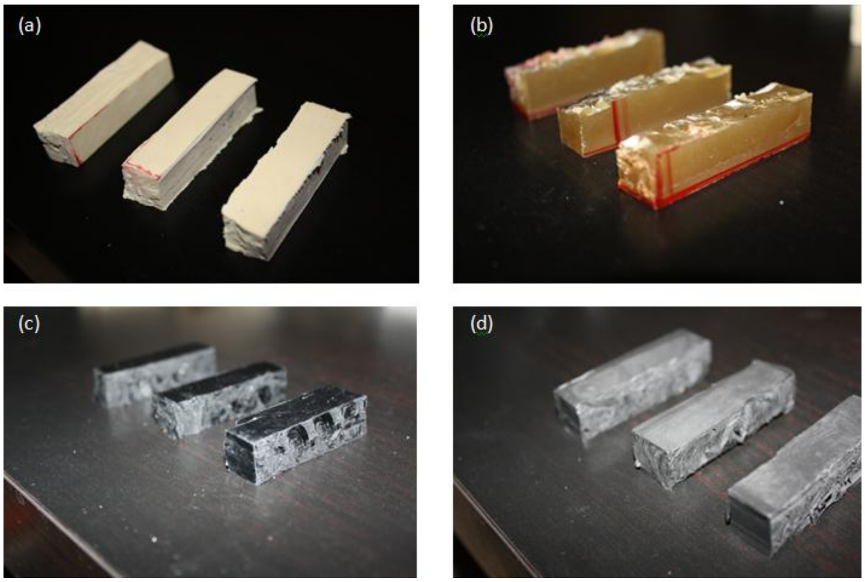

Figure 6.17. Oxyacetylene Torch Samples Top View (a) Kevlar EPDM, (b) Nanoclay 10 wt%, (c) MWNT 10 wt%, and (d) CNF 20 wt%.

At 5 mm increments three thermocouples are embedded into the center of the specimen, Figure 6.18, to measure the in-depth heat soak temperature during testing. Thermocouples are drilled into the specimen at both ends for the possibility of testing a single specimen twice depending on the ablation rates.

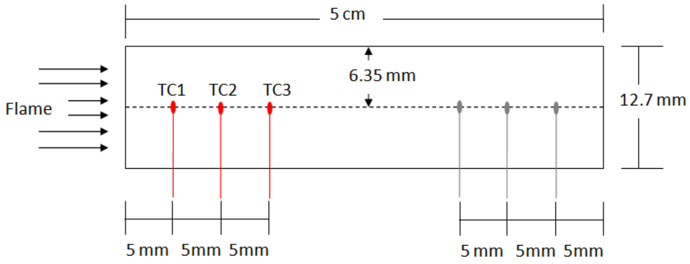

Figure 6.18. Thermocouple location schematic.

6.3.1. Thermal Results

A representative temperature profile of each specimen is shown in Figure 6.19. The specific materials are color coded and the thermocouples are distinguished as: TC 1 solid line, TC 2 dotted line, and TC 3 dashed line. After the 25 second flame exposure is removed the heat is transferred conductively through the specimen. In this set of tests the peak temperature of TC 1 in the CNF sample is 204.8°C and occurs at 60 seconds. The CNF has the highest heat soak temperature. The MWNT and nanoclay TC 1 peaks; 166°C and 174°C, occur at 50 and 64 seconds, respectively. The EPDM/Kevlar TC 1 peak, 168°C, shows the most delay, 75 seconds.

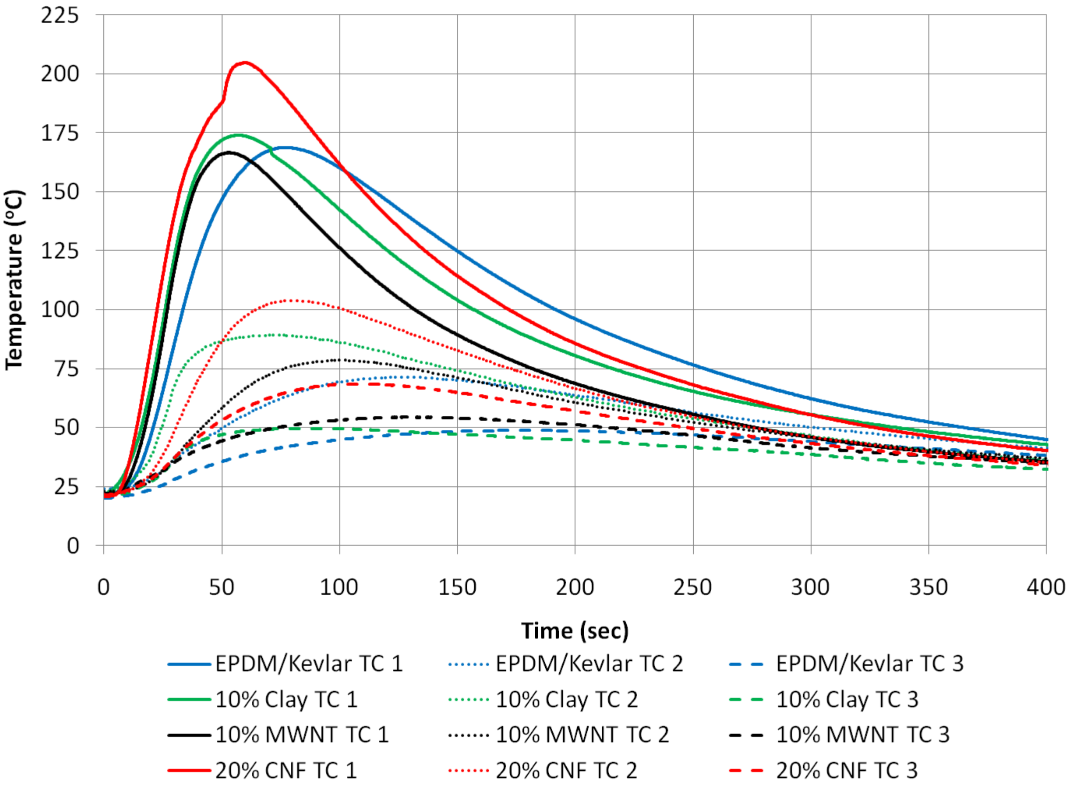

Figure 6.19. Representative oxyacetylene torch temperature profile.

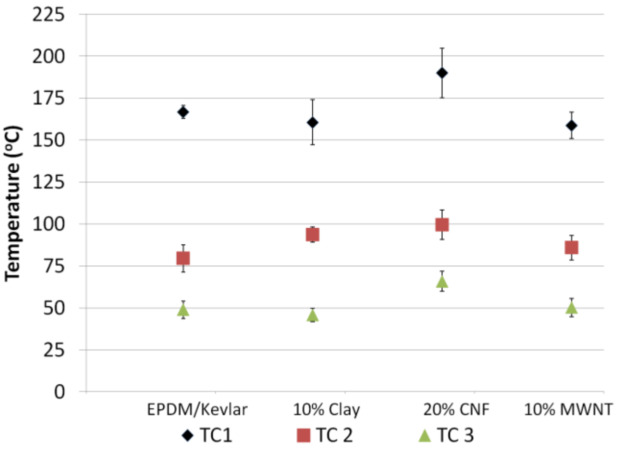

Figure 6.20. Peak in-depth temperatures of EPDM/Kevlar and PNCs.

A numerical heat transfer model is created using virgin TPU material properties (ρ=1.1 g/cm^3, k=0.2 W/mK, c_p=1.5 J/gK). The model allows for heat to be dissipated through convection off each of the side and back walls. After the 25 second burn the front wall also convects heat. A 30 W/m^{2}K convection coefficient is applied to each of these walls. The heat flux is adjusted until TC1 reaches a peak temperature of 200^{o}C to match the temperature profile of the CNF sample. This is achieved at 0.55 MW/m^2. The thermocouple temperatures from the CNF sample and model are shown in Figure 6.21.

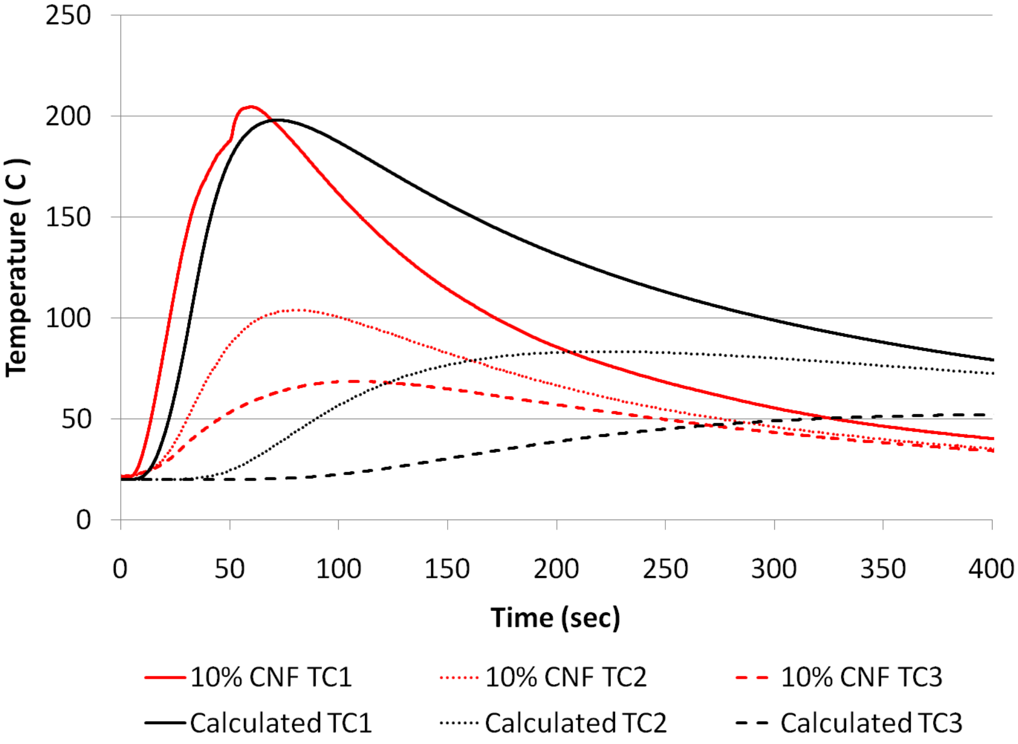

Figure 6.21. Numerical (0.55 MW/m^2) and measured (20% CNF) in-depth thermal history.

As the heating portion of TC1 is increased, there is an 8 second offset between measured and calculated values. The model does not incorporate changes in material properties as the temperature increases most importantly when the surface chars. The CNF specimen has a thick char which considerably increase the penetration depth. The thermal properties of the char are much more conductive than the virgin material which would lead to higher heating and cooling rates. This can account for the higher temperature profile observed. An even more significant offset is observed in TC 2 and TC 3. These reach $50^{o}C$ 60 and 284 seconds after they are measured. Because these thermocouples are in-depth and not in direct contact with the char it is expected these higher responses are due to the higher conductivity of the CNFs and radiation transmission effects not originally expected to be significant.

As the material cools there is also a substantially higher cooling rate measured compared to that calculated. The higher conductivity and char is one cause; another is that the material is held in a drill clamp. The clamp acts as a heat sink and would draw heat from the specimen faster than if simply exposed to convective heat losses.

6.3.2. Post Firing Images

The samples after firing are shown in Figure 6.22 to Figure 6.25. A 1 mm compact char layer is left at the end of the firing of Kevlar/EPDM. Although compact the virgin and char material does not have good adhesion. The nanoclay PNC post test material has about twice the char thickness of the Kevlar/EPDM. Although the char has a crack, the char held well with the virgin material. Similar to the results found in the vertical UL 94 test, in section 4.2, many cracks are observed in the MWNT char surface and result in a weak 2 mm thick char. The CNF PNC char is very thick, greater than 5mm, as the first thermocouple was in the char layer. The CNF char surface is flat without cracks; however it is still very weak. The results from this set of experiments are consistent with the flammability and hybrid rocket tests. The measured average mass loss of each material is shown in Table 6.4. The nanoclay, MWNT, and CNF PNCs lose 13.5%, 33.7%, and 46.5%, respectively, more loss compared to the mass loss of Kevlar/EPDM.

\

Figure 6.22. EPDM post oxyacetylene torch burn.

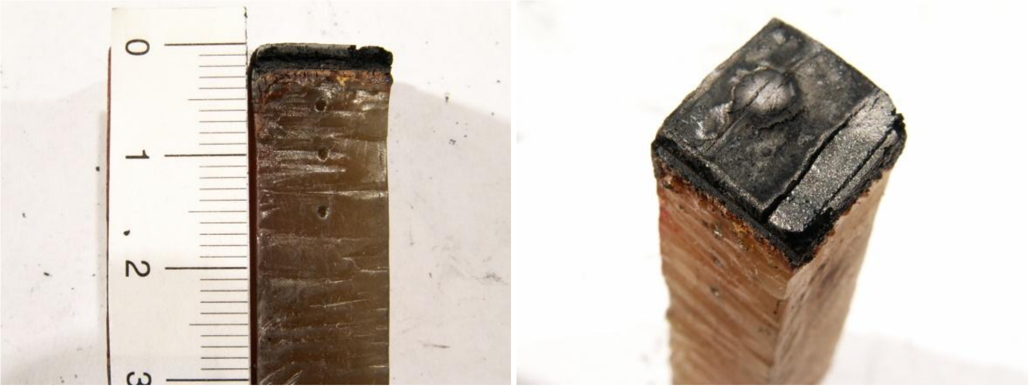

Figure 6.23. 10% Clay PNC post oxyacetylene torch burn.

Figure 6.24. 10% MWNT PNC post oxyacetylene torch burn.

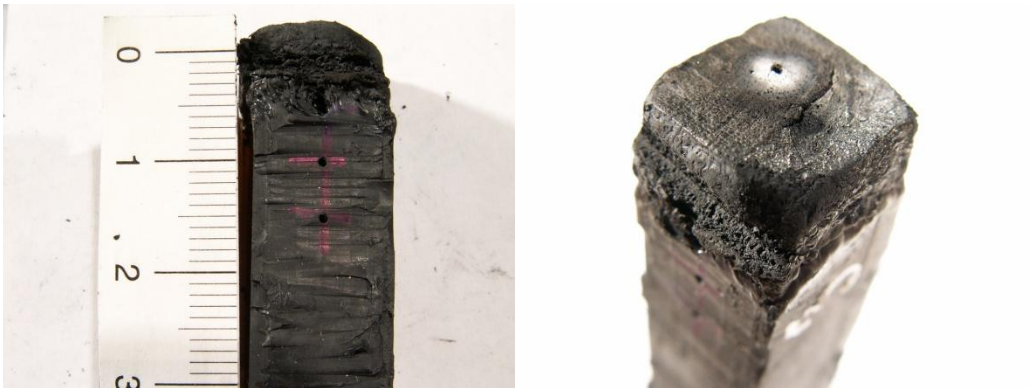

Figure 6.25. 20% CNF PNC post oxyacetylene torch burn.

Table 6.4. Sample mass loss post oxyacetylene torch burn.

	Mass Loss
EPDM/Kevlar	0.288 g
10% Clay	0.327 g
10% MWNT	0.385 g
20% CNF	0.422 g

SEM images of the post fired samples also were taken. The Kevlar/EPDM char material is compact and shows that the individual Kevlar fibers hold the material together as shown in Figure 6.26. The nanoclay char is also a compact composition. A granular morphology is also observed, Figure 6.27. Bubble formations observed in SEM images found in the UL 94 burn tests are observed on the MWNT char surface as well as crack formations, Figure 6.28. An in depth SEM image shows the bundle form of MWNT that is also observed in the UL 94 burn test. The weak CNF char is shown to have a very porous structure, Figure 6.29. Individual CNFs are also able to be observed.

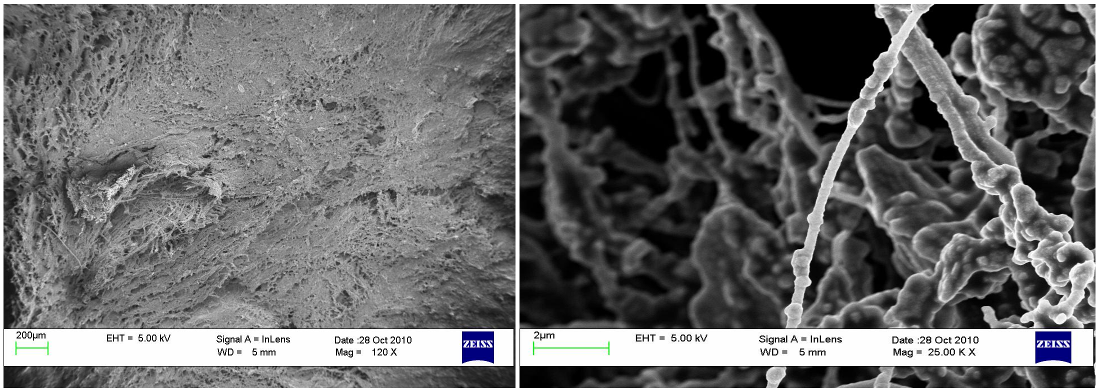

Figure 6.26. SEM of Kevlar/EPDM char post oxyacetylene torch burn (unit bars of left is 200µm and right is 2µm).

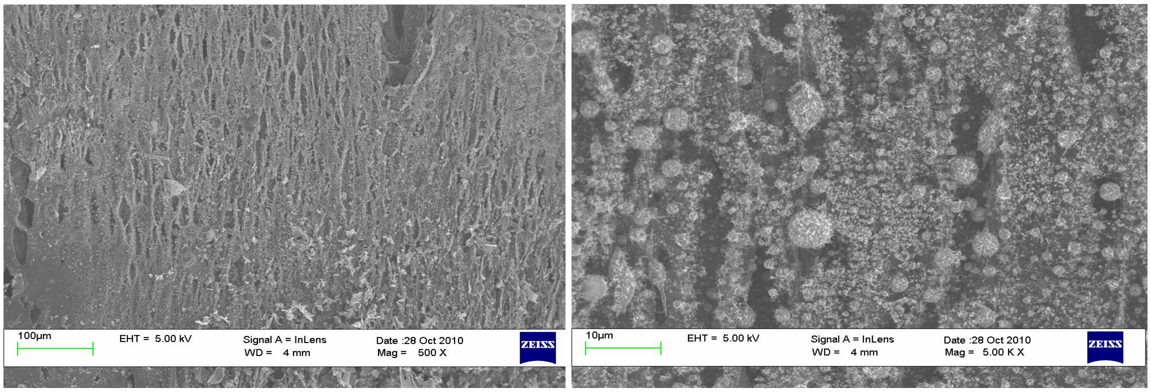

Figure 6.27. SEM of 10% nanoclay PNC char post oxyacetylene torch burn in progressive magnification (unit bars of left is 100μm and right is 10μm).

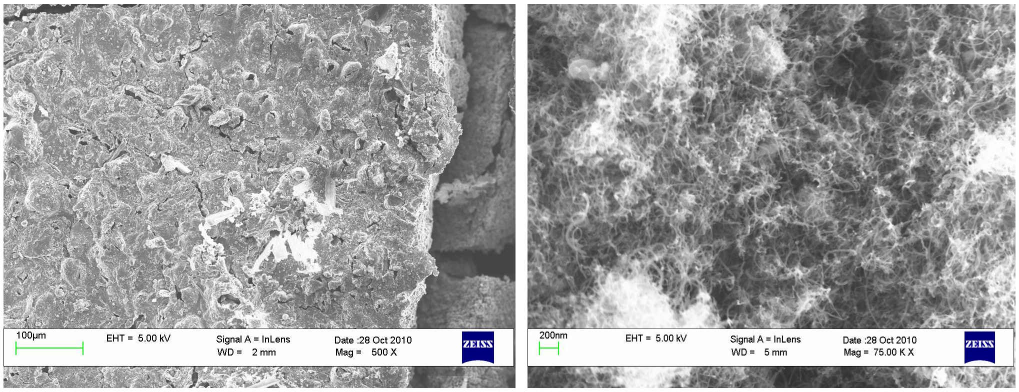

Figure 6.28. SEM of 10% MWNT PNC char post oxyacetylene torch burn in progressive magnification (unit bars of left is 100μm and right is 200nm).

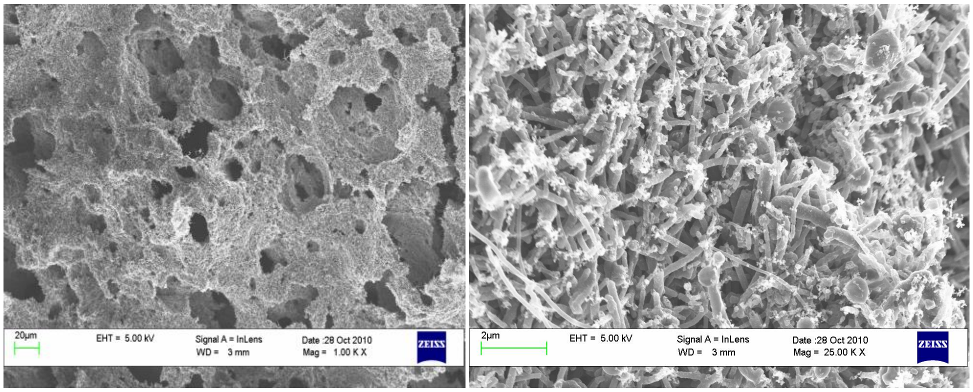

Figure 6.29. SEM of 20% CNF PNC char post oxyacetylene torch burn in progressive magnification (unit bars of left is 20μm and right is 2μm).

6.4. CONCLUSION

The hybrid rocket motor tests have shown the strong char structure of the Kevlar/EPDM. Both the highest weight loadings of MWNT and Nanoclay perform adequate in certain areas of the rocket aft section. The CNF PNCs however do not perform well even at the highest weight loading.

The char created with these tests will be useful in the testing of char strength. The compression test method is a simple and fast test that can be used to quantify char strength in a number of different materials.

The results from the oxyacetylene torch test show that both the nanoclay PNC and MWNT char layers are about twice the thickness of the Kevlar/EPDM char. However, the MWNT char layer is weak compared to the nanoclay PNC char. The CNF char is also very weak and was over five times the thickness of the Kevlar/EPDM char. The mass loss from the CNF sample is almost twice that lost from the Kevlar/EPDM sample. In depth thermal measurements also show that the thermal protection of the PNCs is comparable to that provided by the Kevlar/EPDM, except for the CNF sample which had a much higher peak temperature due to the fact that the first embedded thermocouple ended up in the char region.

The gaseous barrier property of the nanoclay PNCs are again shown to help the PNC enhance its ablative performance. This is observed in the hybrid rocket motor char which show that the pyrolysis zone begins to expand. The high conductivity of the CNFs is shown to negatively impact the heat soak temperatures. This is observed not only in the thermal results from the oxyacetylene torch tests but also by the adhesive debonding of the hybrid rocket motor char. The MWNT char maintains a cracked but continuous surface. The MWNT samples tested in the hybrid rocket motor and oxyacetylene torch are the higher weight loadings. The sample tested in the cone calorimeter which showed a poor char residue was with a 5 wt% loading. Had this formulation been tested in the hybrid rocket motor, results similar to that of the CNF are expected. The higher density of MWNTs provides better MWNT island formations for a continuous but cracked surface to be maintained.

Chapter 7. Conclusion and Future Work

7.1. CONCLUSION

This dissertation studied the work involved in characterizing a new set of ablative materials. Three families of TPUN including nanoclay, MWNT, and CNF nanoadditives are studied. The densities and hardness of the materials increased with nanomaterial loading and the higher weight loadings of the carbon nanomaterials are found to exhibit good electrical conductivity properties. The formulations were found to have good dispersion. At the upper weight loadings of the materials, high viscosities are found to make processing and molding of the materials difficult. Further increasing the loadings used may reach a processing limit.

Degradation studies of the PNC are performed both at low and high heating rates. The calibration of high heating rate experiments is found to be crucial in order to obtain accurate data, and there is not much literature discussing the issues of high heating rate TGA calibration. The PNCs show a distinctly different decomposition profile at the lower heating rates compared to the neat TPU. The two reaction peaks are shifted. Since the two reactions are separated, the peak rate of degradation is also decreased. At these low heating rates the thermal stability is increased by all of the PNCs. Each of the PNC degradation profiles is quite comparable at these heating rates. But as the heating rate is increased to 500^{o}C/min the nanocomposite no longer provides a thermal stability enhancement. In fact the CNF PNC significantly degrades faster than the neat TPU. This as well as the kinetic parameter estimation is a crucial reason why the higher heating rate TGA experiments are necessary to perform. Coupled with a low heating rate TGA experiment FTIR exhaust spectra is taken. The results show that the degradation process in both the neat and PNC happen in two distinct reactions. However the two reactions that occur in the neat TPU overlap much more than in the PNCs. The detection of highest isocyanate concentration occurs in the first reaction for all materials. However in this first reaction is also the highest concentration of CO_2 detected by all the PNC materials, the highest concentration of CO_2 is not detected in the neat TPU until the highest concentration of ether is detected in the second reaction.

Flammability studies show the different char formation in a cone calorimeter heated at 50 kW/m^2. The study shows that each of the PNCs is effective at lowering the PHRR. The CNF formulation tested had the highest PHRR of the three PNCs tested. The char structure of the nanoclay PNC after firing was significantly different than the CNF and MWNT chars. The nanoclay expanded during firing creating a dome-like structure while still maintaining its char integrity. In comparison both the CNF and MWNT PNCs formed weak chars with many cracks present. A second flammability test is performed using vertical UL 94. This experiment showed that the three different nanomaterials degrade and char very differently. The nanoclay formulations created strong chars and at loadings of 7.5% and above are able to maintain its own weight during the degradation process. In comparison the MWNT PNCs show a large amount of crack formation along the char surface. The char created from the MWNTs are very weak and crumble. In comparison the CNF performed the worst in these experiments. The low weight loadings could not create a char structure because the melt flowed too quickly.

Hybrid rocket motor testing was performed to test ablation performance. In addition it provided char structures and a good comparison with the currently used Kevlar/EPDM. The Kevlar/EPDM was found to be much stronger at resisting ablation. The higher weight loadings of nanoclay and MWNT also performed well, however there were regions that had ablated through the sample. Portions of the nanoclay material had a yellowish pigment which indicates that the material had not fully charred. The CNF in these tests had ablated completely through and left no materials to be tested. A current test bed is being refined to test char strength materials. The compression test method is used to measure the resistance required in order to break a char surface. This testing is important and interesting to the TPS field as there are many different TPS tests conducted without a quantifiable measure of char strength.

Oxyacetylene torch experiments are also performed on the PNCs and Kevlar/EPDM. The Kevlar/EPDM created the thinnest char layer and lost the least mass. In depth thermocouples are used to measure the heat wave during the experiment. The MWNT and nanoclay PNCs produced comparable results. The char strength of the nanoclay however is significantly stronger than the MWNT. When the CNF PNC was tested, the torch created a char five times as thick as the Kevlar/EPDM char.

The mechanism which is attributed to the nanomaterials ablative enhancements is that the nanomaterials act as hard segments. This mechanism is observed in the TGA data as the first reaction is slowed down compared to that of the neat TPU. Upon looking at the exhaust compositions it is determined that the depolymerization process is separated in the PNCs in a way that is not separated in the neat TPU degradation. The performance of the nanoclay PNCs is shown to also be attributed to the gaseous barrier, as both in the performance and flammability experiments. This property helps a strong thin char to be formed. A strong char from the carbon-based materials requires a high weight loading because of how the network-island residue is formed. However, even with a high weight loading of MWNT significant cracked surfaces are present. The carbon-based materials also increase the thermal conduction to the backside temperature, observed in the CNF performance tests.

From all of the work presented it is clear that as far as ablative performance is concerned the nanoclay PNC is superior because it creates a char which is thin, strong, and a good gaseous barrier. The MWNT may be considered as well but the CNF is definitely not a good choice for ablative material reinforcement.

7.2. FUTURE WORK AND SUGGESTIONS

Tests had been planned to be performed at Texas State University's Simulated Solid Rocket Motor (SSRM) test facility. The test is attractive in that in addition to a high heat flux, 14 MW/m^2, from a plasma arc jet torch alumina particles can also be ejected. The particles significantly change the ablation testing and provide a more realistic performance test since many propellants do eject molten Al_2O_3 particles. Samples of 1.27 cm x 10.16 cm x 10.16 cm (0.5" x 4" x 4") size are ready for testing as soon as the facility is up and running.

Additional collaboration with the hybrid rocket motor group at Fredericksburg High School has already been planned. Additional materials can be tested. The addition of thermal measurements would be useful at understanding the true conditions occurring within chamber that the ablative materials are in. These materials will also be tested for char strength. As the char strength test instrument is finalized more steps will be necessary to fully automate and standardize test procedures. This would be a good addition to the test setup for a standard to be accepted across the board.

During the proposal of this project work was planned to be performed with the Laser Hardened Materials Evaluation Laboratory. The initial plan was to have specimens tested at high heat fluxes with specially equipped thermocouples. These thermocouples were to be manufactured NANMAC gauges. Specimens were sent to NANMAC and the plan was for them to manufacture their gauges from these materials. Upon cutting into the materials the porosity in these materials was too high for their gauges to work effectively. Eventually the work was thrown out. The gauges that were to be designed for this experiment were expensive however do provide a means for measuring the in-depth as well as surface temperature.

The tests performed can be repeated on new sets of experiments with multiple nanomaterial additives. A combination of nanoclay and MWNT would be an interesting study. The combination of the nanoclay platelet gas barrier and the MWNT network may prove to further enhance the materials ablative performance.

Bibliography

Adam, L., Delaere, K., Kaszacs, M., Gérard, J. S., Assaker, R., & Doghri, I. Multi-scale modeling of polymer nanocomposites.

Agherghinel, I. (1996). Thermogravimetry, analysis of the parameters of the DTG maximum. *Thermochimica Acta, 285,* 57-65.

Agić, A., & Bajsić, E. G. (2007). Strategy for kinetic parameter estimation-thermal degradation of polyurethane elastomers. *Journal of applied polymer science, 103,* 764-772.

Ahmad, R. A. (2005). Convective heat transfer in the reusable solid rocket motor of the space transportation system. *Heat Transfer Engineering, 26*(10), 30-45.

Angioletti, M., Di Tommaso, R.M., Nino, E., & Ruocco, G. (2003). Simultaneous visualization of flow field and evaluation of local heat transfer by transitional impinging jets. *International Journal of Heat and Mass Transfer, 46,* 1703-1713.

Angioletti, M., Nino, E., & Ruocco, G. (2005). CFD turbulent modeling of jet impingement and its validation by particle image velocimetry and mass transfer measurements. *International Journal of Thermal Sciences, 44,* 349-356.

ASTM Standard D1238, 2010, "Standard Test Method for Melt Flow Rates of Thermoplastics by Extrusion Plastometer," ASTM International, West Conshohocken, PA, 2010, www.astm.org.

ASTM Standard D412, 2006e2, "Standard Test Method for Vulcanized Rubber and Thermoplastic Elastomers – Tension," ASTM International, West Conshohocken, PA, 2006, www.astm.org.

ASTM Standard E1582, 2004, "Standard Practice for Calibration of Temperature Scale for Thermogravimetry," ASTM International, West Conshohocken, PA, 2004, www.astm.org.

ASTM Standard E162, 2008b, "Standard Test Method for Surface Flammability of Materials Using a Radinat Heat Energy Source," ASTM International, West Conshohocken, PA, 2008, www.astm.org.

Bala, T., Pence, D. V., & Liburdy, J. A. (2004). Heat transfer dynamics associated with the simultaneous growth of solid-liquid melt layers. *International Journal of Heat and Mass Transfer, 47,* 2619-2628.

Balazs, A. C., Singh, C., Zhulina, E., & Lyatskaya, Y. (1999). Modeling the phase behavior of polymer/clay nanocomposites. *Acc. Chem. Res., 32,* 651-657.

Balek, V., Karabascheva, N. A., & Györyová, K. (1993). Literature survey on thermal analysis reference materials. *Journal of Thermal Analysis, 40,* 1459-1463.

Barick, A. K., & Tripathy, D. K. (2010). Effect of organoclay on the morphology, mechanical, thermal, and rheological properties, of organophilic polyurethane nanocomposites prepared by melt blending. *Polymer Engineering and Science,* 484-498.

Barick, A. K., & Tripathy, D. K. (2010). Thermal and dynamic mechanical characterization of thermoplastic polyurethane/organoclay nanocomposites prepared by melt compounding. *Materials Science and Engineering, A 527,* 812-823.

Benli, S., Yilmazer, Ü., Pekel, F., & Özkar, S. (1998). Effect of fillers on thermal and mechanical properties of polyurethane elastomer. *Journal of Applied Polymer Science, 68,* 1057-1065.

Berta, M., Lindsay, C., Pans, G., & Camino, G. (2006). Effect of chemical structure on combustion and thermal behaviour of polyurethane elastomer layered silicate nanocomposites. *Polymer Degradation and Stability, 91,* 1179-1191.

Beyer, G. (2007). Flame retardancy of thermoplastic polyurethane and polyvinyl chloride by organoclays. *Journal of Fire Sciences, 25,* 65.

Bianchi, D., Martelli, E., & Onofri, M. (2006). Practical navier-stokes computation of flowfields with ablation products injection. *Thermal Protection Systems and Hot Structures Proceedings of the 5th European Workshop, ESA SP-631.*

Bourbigot, S., Samyn, F., Turf, T., & Duquesne, S. (2010). Nanomorphology and reaction to fire of polyurethane and polyamide nanocomposites containing flame retardants. *Polymer Degradation and Stability, 95,* 320-326.

Briber, R. M., & Thomas, E. L. (1983). Investigation of two crystal forms in MDI/BDO-based polyurethanes. *J. Macromol. Sci. – Phys., B 22*(4), 509-528.

Brune, D. A., & Bicerano, J. (2002). Micromechanics of nanocomposites: comparison of tensile and compressive elastic moduli, and prediction of effects of incomplete exfoliation and imperfect alignment on modulus. *Polymer, 43,* 369-387.

Bruns, M. C., Koo, J. H., & Ezekoye, O. A. (2009). Population-based models of thermoplastic degradation: using optimization to determine model parameters. *Polymer Degradation and Stability, 94*(6), 1013-1022.

Buttsworth, D. R., Stevens, R., & Stone, C. R. (2005). Eroding ribbon thermocouples: impulse response and transient heat flux analysis. *Meas. Sci. Technol., 16,* 1487-1494.

Cassel, R. B. (2005). Q5000 IR features to ensure and maintain optimum TGA performance. *TA Instrument Report, TA327,* 1-8.

Ceamanos, J., Mastral, J. F., Millera, A., & Aldea, M. E. (2002). Kinetics of pyrolysis of high density polyethylene. Comparison of isothermal and dynamic experiments. *Journal of Analytical and Applied Pyrolysis, 65,* 93-110.

Cervantes-Uc, J. M., Cauich-Rodríguez, J. V., Vázquez-Torres, H., Garfias-Mesías, L. F., & Paul, D. R. (2007). Thermal degradation of commercially available organoclays studied by TGA-FTIR. *Thermochimica Acta, 457,* 92-102.

Cervantes-Uc, J. M., Moo Espinosa, J. I., Cauich-Rodríguez, J. V., Ávila-Ortega, A., Vázquez-Torres, H., Marcos-Fernández, A., & San Román, J. (2009). TGA/FTIR studies of segmented aliphatic polyurethanes and their nanocomposites prepared with commercial montmorillonites. *Polymer Degradation and Stability, 94,* 1666-1677.

Chamis, C. C., & Coroneos, R. M. (2007). Probabilistic simulation for nanocomposite characterization. *48th SDM Conference, AIAA-2007-1969,* 1-15.

Chen, D., Green, A., & Dollimore, D. (1996). DSC: the importance of baseline calibration. *Thermochimica Acta, 284,* 429-433.

Chen, T. K., Tien, Y. I., & Wei, K. H. (2000). Synthesis and characterization of novel segmented polyurethane/clay nanocomposites. *Polymer, 41,* 1345-1353.

Chiou, B., & Schoen, P. E. (2002). Effects of crosslinking on thermal and mechanical properties of polyurethanes. *Journal of Applied Polymer Science, 83,* 212-223.

Chiou, B., & Schoen, P. E. (2002). Effects of crosslinking on thermal and mechanical properties of polyurethanes. *Journal of Applied Polymer Science, 83,* 212-223.

Cloisite® 30B technical datasheet, Southern Clay Products, Gonzales, TX.

Cothran, L. E., & Barnes, S. V. (1964). Behavior of plastic and refractory materials in the particle-impingement areas of solid propellant ducting systems. *1st AIAA Annual Meeting, AIAA-64-224,* 1-11.

Crighton, J. S., & Wilburn, F. W. (1992). The role of heat transfer in the production of DSC curves. *Thermochimica Acta, 203,* 1-5.

Darby, S. P., Landrum, D. B., & Coleman, H. W. (1998). Assessment of uncertainty in the determination of activation energy for polymeric materials. *Journal of Thermophysics and Heat Transfer, 12*(4), 520-527.

Dasari, A., Yu, Z., Mai, Y., Cai, G., & Song, H. (2009). Roles of graphite oxide, clay, and POSS during the combustion of polyamide 6. *Polymer, 50,* 1577-1587.

Day, M., & Budgell, D. R. (1992). Kinetics of thermal degradation of poly(phenylene sulfide). *Thermochimca Acta, 203,* 465-474.

De Castro, C. A. N., Lourenço, M. J. V., & Sampaio, M.O. (2000). Calibration of a DSC: its importance for the traceability and uncertainty of thermal measurements. *Thermochimica Acta, 347,* 85-91.

Desmopan® DP 6065A technical datasheet, Bayer MaterialScience, Pittsburgh, PA.

Devendra, R., & Hatzikiriakos, S. G. (2006). Rheology of metallocene polyethylene-based nanocomposites: Influence of graft modification. *J. Rheol., 50*(4), 415-434.

Dimitrienko, Y. I., & Dimitrienko, I. D. (2000). Effect of thermomechanical erosion on heterogeneous combustion of composite materials in high-speed flows. *Combustion and Flame, 112,* 211-226.

Dirita, C., De Bonis, M. V., &Ruocco, G. (2007). Analysis of food cooling by jet impingement, including inherent conduction. *Journal of Food Engineering, 81,* 12-20.

Dowdy, D. R. (1987). Meaningful activation energies for complex systems. *Journal of Thermal Analysis, 32,* 137-147.

Doyle, C. D. (1961). Kinetic analysis of thermogravimetric data. *Journal of Applied Polymer Science, V*(15), 285-292.

Endres, W., Dieter Lechner, M., & Steinberger, R. (2003). The kinetics of the thermal decomposition of thermoplastic polyurethane elastomers under thermoplastic processing conditions. *Marcomol. Mater. Eng., 288,* 525-530.

Erickson, K. L. Application of low-heating rate TGA results to hazard analyses involving high-heating rates.

Erickson, K. L. Thermal decomposition mechanisms common to polyurethane, epoxy, poly(diallyl phthalate), polycarbonate, and poly(phenylene sulfide). 1-20.

Erickson, K. L., & Oelfke, J. (2009). Effect of ambient oxygen concentration on thermal decomposition of polyurethanes based on MDI and PMDI. *Fire and Polymers V, Materials and Cncepts for Fire Retardancy, Chapter 23,* 387-407.

Ferriol, M., Gentilhomme, A., Cochez, M., Oget, N., & Mieloszynski, J. L. (2003). Thermal degradation of poly(methyl methacrylate) (PMMA) modeling of DTG and TG curves. *Polymer Degradation and Stability, 79,* 271-281.

Fitzgerald, J. A., & Garimella, S. V. (1998). A study of the flow field of a confined and submerged impinging jet. *International Journal of Heat and Mass Transfer, 41*(8-9), 1025-1034.

Fleischer, A. S., & Nejad, S. R. (2004). Jet impingement cooling of a discretely heated portion of a protruding pedestal with a single round air jet. *Experimental Thermal and Fluid Science, 28,* 893-901.

Flynn, J. H., & Wall, L. A. (1966). A quick, direct method for the determination of activation energy from thermogravimetric data. *Polymer Letters, 4,* 323-328.

Fornes, T. D., & Paul, D. R. (2003). Modeling properties of nylon 6/clay nanocomposites using composite theories. *Polymer, 44,* 4993-5013.

Frick, A., & Rochman, A. (2004). Characterization of TPU-elastomers by thermal analysis (DSC). *Polymer Testing, 23,* 413-417.

Gallagher, P. K., Blaine, R., E., Charlsey, E. L., Koga, N., Ozao, R., Sato, H., Sauerbrunn, S., Schultze, D., & Yoshida, H. (2003). Magnetic temperature standards for TG. *Journal of Thermal Analysis and Calorimetry, 72,* 1109-1116.

Gao, F. (2004). Clay/polymer composites: the story. *Materials Today,* 50-55.

Gao, Z., Kaneko, T., Hou, D., & Nakada, M. (2004). Kinetics of thermal degradation of poly(methyl methacrylate) studied with the assistance of the fractional conversion at the maximum reaction rate. *Polymer Degradation and Stability, 84,* 399-403.

Garashchenko, A. N., Kuznetsov, G. V., & Tksachev, A. I. (1995). The mechanism of high-temperature failure of rubbery heat-refelecting materials in the field of mass inertia forces. *High Temperature, 33*(3), 455-459.

Geisler, R. L. (2002). A global view of the use of aluminum fuel in solid rocket motors. *38th AIAA/ASME/SAE/ASEE Joint Propulsion Conference, AIAA-2002-3748,* 1-8.

Gorrasi, G., Tortora, M., Vittoria, V., Pollet, E., Lepoittevin, B., Alexandre, M., & Dubois, P. (2003). Vapor barrier properties of polycaprolactone Montmorillonite nanocomposites: effect of clay dispersion. *Polymer, 44,* 2271-2279.

Guo, Yalin, Liang, G., Qiu, Z., & Liu, A. (2007). Study of a liquid insulation for the solid rocket motor. *Materials Letters, 61,* 2406-2411.

Gupta, T., & Adhikari, B. (2003). Thermal degradation and stability of HTPB-based polyurethane and polyurethaneureas. *Thermochimica Acta, 402,* 169-181.

Haponiuk, J. T., Balas, A., & Kawka, T. (1990). Application of the DSC analysis of thermoplastic polyurethane elastomers to a comparative study of their technological properties. *Journal of Thermal Analysis, 36,* 2249-2252.

Hentschel, T., Münstedt, H. (2001). Kinetics of the molar mass decrease in a polyurethane melt: a rheological study. *Polymer, 42,* 3195-3203.

Herrera, M., Matuschek, G., & Kettrup, A. (2002). Thermal degradation of thermoplastic polyurethane elastomers (TPU) based on MDI. *Polymer Degradation and Stability, 78,* 323-331.

Ho, W. K., Koo, J. H., & Ezekoye, O. A. (2010). Thermoplastic polyurethane elastomer nanocomposites: morphology, thermophysical, and flammability properties. *Journal of Nanomaterials, 2010,* 1-11.

Ho, W. K., Koo, J. H., & Ezekoye, O. A. (2010). Thermoplastic polyurethane elastomer nanocomposites: morphology, thermophysical, and flammability properties. *Journal of Nanomaterials,* 11 pgs.

Hofmann, H., Martin, H., & Kind, M. (2004). Numerical simulation of heat transfer from an impinging jet to a flat plate. *Chemical Engineering and Technology, 21*(1), 27-30.

Horowitz, H. H., & Metzger, G. (1963). A new analysis of thermogravimetric traces. *Analytical Chemistry, 35*(10), 1464-1468.

Hribar, V. F. (1966). A critique on internal insulation materials for solid propellant rocket motors. *Journal of Spacecraft, 3*(9), 1434-1436.

Hurwicz, H., Kratsch, K. M., & Rogan, J. E. (1972). Ablation. *AGARDograph, AGARD-AG-161,* 1-51.

Hussain, F., Hojjati, M., Okamoto, M., & Gorga, R. E. (2006). Review article: Polymer-matrix nanocomposites, processing, manufacturing, and application: An overview. *Journal of Composite Materiasl, 40*(17), 1511-1575.

Jana, R. N., & Cho, Jae, J. W. (2008). Thermal stability and molecular interaction of polyurethane nanocomposites prepared by in situ polymerization with functionalized multiwalled carbon nanotubes. *Journal of Applied Polymer Science, 108,* 2857-2864.

Jaramillo, M., Edd, A. E., Wells, D. M., & Koo, J. H. (2011). An experimental investigation of char strength of polymer nanocomposites for propulsion applications. *AIAA-SDM 2011 Conference,* (In Press).

Jia, R., Sundén, B., & Faghri, M. (2007). A new low Reynolds stress transport model for heat transfer and fluid in engineering applications. *Transactions of the ASME, 129,* 434-440.

Jia, X., Li, G., Yu, Y., Sui, G., Liu, H., Li, Y., Li, P., & Yang, X. (2009). Ablation and thermal properties of ethylene-propylene-diene elastomer composites reinforced with polysulfonamide short fibers. *Journal of Applied Polymer Science, 113,* 283-289.

Jordan, J., Jacob, K. I., Tannenbaum, R., Sharaf, M. A., & Jasiuk, I. (2005). Experimental trends in polymer nanocomposites-a review. *Materials Science and Engineering, A 393,* 1-11.

Kalogiannakis, G., Van Hemelrijck, D., & Van Assche, G. (2004). Measurements of thermal properties of carbon/epoxy and glass/epoxy using modulated temperature differential scanning calorimetry. *Journal of Composite Materials, 38*(2), 163-175.

Kandola, B. K., Smart, G., Horrocks, A. R., Joseph, P., Zhang, S., Hull, T. R., Ebdon, J., Hunt, B., & Cook, A. (2008). Effect of different compatibilisers on nanoclay dispersion, thermal stability, and burning behavior of polypropylene-nanoclay blends. *Journal of Applied Polymer Science, 108,* 816-824.

Kanevce, L. P., Kanevce, G. H., & Angelevski, Z. Z. (1999). Comparison of two kinds of experiments for estimation of thermal properties of ablative composites. *3rd International Conference on Inverse Problems in Engineering,* 1-7.

Kashiwagi, T., Du, F., Douglas, J. F., Winey, K. I., Harris Jr., R. H., & Shields, J. R. (2005) Nanoparticle networks reduce the flammability of polymer nanocomposites. *Nature Materials, 4,* 928-933.

Kashiwagi, T., Grulke, E., Hilding, J., Groth, K., Harris, R., Butler, K., Shields, J., Kharchenko, S., & Douglas, J. (2004). Thermal and flammability properties of polypropylene/carbon nanotubes nanocomposites. *Polymer, 45,* 4227-4239.

Kim, E. S., Kim, E. J., Shim, J. H., & Yoon, J. (2008). Thermal stability and ablation properties of silicone rubber composites. *Journal of Applied Polymer Science, 110,* 1263-1270.

King, A. J. C., & Chandratilleke, T. T. (2004). Heat transfer enhancement in impinging jets by surface modification. *2004 Electronics Packaging Technology Conference,* 270-272.

Kiran, Y. B., Devendranath Reddy, C., Gunasekar, D., Barbosa, L. C. A., Marney, D. C. O., & Russell, L. J. (2007). Synthesis and TGA evaluation of novel triphosphate esters. *Journal of Fire Sciences, 25,* 193-214.

Kisdi-Koszó, É., Kiss, L. F., Varga, L. K., & Kamasa, P. (1997). Curie temperature measurement of metastable alloys using high heating rate. *Materials Science and Engineering, A226-228,* 689-692.

Koo, J. H., Pilato, L. A., & Wissler, G. E. (2005). Polymer nanostructured materials for propulsion systems, *41st AIAA/ASME/SAE/ASEE Joint Propulsion Conference, AIAA-2005-3606,* 1-16.

Kumar, G., Mahesh, L., Neelakantan, N. R., & Subramanian, N. (1993). Studies on thermal stability and behaviour of polyacetal and thermoplastic polyurethane elastomers blends. *Polymer International, 31,* 283-289.

Lage, L. G., & Kawano, Y. (2001). Thermal degradation of biomedical polyurethanes – a kinetic study using high-resolution thermogravimetry. *Journal of Applied Polymer Science, 79,* 910-919.

Lam, C., Lau, K., Cheung, H., & Ling, H. (2005). Effect of ultrasound sonication in nanoclay clusters of nanoclay/epoxy composites. *Materials Letters, 59,* 1369-1372.

Lau, K., Gu, C., & Hui, D. (2006). A critical review on nanotubes and nanotubes/nanoclay related polymer composite materials. *Composites: Part B, 37,* 425-436.

Laub, B., & Venkatapathy, E. (2004). Thermal protection system technology and facility needs for demanding future planetary missions. *Proc. Int. Workshop, ESA SP-544,* 239-247.

Lee, D., Greif, R., Lee, S. J., & Lee, J. H. (1995). Heat transfer from a flat plate to a fully developed axisymmetric impinging jet. *Transactions of the ASME, 117,* 772-776.

Lee, J. A., Kontopoulou, M., Parent, J. S. (2004). Time and shear dependent rheology of maleated polyethylene and its nanocomposites. *Polymer, 45,* 6595-6600.

Lee, S., & Hanna, M. (2008). Preparation and characterization of tapioca starch-poly(lactic acid)-Cloisite NA$^+$ nanocomposite foams. *Journal of Applied Polymer Science, 110*(4), 2337-2344.

Letuchi, M., Tzur, A., Tchoudakov, R., Narkis, M., & Siegmann, A. (2007). Melt processing and characterization of multicomponent polymeric nanocomposites containing organoclay. *Polymer Composites,* 417-424.

Li, C., & Tang, T. B. (1999). Isoconversion method for kinetic analysis of solid-state reactions from dynamic thermoanalytical data. *Journal of Materials Science, 34,* 3467-3470.

Liu, Z. H., Zhang, X. D., Zhu, X. G., Qi, Z. N., Wang, F. S., Li, R. . Y., & Choy, C. L. (1998). Effect of morphology on the brittle ductile transition of polymer blends: 6. Influence of rubber particle spatial distribution on the toughening and stiffening efficiency of poly(vinyl chloride)/nitrile rubber blends. *Polymer, 39*(21), 5047-5052.

Luchinsky, D. G., & Osipov, V. V. (2008). Model based IVHM system for the solid rocket booster. *2008 IEEE Aerospace Conference,* 1-15.

Ma, C. M., Sung, S., Wang, F., Chiang, L. Y., Wang, L. Y., & Chiang, C. (2001). Thermal, mechanical, and morphological properties of novolac-type phenolic resin blended with fullerenol polyurethane and linear polyurethane. *Journal of Polymer science. Part B: Polymer Physics, 39,* 2436-2443.

Marini, A., Berbenni, V., Capsoni, D., Riccardi, R., & Zerlia, T. (1994). Factors affecting the spectral response in a TG/FT-IR experiment. *Applied Spectroscopy, 48*(12), 1468-1471.

Martin, D. J., Meijs, G. F., Gunatillake, P. A., McCarthy S. J., & Renwick, G. M. (). The effect of average soft segment length on morphology and properties of a series of polyurethane elastomers. II. SAXS-DSC Annealing study. *Journal of Applied Polymer Science, 64*(4). 803-817.

Mathieu, R. D. (1964). Mechanical spallation of charring ablators in hyperthermal environments. *AIAA Journal, 2*(9), 1621-1627.

McAndrew, P. (2008). Arkema Inc. Graphistrength® Carbon Nanotubes. *NIST Polymer Interphases Consortium, Corporate & External Research,* King of Prussia, PA

McAndrew, T.P., Laurent, P., Havel, M., and Roger, C., (2008) Arkema Graphistrength® Multi-Walled Carbon Nanotubes, *report from Arkema Inc., Arkema Research Center,* King of Prussia, PA.

McGhie, A. R. (1983). Thermometric calibration in thermogravimetric analysis. *Anal. Chem., 55,* 987-988.

Meetham, G. W. (1991). High-temperature materials–a general review. *Journal of Materials Science, 26,* 853-860.

Monthioux, M., & Kuznetsov, V. L. (2006). Who should be given the credit for the discovery of carbon nanotubes? *Carbon, 44,* 1621.

Monticelli, O., Musina, Z., Russo, S., & Bals, S. (2007). On the use of TEM in the characterization of nanocomposites. *Materials Letters, 61,* 3446-3450.

Moon, S., Ku, B., Emrick, T., Coughlin, B. E., Farris, R. J. (2009). Flame resistant electrospun polymer nanofibers from deoxybenzoin-based polymers. *Journal of Applied Polymer Science, 111,* 301-307.

Moore, A. L., Cummings, A. T., Jensen, J. M., Shi, L., & Koo, J. H. Thermal conductivity measurements of nylon 11-carbon nanofibers nanocomposites.

Morant, C. A. (1965). Command module heat shield ablator subsystem development plan. *North American Aviation, Inc. Technical Report, SID 64-2067, 1-1 – 5-8.*

Musto, P., Ragosta, G., Scarinzi, G., & Mascia, L. (2004). Polyimide-silica nanocomposites: spectroscopic, morphological and mechanical investigations. *Polymer, 45,* 1697-1706.

Nan, C., Liu, G., Lin, Y., & Li, M. (2004). Interface effect on thermal conductivity of carbon nanotubes composites. *Applied Physics Letters, 85*(16), 3549-3551.

Nanigian, J., & Nanigian, D. (2006). A unique thermocouple to measure the temperatures of squibs, igniters, propellants, and rocket nozzles. *SPIE Paper 6222-3,* 6 pgs.

Nguyen, K., Koo, J. H., Ho, W. K., Bruns, M. C., & Ezekoye, O. A. (2007). Experimental characterization of thermoplastic polyurethane nanocomposite under extreme conditions. *43rd AIAA/ASME/SAE/ASEE Joint Propulsion Conference, AIAA-2007-5770,* 1-18.

Nicolette, V. F., Erickson, K. L., & Vembe, B. E. Numerical simulation of decomposition and combustion organic materials.

Nijuguna, J., Pielichowski, K., & Desai, S. (2008). Nanofiller-reinforced polymer nanocomposites. *Polym. Adv. Technol., 19,* 947-959.

O'Donovan, T. S., & Murray, D. B. (2007). Jet impingement heat transfer – Part I: Mean and root-mean-square heat transfer and velocity distributions. *International Journal of Heat and Mass Transfer, 51*, 3291-3301.

Okamoto, M., Morita, S., Taguchi, H., Kim, Y. H., Kotaka, T., & Tateyama, H. (2000). Synthesis and structure of smectic clay/poly(methyl methacrylate) and clay/polystyrene nanocomposites via in situ intercalative polymerization. *Polymer, 41,* 3387-3890.

Opfermann, J., & Kaisersberger, E. (1992). An advantageous variant of the Ozawa-Flynn-Wall analysis. *Thermochimica Acta, 203,* 167-175.

Ozawa, T. (1965). A new method of analyzing thermogravimetric data. *Bulleting of the Chemical Society of Japan, 38*(11), 1881-1886.

Ozawa, T. (1992). Estimation of an activation energy by isoconversion methods. *Thermochimica Acta, 203,* 159-165.

Patton, R.D., Pittman Jr., C. U., Wang, L., Hill, J. R., & Day, A. (2002). Ablation, mechanical and thermal conductivity properties of vapor grown carbon fiber/phenolic matrix composites. *Composites: Part A, 33,* 242-251.

Paul, D. R., & Robeson, L. M. (In Press). Polymer nanotechnology: Nanocomposites. *Polymer*.

Pizzatto, L., Lizot, A., Fiorio, R., Amorim, C. L., Machado, G., Giovanela, M., Zattera, A. J., & Crespo, J. S. (2009). Synthesis and characterization of thermoplastic polyurethane/nanoclay composites. *Materials Science and Engineering C, 29,* 474-478.

Powell, C. E., Villareal, A. D., & Handcock, J. (2008). Simulated solid rocket motor (SSRM) ablative testing of nanomodified thermoplastic urethane and cyanate ester-rayon fabric composites for integrated high payoff rocket propulsion technology (IHPRPT) solid rocket motor modeling program (SRMM). *Texas State University-San Marcos SSRM Test Report.*

PR-19-XT LHT CNF technical datasheet, Applied Sciences Inc., Cedarville, OH.

Pramoda, K. P., Chung, T. S., Liu, S. L., Oikawa, H., & Yamaguchi, A. (2000). Characterization and thermal degradation of polyimide and polyamide liquid crystalline polymers. *Polymer Degradation and Stability, 64,* 365-374.

Price, D. M., & Church, S. P. (1997). FTIR evolved gas analysis of the decomposition products of cellulose diacetate. *Thermochimica Acta, 294,* 107-112.

Ramezanpour, A., Shirvani, H., & Mirzaee, I. (2003). A numerical study on the heat transfer characteristics of two-dimensional inclined impinging jet. *2003 Electronics Packaging Technology Conference,* 626-632.

Reno, C. D. (1964). Test evaluation of various ablative materials. *MSC Internal Note, MSC-IN-64-EP2,* 1-29.

Reshetnikov, I. S., Garashchenko, A. N., & Strakhov, V. L. (2000). Experimental investigation into mechanical destruction of intumescent chars. *Polymers for Advanced Technologies, 11,* 392-397.

Reshetnikov, I. S., Yablokova, M. Y., Potapova, E. V., Khalturinskij, N. A., Chernyh, V. Y., Mashlyakovskii, L. N. (1998). Mechanical stability of intumescent chars. *Journal of Applied Polymer Science, 67*, 1827-1830.

Reverte, C., Dirion, J., & Cabassud, M. (2007). Kinetic model identification and parameters estimation from TGA experiments. *J. Anal. Appl. Pyrolysis, 79,* 297-305.

Rittigstein, P., Priestley, R. D., Broadbelt, L. J., & Torkelson, J. M. (2007). Model polymer nanocomposites provide an understanding of confinement effects in real nanocomposites. *Nature Materials, 6,* 278-282.

Rosthauser, J. W., Haider, K. W., Steinlein, C., & Eisenbach, C. D. (1997). Mechanical and dynamic mechanical properties of polyurethane and polyurethane/polyurea elastomers based on 4,4'-diisocyanatodicyclohexyl methane. *Journal of Applied Polymer Science, 64*(5)*,* 957-970.

Rudtsch, S. (2002). Uncertainty of heat capacity measurements with differential scanning calorimeters. *Thermochimica Act, 382,* 17-25.

Samborska-Skowron, R., & Balas, A. (2002). An overview of developments in poly(urethane-isocyanurates) elastomers. *Polym. Adv. Technol., 13,* 653-662.

Sánchez-Adsuar, M. S., Papon, E., & Villenave, J. J. (2000). Influence of the prepolymerization on the properties of thermoplastic polyurethane elastomers. Part I. Prepolymer characterization. *Journal of Applied Polymer Science, 76,* 1596-1601.

Sauerbrunn, S., & Gill, P. Decomposition kinetics using TGA. *Thermal Analysis & Rheology, TA-075,* 9 pgs.

Schenider, P. J., Dolton, T. A., & Reed, G. W. (1966). Char-layer structural response in high-performance ballistic reentry. *AIAA 4th Aerospace Sciences Meeting, AIAA-66-424,* 1-21.

Schilling, M. R. (1990). Effects of sample size and packing in the thermogravimetric analysis of calcium Montmorillonite STx-1. *Clays and Clay Minerals, 38*(5), 556-558.

Scully, K., & Bissessur, R. (2009). Decomposition kinetics of nylon-6/graphite and nylon-6/graphite oxide composites. *Thermochimica Acta, 490,* 32-36.

Sichina, W. J. Characterizing polymer lifetimes using TGA decomposition kinetics, *Thermal Analysis Application Note, PETech-66,* 1-5.

Smith-Heberer, E., Wu, L., & Camargo, R. E. (2007). Kinetic and rheological characterization of new, very soft polyurethane elastomers for comfort applications. *Polyurethane 2007 Technical Conference,* 12 pgs.

Song, L., Hu, Y., Tang, Y., Zhang, R., Chen, Z., & Fan, W. (2005). Study on the properties of flame retardant polyurethane/organoclay nanocomposite. *Polymer Degradation and Stability, 87,* 111-116.

Sorathia, U., Beck, C., & Dapp, T., (1993). Residual strength of composites during and after fire exposure. *Journal of Fire Sciences, 11,* 255-270.

Sposato, C., Tamanini, R., Rogers, W. J., & Mannan, M. S. (2003). Effects of plate impingement on the flammable volume of fuel jet releases. *Process Safety Progress, 22*(4), 203-211.

Sung, P. H., & Mark, J. E. (1981). Model polyurethane elastomers prepared from noncrystallizable poly(propylene oxide) chains. *Journal of Polymer Science: Polymer Physics Edition, 19,* 507-515.

Székely, T., Várhegyi, G., & Till, F. (1973). The determination and use of the second derivative thermogravimetric function (DDTG) and the calculation of the kinetic constants of some decomposition reaction types. *Journal of Thermal Analysis, 5,* 227-237.

TA Instruments. (2007). Temperature calibration for TGA and SDT - using curie temperature standards. *TA Instrument Report,* 1-14.

TA Instruments. Modulated thermogravimetric analysis: a new approach for obtaining kinetic parameters. *TA Instruments Thermal Analysis & Rheology, TA-237,* 1-2.

TA Instruments. TGA temperature calibration using curie temperature standards. *Thermal Analysis & Rehology Thermal Application Note, TN-24,* 3 pgs.

Tate, J.S., Kabakov, D., Koo, J. H., & Lao, S. C. (2009). Nanomodified Phenolic/e-glass composites. *2009 SAMPE Conference,* 1-12.

Telara, M., Stella, F., Paglia, F., & Giangi, M. (2005). Pressure oscillations in solid rocket motors. *Fluent News,* S14-S16.

Torre, L., Kenny, J. M., Maffezzoli, A. M. (1998). Degradation behaviour of a composite material for thermal protection systems. Part I – Experimental characterization. *Journal of Material Science, 33,* 3137-3143.

Tran, N. H., Dennis, G. R., Milev, A. S., Kannangara, G. S. K., Williams, P., Wilson, M. A., & Lamb, R. N. (2006). Dispersion of organically modified clays within n-alcohols. *Journal of Colloid and Interface Science, 297,* 541-545.

Trau, J. (1968). Suggestions for reporting thermoanalytical thermogravimetric and derivatographic data. *Chemia Analityczna, 13,* 909.

Usuki, A., Tukigase, A., & Kato, M. (2002). Preparation and properties of EPDM-clay hybrids. *Polymer, 43,* 2185-2189. Vyazovkin, S. V., & Lesnikovich, A. I. (1992).

Practical application of isoconversional methods. *Thermochimica Acta, 203,* 177-185.

Vyazovkin, S., & Wight, C. A. (2000). Estimating realistic confidence intervals for the activation energy determined from thermoanalytical measurements. *Anal. Chem., 72,* 3171-3175.

Wang, Q. (2001). On the prediction of convective heat transfer coefficients using general-purpose CFD codes. *39th AIAA Aerospace Sciences Meeting, A01-16260,* 1-20.

Xiong, J., Zheng, Z., Qin, X., Li, M., Li, H., & Wang, X. (2006). The thermal and mechanical properties of a polyurethane/multi-walled carbon nanotube composite. *Carbon, 44,* 2701-2707.

Yang, F., Yngard, R., & Nelson, G. L. (2005). Flammability of polymer-clay and polymer-silica nanocomposites. *Journal of Fire Sciences, 23,* 209-226.

Zammarano, M., Gilman, J. W., Krämer, R. H., Harris Jr., R., Ohlemiller, T. J., & Shields, J. R. (2008). Effect of nanoparticles on flammability of flexible polyurethane foams. *19th BCC Conference,* 7 pgs.

Zanetti, M., Bracco, P., & Costa, L. (2004). Thermal degradation behaviour of PE/clay nanocomposites. *Polymer Degradation and Stability, 85,* 657-665.

Zeng, Q. H., Yu, A. B., & Lu, G. Q. (2008). Multiscale modeling and simulation of polymer nanocomposites. *Prog. Polym. Sci., 33,* 191-269.

Zhang, F., Li, S., Karaki, T., & Adachi, M. (2005). Synthesis of polyethylene/Montmorillonite nanocomposites by in-situ intercalative polymerization. *Japanese Journal of Applied Physics, 44*(1B), 658-661.

Zhao, W., Li, M., & Peng, H. (2010). Functionalized MWNT-doped thermoplastic polyurethane nanocomposites for aerospace coating applications. *Macromol. Mater. Eng., 295*(9)*,* 838-845.

Ziering, M. B., & DiCristina, V. (1972). Thermomechanical erosion of ablative plastic composites. *AIAA 7th Thermophysics Conference, AIAA-72-299,* 1-14.

Vita

Jason Chi-Sing Lee was born in Pasadena, California on September 2nd 1983, to Norman and Anny Lee. He has two sisters, Rene' and Tammy Lee. After graduating from Schurr High School, in Montebello California, in 2001 he studied Mechanical Engineering at the University of California, Berkeley.

In 2005 he began his graduate studies at the University of Texas at Austin working under Dr. John R. Howell, modeling the heat transfer of a welding process. Under this project he spent a summer at Los Alamos National Laboratory as well as traveled to Brazil in 2007 under the NSF supported Pan-American Advanced Studies Institute (PASI) studying Predictive Process Dynamics for Manufacturing (PPDM). His thesis work was with Gas Technology Institute (GTI) studying the thermal environment of a steel furnace tube using FLUENT. Two semesters were spent as a TA for the undergraduate fluid dynamics laboratory class.

He began his PhD work in 2007 at UT under Dr. Joseph Koo and Dr. Ofodike Ezekoye, studying polymer nanocomposites. He also worked on the Predictive Engineering and Computational Sciences project, sponsored by DOE, one of the centers of the Predictive Science Academic Alliance Program, beginning in 2009, where he helped provide data on NASA ablative materials. This provided him with the opportunity to work at Sandia National Laboratory in 2009 and Dr. Kenneth Erickson.

He has co-chaired a session at the Join Propulsion Conference, has published multiple papers, some of which are still in the process of being written and/or reviewed.

Permanent address: 1756 Laurel Drive Monterey Park, Ca 91755

This dissertation was typed by the author.